University of Napoles Federico II

Department of Industrial Engineering

Doctoral Degree
XXXVI Cycle

Innovative IoT-based Methods for remote control, monitoring and measurements

Coordinator:
Ch.mo Prof. Michele Grassi

Advisor:
Ch.mo Prof. Rosario Schiano Lo Moriello

Co-Advisor:
Dr. Ing. Giorgio de Alteriis

Candidate:
Ing. Caputo Enzo
ID. DR995318

SUMMARY

INTRODUCTION

The restrictions associated with the current SARS-Cov-2 pandemic are having a major impact on nearly all human activities and interactions. In this context, both educational practices and industrial processes have faced substantial challenges. This thesis work is structured in two distinct yet interconnected sections each addressing specific domains within the technological landscape.

Section I: IoT Device To Remotely Control System

This section is focused on revolutionizing didactic approaches in response to the restrictions imposed by the pandemic, particularly in laboratory-based educational settings. In the face of lockdowns and reduced physical access to facilities, the proposed solution leverages the Internet of Things (IoT) and the fourth industrial revolution. By utilizing remotely controlled instruments displayed in augmented reality on consumer devices, students can access, operate, and learn from laboratory instruments with realism and effectiveness.

This theme has been expanded to the the realm of Cyber-Physical Systems (CPS) and digital twins. It introduces an innovative approach that employs Augmented Reality (AR) as a Digital Twin for measurement instruments. This not only bridges the gap between physical and digital worlds but also showcases the practicality of the proposed method through an application involving a digital storage oscilloscope.

Then the framework adopted previously has been used to address safety concerns in laboratory experiences, especially in disciplines such as Sciences, Technology, Engineering, and Mathematics (STEM). By introducing a mixed-reality solution with augmented reality on the student side and actual instrumentation on the laboratory side, this approach ensures a secure and enriching educational experience. The study demonstrates its applicability to experiments involving remote control of measurement instruments and addresses generic risk conditions through an illustrative case study on gamma radiation measurements.

Section II: IoT For Localization And Monitoring

This section shift the focus to innovations within industrial systems, exploring technologies such as Bluetooth Low-Energy (BLE), Micro-Electro-Mechanical Systems (MEMS), and predictive maintenance algorithms.

In the automotive field, the use of smartphones and BLE Fingerprinting for a Passive Entry Passive Start (PEPS) system. By overcoming spatial orientation challenges and implementing data filtering techniques, the study showcases the reliability of the proposed method in determining the driver's position within or outside the vehicle.

Moving to structural health monitoring (SHM), a method combining redundant MEMS accelerometers with a Kalman Filter approach. This approach compensates for inherent errors in MEMS-based sensors and establishes a real-time monitoring sensor node using LoRaWAN and NFC protocols.

The final part explores the application of Long Short-Term Memory (LSTM) deep learning algorithms for predictive maintenance in the railway domain. The study, conducted within an academic-industrial partnership, showcases the methodology's efficacy in forecasting failures of railway rolling stock equipment with remarkable accuracy.

SECTION 1 - IoT DEVICE TO REMOTELY CONTROL SYSTEM

The first Section focuses on distance learning activities, unfortunately became mostly important during the recent COVID-19 pandemic; in particular, the so-called "*Remote laboratories*" are taken into account. More specifically, the aim was to define and prototipally implement, in particular it will be explored a hardware/software framework to remotely control laboratories instrument without losing contact the idea of "hand" interaction with the instruments. To this aim, the crucial aspect of instrument scanning and 3D reconstruction, which plays a fundamental role in facilitating the remote laboratory experience, will be first discussed. Subsequently, it will be delved into the technologies that enable users and laboratories to communicate effectively and securely through remote instrument control.

To fully assess the reliability and efficacy of the proposed framework, a case study and user experiences will be presented analyzed.

Subsequently, it will be explored the concept of a "*Cyber-Physical System*" and demonstrated that a similar framework can play a concrete example of the relevat role in the definition and implementation of an Augmented Reality-based cyber-physical system.

Lastly, the extension of the considered framework to the remote instrument control for conducting experiments safely will be addressed; in particular, a solution involving the measurement of gamma ray energy spectra will be presented and discussed to assess its feasibility. The involved hardware and software architectures will be analyzed and the obtained experimental results will be shown.

Chapter 1 - Remote Laboratories

Remote laboratories, often referred to as remote labs, are specialized facilities where measurement instruments are operated and controlled remotely through an internet connection [1], [2]. These remote laboratories have emerged as invaluable tools, particularly in the context of teaching technical subjects.

Below are listed the strengths of a remote laboratory:

1. **Overcoming the Challenge of Student Numbers:** In traditional university settings, the number of students attending technical courses can often be substantial, making it logistically challenging to provide hands-on laboratory experiences for all learners. Physical labs may be limited in capacity and availability, leading to scheduling conflicts and restricted access. Remote laboratories offer a solution to this problem by allowing students to access lab equipment and perform experiments from remote locations. This not only ensures that every student has an opportunity to engage with the material but also provides flexibility in terms of when and how experiments are conducted.
2. **Mitigating Resource Constraints:** Educational institutions, especially in resource-constrained environments, may face difficulties in acquiring and maintaining a diverse range of expensive laboratory equipment. Even well-funded institutions can struggle to keep up with the rapid advancements in technology. Remote labs address this challenge by centralizing expensive equipment and making it accessible to multiple students. This efficient resource allocation ensures that students can access cutting-edge equipment and technology without the burden of heavy institutional investments [3]–[5].
3. **Enhancing Accessibility and Inclusivity:** Remote laboratories extend accessibility to a wider audience, including students with physical disabilities, geographical constraints, or other limitations that may hinder their ability to attend in-person lab sessions. This inclusivity promotes equal educational opportunities and ensures that no student is left behind due to circumstances beyond their control.
4. **Facilitating Collaborative Learning:** Remote laboratories can facilitate collaborative learning experiences where students from different institutions or

even different countries can work together on experiments and projects. This global collaboration not only enriches the educational experience but also exposes students to diverse perspectives and approaches.

5. **Encouraging Experimentation and Exploration:** With remote laboratories, students have the freedom to experiment and explore without the fear of damaging expensive equipment. This promotes a culture of curiosity and innovation, allowing students to learn from their mistakes and develop problem-solving skills.
6. **Preparing Students for the Digital Age:** Operating remote labs via the Internet closely mirrors the technology-driven work environments that students are likely to encounter in their future careers. By familiarizing students with remote experimentation, these laboratories equip them with skills and competencies that are highly relevant in the digital age.

So, it is possible to say that remote laboratories address critical challenges related to student numbers and resource constraints while promoting inclusivity, collaboration, and hands-on learning; they will play a pivotal role in shaping the future of technical education by ensuring that students have access to high-quality, practical learning experiences regardless of their location or the size of their classes.

1.1 State of Art

Regarding the hardware and software architecture of remote laboratories, there are various proposals in literature [1]–[10]. Some solutions prioritize ease of use or flexibility, to the detriment of a greater burden on implementation, while others optimize concurrent request queuing [11]–[13]. Nevertheless, all these solutions share a common feature: the utilization of user interfaces designed for conducting specific measurements as requested by the lecturer. However, these interfaces cannot exactly replicate the appearance of the actual laboratory instrumentation [14], [15].
This approach poses a potential challenge in that it may disconnect students from the physical reality of the laboratory. In such cases, the students' interaction is limited to receiving measurement results from the instruments, and they may miss out on the

hands-on experience of operating the equipment themselves. As a result, the current concept of remote laboratories is primarily tailored for a teaching approach that complements traditional in-person lessons and exercises conducted in a physical laboratory setting. During these in-person sessions, students have the opportunity to become familiar with the front panel of the instruments and their various configurations for optimal measurements.

However, this approach has limitations, particularly when access to physical laboratories in schools and universities is restricted for compelling reasons, such as public health concerns during a pandemic. In such situations, students are denied the crucial hands-on experience that would enable them to develop the expertise needed to tackle more complex measurement problems. This limitation underscores the need to continually innovate and improve remote laboratory solutions to bridge the gap between virtual and physical laboratory experiences, ensuring that students can receive comprehensive education regardless of the circumstances.

To address this limitation, a novel approach has been introduced that not only overcomes the constraints of traditional laboratory settings but also enhances the learning experience. This solution focuses on the integration of Augmented Reality (AR) technology into the sphere of remote laboratories.

AR has garnered increasing attention in various domains due to its unique ability to augment the physical world with digital information, making it an invaluable tool for several applications. The solution harnesses the power of AR to transform the way students engage with laboratory experiments and educational activities.

In recent years, AR has demonstrated its utility in different contexts. For instance, AR systems have been used to support workers during training sessions, where it overlays essential contextual information onto real-world scenarios (as illustrated in [16]). Similarly, building projects have benefited from AR's ability to simulate spatial and temporal constraints, enabling the superimposition of Building Information Modeling (BIM) elements onto real-time site videos [17]. AR has also found application in maintenance tasks, such as assisting in the servicing of electrical equipment [18] and enhancing users' awareness of their energy consumption [19].

In the Education context, AR has emerged as a potent teaching aid. Numerous educational proposals in the literature have leveraged AR technology to enrich the learning experience by adding contextual information to real-world settings [20]. Examples range from the use of AR in primary schools to aid learning [21]–[24] to more specialized applications like supporting mechanical engineering education with a Web3D and AR-based system [25].

In contrast to existing solutions that depend heavily on simulations [26], [27], the AR-based remote laboratory, implemented in our laboratories, has been developed with a revolutionary approach. It empowers students to conduct laboratory experiments using everyday devices such as smartphones, tablets, or personal computers. With this system, students can interact with faithful reproductions of laboratory instruments as if they were physically present in the laboratory.

What sets our approach apart is the seamless translation of students' actions on the AR instrument's front panel into commands sent to real instruments. These instruments are configured according to the student's input and provide the desired measurement results. This tangible interaction with actual equipment ensures that students gain practical experience and a deep understanding of the experimental process.

Operationally, students are equipped with markers or paper simulacra representing the necessary instruments for their experiments. When viewed through their device's camera, these markers trigger the appearance of lifelike instrument reproductions on their screens. The reconstruction is meticulously crafted to be as realistic as possible, including the faithful emulation of button presses and other seemingly minor details. This level of realism enables students to fully immerse themselves in the laboratory experience, just as they would in a physical setting.

In summary, the proposed AR-based remote laboratory represents a paradigm shift in education and practical training. By seamlessly merging the physical and digital worlds, we provide students with a unique learning experience that combines the convenience of remote access with the authenticity of hands-on experimentation. This innovation has the potential to revolutionize the approach of laboratory for the education and opens up exciting possibilities for future educational technology developments.

1.2 Proposed Framework

The primary goal is to empower students with the capability to engage in laboratory activities prescribed by their college curriculum, even when access to physical laboratories is impeded due to unforeseen circumstances or overcrowded class sizes. This innovative approach not only addresses practical challenges but also ensures that students have an educational experience that closely simulates what they would encounter in a physical laboratory setting.

The following are listed as the main aspects of the AR-based remote laboratory:

- **Enhancing Accessibility**: One key motivation behind our research is to make laboratory education more accessible. There are instances, such as during cases of force majeure, when students cannot physically access laboratories. Additionally, in highly populated classes, providing each student with the required training time can be economically and operationally burdensome, necessitating the replication of measurement stations or laboratory lectures. By introducing remote laboratories in augmented reality (AR), it mitigates these challenges and provides a flexible solution that promotes equal access to quality education;
- **Realistic Instrument Replicas**: An essential aspect of this type of laboratory is to create digital replicas of laboratory instruments that closely resemble their physical counterparts. These digital instruments should not be perceived as abstract or simulated entities but must be connected to the actual laboratory equipment. The objective here is to enhance students' knowledge, skills, and expertise by offering them a lifelike laboratory experience. This immersion is essential for students to gain a deep understanding of instrument appearance and functionality;
- **Framework for AR Remote Laboratories**: A crucial aspect is to establish a comprehensive framework for the development of AR remote laboratories. The framework's purpose is to make it easy to add instruments while utilizing cutting-edge technologies associated with the Internet of Things and the fourth industrial revolution. By leveraging these technologies, we can ensure

integration and interoperability with other contemporary tools and platforms, enhancing the overall educational experience;

- **Applicability Across Disciplines**: It's worth highlighting that the proposed framework is not limited to a specific educational domain but can be applied across various fields where students interact with laboratory equipment. Regarding the introductory courses in basic electrical and electronic measurements, students often encounter laboratory instruments for the first time and need to learn how to operate them through the instrument's front panel to perform measurements in both time and amplitude domains [28].

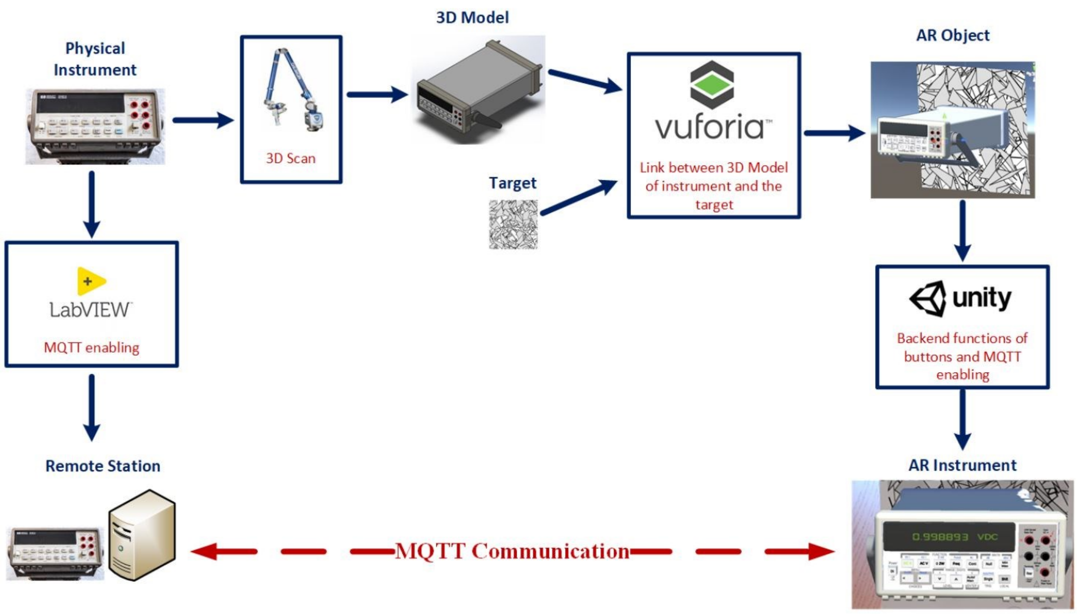

Figure 1. Graphical scheme of the developed framework.

As illustrated in Figure 1, the framework consists of several key steps. The initial step involves scanning and 3-D reconstructing the instrument image. This process typically employs reverse engineering techniques, combining data acquisition methods such as 3-D scanners with 3-D image analysis methodologies. These techniques allow us to transform point cloud data into a precise geometric reconstruction of the instrument. The subsequent step involves associating the obtained 3-D instrument model with a specific marker, pattern, image, or object to enable rendering. However, this representation remains empty without further functionalization. To address this, it has been integrated software module responsible for replicating the functionality of various buttons and controls found on the instrument's front panel. This operation is executed within a 3-D development platform that manages image rendering and user interaction through scripts responding to user inputs.

Moreover, the actions performed on the front panel are converted into messages compliant with the Message Queue Telemetry Transport (MQTT) protocol [29]. These messages are exchanged with a remote station situated in the physical laboratory. To complete the process, students are provided with an application to install on their devices. This application enables them to recreate the laboratory instruments by framing the relevant marker with their device's camera.

MQTT is a lightweight communication protocol utilizing a publish-subscribe model and TCP/IP for transport [30]. It is particularly suited for scenarios with limited bandwidth and low impact. In contrast to traditional client-server systems, MQTT employs a broker that dispatches messages published under specific topics to all devices subscribed to those topics, facilitating efficient and reliable communication among connected devices.

1.2.1 Instrument Scan and 3-D Reconstruction

The initial phase of the proposed framework involves the creation of 3-D models for the desired laboratory instruments using techniques typical of reverse engineering. Reverse engineering encompasses the utilization of specialized instruments to capture 3-D geometric data and dedicated software to manipulate and interpret this data into usable information. This versatile approach can serve various purposes, ranging from inspecting fabricated parts and functional devices to generating 3-D models for objects that do not currently exist [31]–[34].

The reverse engineering process is broadly divided into two fundamental steps: (i) measurements and (ii) subsequent processing. Measurements are conducted using suitable systems, with considerations given to data accuracy, density, part features, and surface properties, all tailored to the specific task at hand [34]. There are three primary methods for data collection: touch probe, surface scanning, and volume scanning, each chosen based on factors such as feature-based data or dense point cloud data, depending on the application requirements [34].

In this context, it has been employed the reverse engineering approach to create virtual models of laboratory instruments. For clarity, let's illustrate these steps using a digital multimeter (DMM) as an example. It has been integrated image acquisition techniques and systems with image analysis methods. Since internal features were not a primary concern, it has been chosen a non-contact FARO Laser ScanArm among various measurement systems to capture images, thereby obtaining information about the instrument's shape and size (Fig. 2).

Figure 2. Measurement phase: image acquisition using noncontact FARO Laser

The collected datasets have been processed using dedicated software and procedures.

To define mathematical representations for reconstructing the instrument's geometry, it has been implemented computer-aided design (CAD) systems and methodologies. The measurement phase involved data collection, while the processing phase centered on interpreting these measurements into meaningful information. The scanning process generated point clouds, which are sets of data points in three-dimensional space, used to create 3-D CAD models. Depending on the complexity of the part and the surface characteristics, point clouds can range from a series of points collected by a probe swept across a part to an extensive scan of a part's surface, comprised of millions of measured points. Such dense point clouds are employed when the complexity of the part requires more data for surface characterization [34].
Handling dense point clouds effectively is essential; the management has begun with the utilization of Geomagic Wrap software (as depicted in Fig. 3).

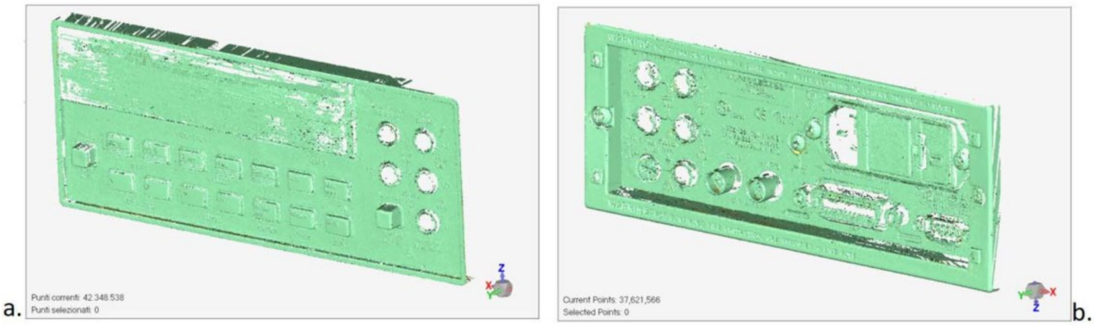

Figure 3. Point clouds: (a) multimeter front and (b) rear panels.

This software facilitates the transformation of point cloud data, probe data, and imported 3-D formats (e.g., OBJ, STL) into 3-D polygon meshes for use in analysis and design applications. This step involved preliminary cleaning, point selection, point number reduction, and noise reduction operations.
Subsequently, the 3-D image reconstruction process commenced, involving blending operations and the creation of surfaces from tessellated models. These operations were conducted using the SolidWorks 2018 CAD system, where the ScanTo3D add-in played a crucial role in generating 3-D CAD models from scanned data. The final CAD model was constructed by assembling four primary parts (case, front panel, rear panel, and support system/height adjustment) (as shown in Fig. 4). All buttons were designed individually and placed in specific positions to create the assembled model, and they

functioned independently. The choice of colors for different parts of the model aimed to replicate the appearance of the real instrument.

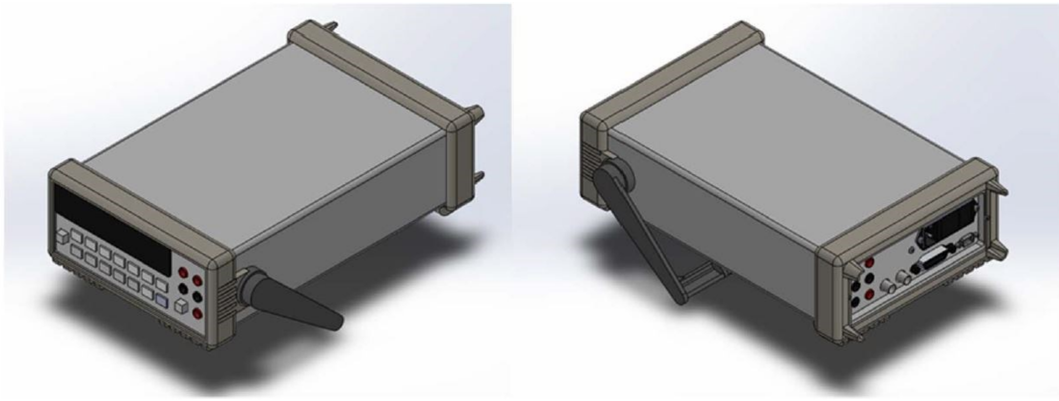

Figure 4. 3-D reconstruction and multimeter CAD models: different views

1.2.2 User-Side Enabling Technologies

The output of the scanning operations produces a file with the OBJ extension, containing a 3-D digital replica of the physical object. The subsequent step involves transforming this raw 3-D virtual object into an interactive 3-D Augmented Reality graphic interface. This interface allows students, to operate on the corresponding physical instrument located in a remote laboratory. To ensure user-friendliness and accessibility, it has been developed an application, referred to as APP-AR, which can run on mobile phones or tablets – devices that are readily available to students. To implement this app, it has been used the 3-D graphic development platform Unity [35], [36] and the integrated Vuforia software development kit [37]–[39] into the 3-D engine to enable the use of AR content.

Developing the AR APP and ensuring its functionality involved several essential steps. The first step was selecting an appropriate target image. In AR applications, the target image is crucial for placing the 3-D virtual object in the scene. The APP-AR activates the device's camera and displays what it records on the screen. A software module continuously processes the image to locate the target. When the target enters the camera's field of view, the APP-AR superimposes the 3-D digital replicas of the instruments (Fig 5.a) on the marker in the scene captured by the device's camera, creating the AR effect (Fig 5.b).

a. b.

Figure 5. Rendering of the instrumentation due to (a) AR approach and (b) user display screenshot after target identification.

Target images in AR applications are typically high-contrast squares or rectangles composed of black and white geometric shapes, making them easily recognizable. Creating the target image involves two phases: image generation and training the AR software to identify it. The complexity of the target pattern influences the stability of rendering the corresponding instrument. Different patterns can be used to distinguish between different instruments or laboratory experiences. Vuforia simplifies the development of essential components in an AR app, including recognition, tracking, and rendering of AR content [40], [41]. The marker recognition training phase is managed by Vuforia's target manager module [42]. If the chosen image is suitable as a target image (Fig 6.a), the module identifies several characteristic points on the image, marking them with yellow crosses (Fig 6.b).

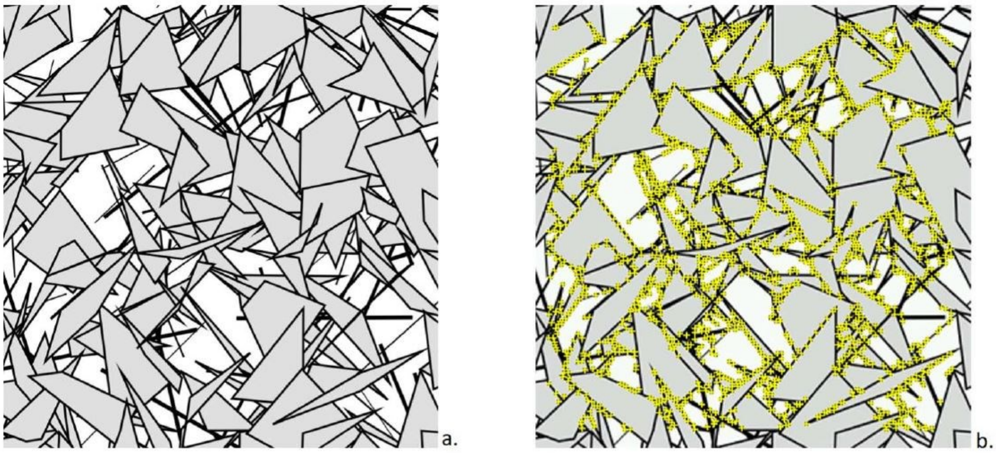

Figure 6. Training result in target. (a) Recognition with Vuforia. (b) Yellow crosses are image characteristic points that make it possible both target recognition and orientation in the space.

Once the software has been trained to identify the target image, the image target can be loaded and positioned in the scene within a Unity 3-D project (Fig 7.a). The target is then associated with the graphic elements to be rendered in AR, represented by 3-D virtual instruments in the application (Fig 7.b), and the relative position with respect to the target (Fig. 7.c). Additionally, a software module has been developed to recognize button presses on the AR instrument [43]. This module, written in C# language and based on event programming (Fig 7.d), interprets the sequence of actions performed by the user, corresponding to instrument configurations, parameter settings, or measurement requests.

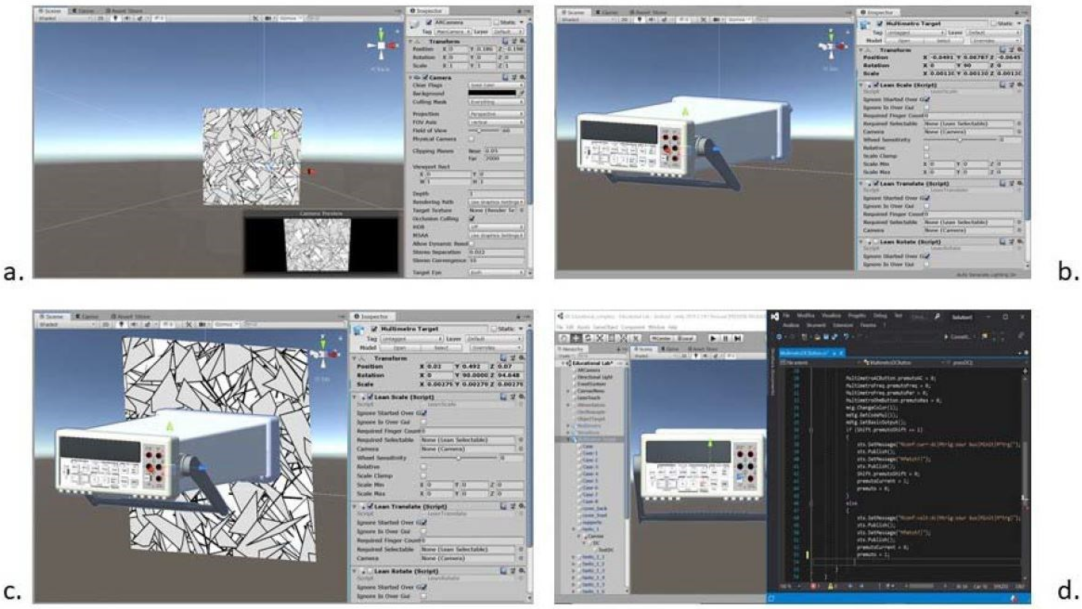

Figure 7. a) Target and (b) instrument imported in the Unity 3-D environment and associated for (c) rendering after recognition. (d) Buttons of the reconstructed

Valid key combinations trigger software events that update a finite state machine (FSM). When a valid command is recognized, it generates a command string compliant with the IEEE488 protocol [44], [45] and sends it to the instruments in the laboratory for execution via an MQTT client integrated into the APP-AR. If a response from the instrument is expected, such as a measurement result, the MQTT client receives the response, and the APP-AR updates the displays of the AR instruments with the received information. In essence, the implemented app allows users to interact with AR interactive 3-D models, providing the sensation of directly manipulating physical instruments in the laboratory, even from different locations, such as in distance learning scenarios.

To enhance the user experience and make the 3-D AR instrument more realistic, additional graphic functions and effects have been implemented in UNITY. These include emulating button movements when pressed and adding backlighting effects. Finally, all these software modules are integrated and compiled into the Unity 3-D project to produce installation packages (APK and IPA) for the distribution of the developed APP-AR on Android and iOS devices, respectively.

1.2.3 Laboratory-Side Enabling Technologies

To enable communication between students' devices and laboratory instrumentation, it is essential to modernize the physical laboratory using IoT technologies. Specifically, a measurement station has been established within the laboratory to receive user requests. This station receives messages from users via Ethernet and connects to the instrumentation using the IEEE488 protocol. The framework described here is versatile and can be easily adapted to any communication interface used by the laboratory equipment.

Furthermore, this framework demonstrates that it is possible to upgrade and "IoTtify" laboratory instruments with outdated ICT technologies without the need to purchase modern devices. This approach reduces costs and minimizes electronic waste.

The measurement station can connect to various instruments, either independently for exercises aimed at familiarizing students with specific instrument functions or electrically interconnected for more complex experiments requiring multiple instruments to analyze the same signal. To reduce waiting times for laboratory access, multiple stations can be replicated.

From a software perspective, the station application was developed using the National Instruments LabVIEW environment, which facilitates communication with other devices via the IEEE488 protocol through its libraries. The station software translates user requests into messages sent to the instrumentation and vice versa. As described in the previous section the user communication is accomplished through MQTT messages. Therefore, the station program must convert MQTT messages into IEEE488 command strings for the instrumentation and vice versa, translating responses from the instrumentation into MQTT messages to relay back to the user.

In terms of message encoding, the traditional Standard Commands for Programmable Instruments (SCPI) was chosen in this case study, but the framework is not limited to this option, as the command language is entirely transparent from the MQTT messaging perspective. The choice of SCPI is associated with the instruments already available in the lab, and other languages or libraries may be considered if the instruments' control server has the necessary drivers. Similarly, for the framework's implementation on the laboratory side, any programming language or environment capable of interacting with IEEE 488.2 or similar interface drivers could have been used. In this case, LabVIEW was selected for compatibility with existing measurement stations in the laboratories.

Concerning MQTT communication, the public broker HiveMQ (available at https://www.mqtt-dashboard.com/) was utilized. For each laboratory instrument, a corresponding topic was created, with the topic name following the template *ARRemLab/Station-number/Device-number*. The station number specifies a particular measurement station, while the device number identifies the instrument to be connected to. Both the user application and the station software must subscribe to the same topic to receive messages from the broker. The user application publishes commands to be sent to the instrument identified by the device number on this topic. A lookup table stored in the station software associates the general-purpose interface bus (GPIB) address of the corresponding instrument with each topic, allowing the software to forward user message command strings to the addressed instrument using the *LabVIEW GPIB Write* function.

The same topic is also used to transmit replies received from the instrument identified by the device number. In this case, the LabVIEW software acts as the publisher and posts the response received from the instrument to which a query has been sent. Any user subscribed to the topic (not just the one sending the command and queries) will receive the instrument's replies (i.e., the measurement results). Subsequently, the user software integrates the received information into the AR object shown to the student.

Access control and management of concurrent accesses are handled through MQTT messaging. To ensure students' understanding of the laboratory experience, each student is granted exclusive control of a station for a maximum of 30 minutes. MQTT's inherent features facilitate this exclusivity, ensuring that the authorized user is the only one capable of sending commands to the station's instruments. Other students can subscribe to the topic of any instrument to receive measurement results, but they cannot publish on that topic, i.e., they cannot send commands.

MQTT messaging offers the advantage of facilitating information exchange between a measurement instrument and any number of users. For example, synchronous online experiments can be conducted where the lecturer controls the instrument's operations, and all students in the class view the measurement results on their AR instruments. Alternatively, if a user is solely interested in collecting measurement results, they can subscribe to the topic and receive them, eliminating the need for laboratory reservations and corresponding waiting times.

Regarding authentication and authorization, the lecturer has preassigned students to laboratory shifts and scheduled their remote laboratory access. Each remote measurement station has a reservation file associating a unique identification number (e.g., university ID number) with a defined time slot for a student's use. Access concurrency is also managed through MQTT topics. Specifically, a topic, *ARRemLab/Station-number/Connection-Status*, with the retain property set to true, provides information about the station's occupation status to prevent unauthorized access when a student is already using the instruments. If the station is available, and the user ID matches the current time slot, the student gains access to the lab resources. A timer displaying the remaining access time is then shown in AR on the user's display. Authentication is performed using the topic *ARRemLab/Station-number/User*, where the user is the publisher, and the station subscribes to receive the user ID and verify the user's eligibility for the current time slot. The user ID also aids the server in logging information related to user operations. All actions performed by the authorized user are recorded in a text file associated with their user ID, allowing the lecturer to assess the student's level of preparation.

In Figure 8, an architecture diagram of the laboratory is presented. In the example, three users have subscribed to the topic related to the first instrument of station 1. However, only one user has exclusive access to station 1 during the designated time slot and is authorized to send commands to device 1. All users, including those without exclusive access, receive messages posted on the topic. This framework's scalability is very useful, as adding a new instrument to the measurement station simply involves connecting the instrument to one of the laboratory stations and updating the station's lookup table with the corresponding topic.

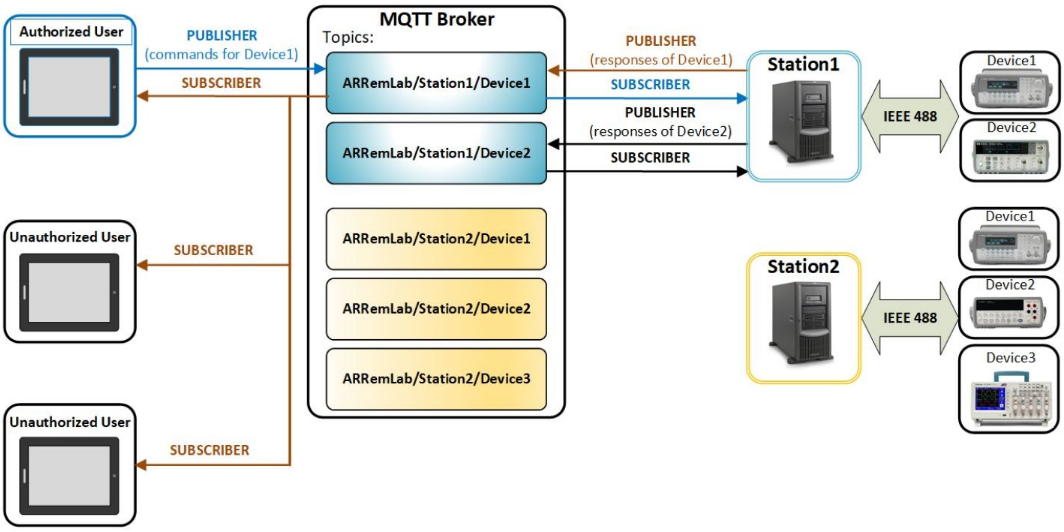

Figure 8. Block diagram of the remote laboratory access and exploitation.

1.3 Case Study and User Experience

To illustrate the practical application of this framework and provide insight into the user experience, it will be described a real-life laboratory activity commonly undertaken by students in basic metrology courses. This activity involves the measurement of the root mean square (rms) voltage of an alternating current (AC) signal. The detailed description is provided to emphasize the high level of technical realism achieved in representing these activities through Augmented Reality instruments.

Upon launching the AR application (APP-AR), the user is prompted to enter their academic registration number. By clicking the "AR START" button, the user gains access to the measurement station, which is equipped with an Arbitrary Waveform Generator (AWG) model 33220A and a Digital Multimeter (DMM) model 34401A, both manufactured by Agilent Technologies. As previously mentioned, the user is granted exclusive publishing access to the station for a 30-minute period. However, an additional "AR STOP" button is available, allowing the student to release the station before the reservation period expires (refer to Figure 9).

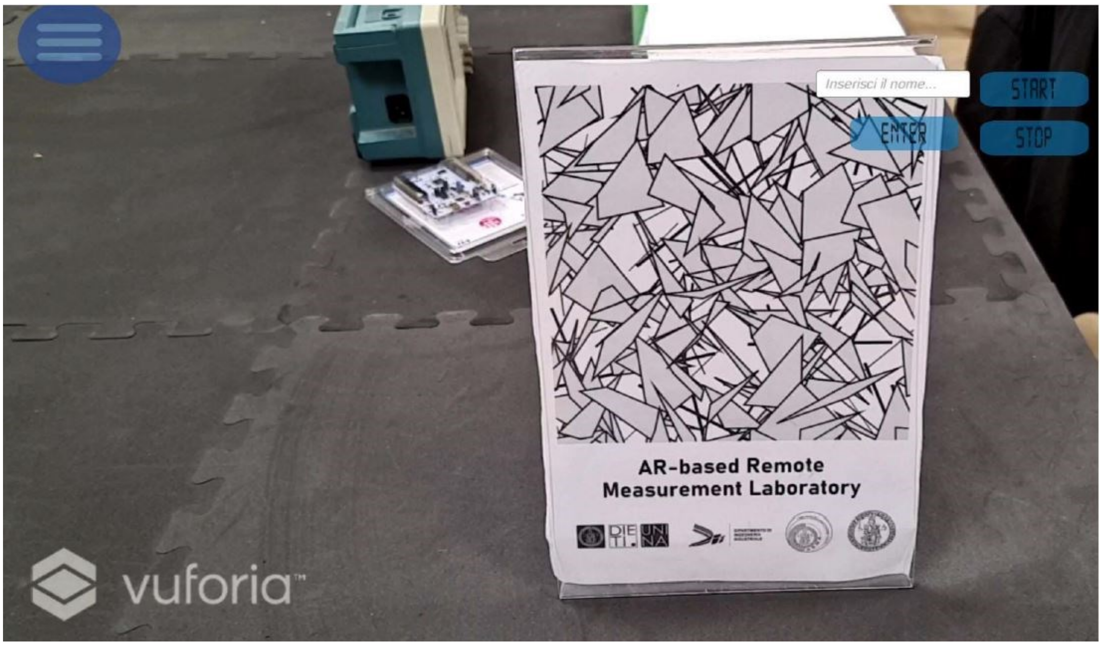

Figure 9. APP-AR menu.

The laboratory activities can be divided into two sequential steps:

1. *Setting the Generator Parameters*: in this initial step, the user configures the AWG to produce the desired sine waveform. This involves specifying parameters such as frequency, amplitude, and waveform shape to generate an AC signal that matches the requirements of the experiment;
2. *Taking Measurements with the Multimeter*: in the second step, the user interacts with the front panel of the digital multimeter. They perform the necessary operations to obtain accurate measurements of the AC signal's root mean square (rms) voltage. This may include selecting the appropriate measurement function, configuring measurement settings, and interpreting the displayed results.

In this way, the student has a realistic and hands-on laboratory experience facilitated by AR instruments and he can engage in metrology experiments, learn measurement techniques, and gain a deeper understanding of AC signal analysis.

1.3.1 Waveform Generator Setup

As is well known, multimeters typically have high input impedance when configured for AC voltage measurements. On the contrary, the adopted waveform generator defaults to being connected with a 50-Ω load. To prevent any discrepancies between the required and measured voltages, it is imperative to provide the generator with accurate information about the electrical load, a configuration known as "*HIGHZ*."
To achieve this configuration in the Augmented Reality environment, the following sequence of actions is performed by the user on the AR front panel of the generator within the APP-AR:

1. The user selects the "*Utility*" softkey to access the configuration menu;
2. The user then chooses the "*Output Setup*" softkey to access the menu for configuring the generator's output stage;
3. Next, the user selects the "*Load/HighZ*" softkey to update the output configuration;
4. Finally, the user confirms their selections by pressing the "*DONE*" softkey.

When these operations are executed on the AR front panel of the generator, they trigger software events to update the states of a dedicated Finite State Machine (FSM) (see Figure 10). These events also generate an IEEE488 string "*OUTP:LOAD INF*" to be sent to the generator, instructing it to set the desired "*High Z*" configuration.

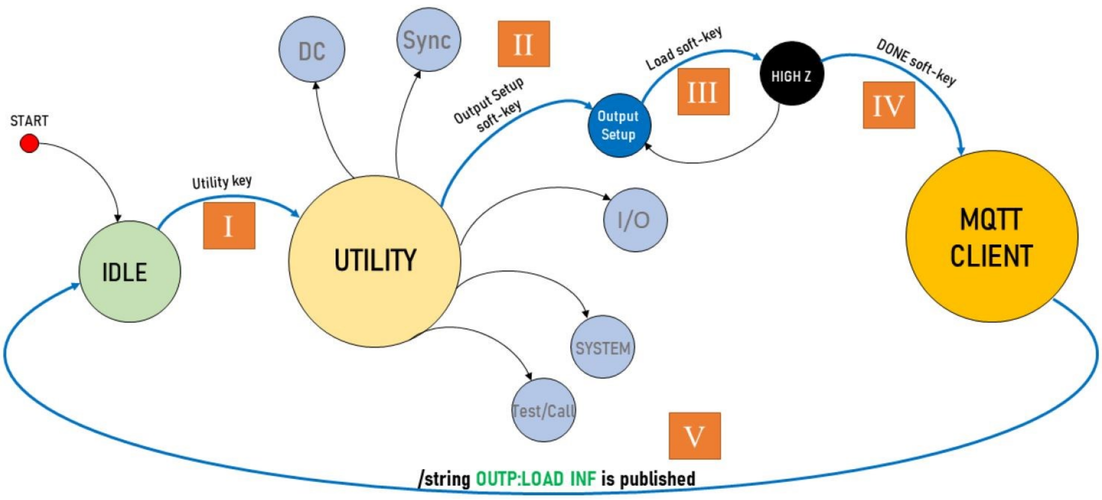

Figure 10. Example of FSM exploited for waveform generator setting; for the sake of the conciseness, other functions implemented but not exploited in the example are shaded.

This string, denoted as the payload, is encapsulated within an MQTT message published by the APP-AR on the topic *ARRemLab/Station1/Device12*. The MQTT client running on the server station receives this message from the broker as soon as it is published. Subsequently, the command string contained within the message is transmitted to the instrument using the IEEE488 protocol through the GPIB/USB interface. Upon receiving the command, the signal generator adjusts its output to the "*High Z*" configuration.

To ensure that no messages are lost between the user and the measurement station, a Quality-of-Service (QoS) level of 2 is selected, despite the potential for communication delays [46]. Upon receiving confirmation of the message, the MQTT client of APP-AR automatically sends a query (corresponding to the string *OUTPut:LOAD?*) to the instrument to verify that the configuration change was successfully executed. If the response from the instrument differs from the expected value, it indicates a problem or error occurred during the configuration operation. In the case of a successful operation, the instrument responds with the string "*9.9E+37*," as specified in the instrument's program manual [47].

While sending a query after each configuration may seem redundant, it is essential for maintaining continuous correspondence between the internal state of the FSM within APP-AR and the actual setting of the instrument. This redundancy ensures the reliability of the entire system efficiently and effectively.

The essential functions of the AWG include generating five standard waveforms (sine, square, ramp, pulse, and noise) and direct current (DC) voltage, as well as configuring their key parameters (amplitude, frequency, and offset). By default, the function generator is set to generate a sine waveform upon power-up. In such cases, students can directly proceed to configuring the waveform parameters. However, if a different waveform is required, the student must first press the "*SINE*" key on the front panel of the augmented instrument to select the sine waveform generation mode.

Upon pressing the "*SINE*" key, the string "*FUNC SIN*" is transmitted to the instrument to set the sine waveform. Once the confirmation of the MQTT message delivery is received, an automatic query ("*FUNC?*") is sent to verify that the configuration change was successful. If the instrument responds with the string "*SIN*" (indicating that the setting was correctly executed), no error messages are displayed on the student's display, and the virtual "*SINE*" key remains illuminated, matching its corresponding button on the actual instrument.

To set the frequency of the signal, the student presses the "*FREQ*" softkey, inputs the desired numeric value using the numeric keypad (e.g., 2), and selects the desired unit of measurement (e.g., kHz) by pressing the corresponding softkey. Particularly, the AWG display updates in real-time to reflect the selected unit of measurement. The user's input generates the command string "*FREQ 5 kHz*," which is sent to the server to configure the desired signal frequency. If the configuration is successfully accepted, the instrument responds to the "*FREQ?*" query with the selected frequency value.

Similarly, the student can configure the values of amplitude and offset voltage (e.g., 70 mVrms and 0V, respectively). Once the generator configuration is complete, pressing the "*OUTPUT*" button activates the voltage waveform at the generator's output terminals. This operation results in the sequential transmission of the command string "*OUTP ON*" and the query "*OUT?*" will return either "1" (indicating the output is enabled) or "0" (indicating the output is disabled). Based on the received value, the "*OUTPUT*" button on the student's mobile display will either be illuminated or not.

For the sake of completeness, the interaction diagram of an MQTT transmission between the authorized user and the measurement station is given in Fig. 11; in particular, in addition to the considered output load configuration, also the messages associated with waveform selection and frequency setting are reported.

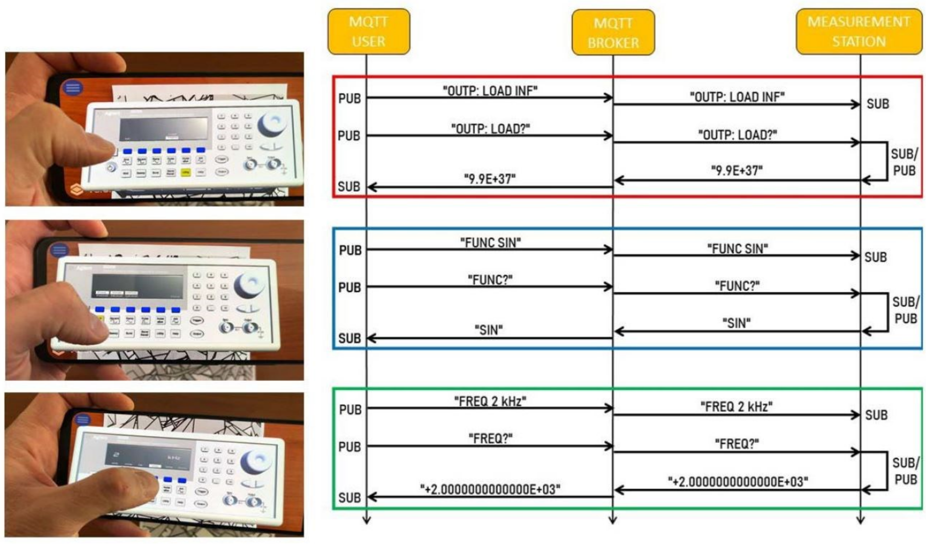

Figure 11. Interaction diagram among MQTT clients (at user and station sides) and broker. For the sake of the clarity, messages associated with QoS management are not reported.

1.3.2 DMM Setup and AC Voltage Measurement

In the context of the Digital Multimeter (DMM), they will be described two key operations that shed light on specific features of the Augmented Reality interaction and the underlying communication with the remote laboratory. The DMM's front panel includes two rows of keys for function and setting selection. Like most instruments, certain keys offer secondary functions, printed in blue above them on the front panel. To access these secondary functions, the user must press the "*SHIFT*" key followed by the key corresponding to the desired secondary function.

To enhance the user experience, the AR multimeter faithfully replicates the behavior of the real instrument, including the use of secondary functions. Two crucial parameters influencing measurement results are the range and resolution. Upon powering on the instrument, it automatically selects the appropriate range. However, users can manually choose their desired range by toggling between automatic and manual mode using the "*Auto/Man*" key and adjusting the range with the up and down arrow keys on the AR instrument's front panel (see Figure 12).

For instance, when measuring AC voltage, selectable range values typically span from 100 mV to 750 V. The chosen range value is consistently maintained as one of the state variables within the APP-AR, updated with each arrow keystroke, and communicated to the instrument. Selecting the AC range of 100 mV would result in the string sent to the instrument being "*VOLT:AC:RANG 0.1*" (indicated by the green path in Figure 12). Similar to the AWG, the APP-AR verifies the multimeter's correct configuration after receiving confirmation from MQTT by sending an appropriate query.

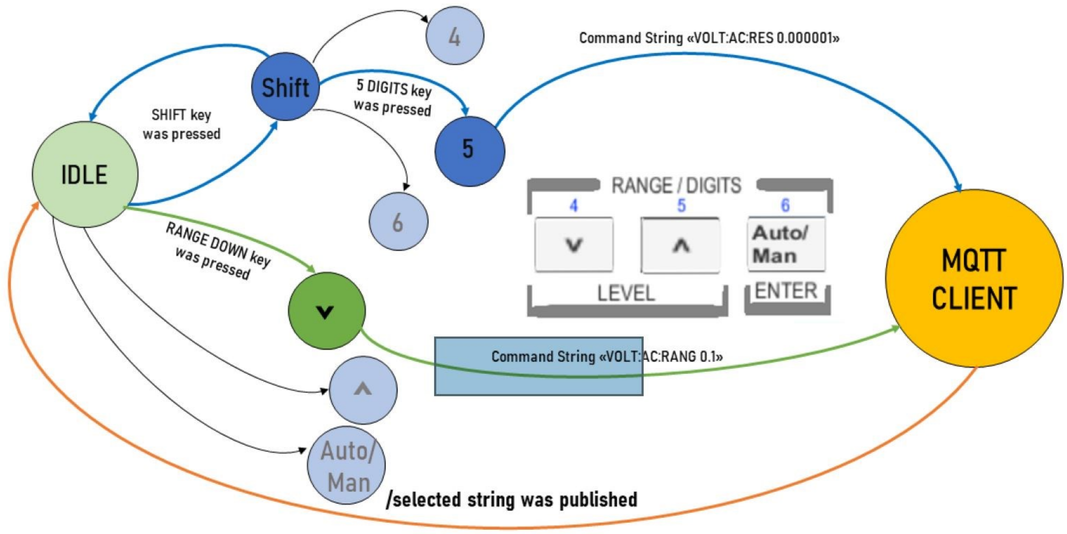

Figure 12. Example of FSM exploited for DMM setting in the presence of secondary functions. Green path refers to normal configuration (ac voltage range selection), while blue path points out the secondary function (ac voltage resolution). The corresponding portion of the APP-AR display is also represented

Resolution in DMMs is often expressed in terms of the number of digits used to display measurement results. The instrument used here offers three resolution settings ranging from 4½ to 6½ digits, with a default setting of 5½ digits at power-up. Higher resolution yields more precise results but at the cost of slower measurements, while lower resolution allows for faster measurements with potentially lower accuracy. Resolution selection shares keys with the range and is accessible as a secondary function. To select the desired resolution, the user must first press the "*SHIFT*" button (indicated by the green path in Figure 12).

In the example, the user sets a 5½ digits resolution, which, coupled with the 100 mV range, corresponds to a resolution of 1 μV. Consequently, the MQTT client integrated into the APP-AR transmits the configuration string "*VOLT:AC:RES 0.000001*" to the measurement station.

To execute the root mean square (rms) voltage measurement in this application, the user presses the "*ACV*" key on the AR front panel. For the remote station to carry out this measurement, the following sequence of commands must be sent to the instrument: "*CONF:VOLT:AC*" followed by "*INIT*" and the query "*FETCH?*". These commands and the query are concatenated into a single string separated by the pipe (|) character, such as "*CONF:VOLT:AC|INIT|FETCH?*". The server handles the separation of these strings and sends them in the correct order to the instrument to manage the measurement operation effectively.

Once the measurement is completed, the instrument returns a string containing the measurement result. This result is then sent from the server to the APP through MQTT and displayed on the virtual instrument's screen according to the selected range and resolution.

Figure 13. and 13.b illustrate the AR laboratory and the corresponding remote laboratory, respectively. It's important to note that the settings and measurements displayed by the AR instruments accurately mirror those of the real instruments located in the remote laboratory. This fidelity ensures that students have a realistic and educational experience when using the AR instruments for metrology experiments.

Figure 13. Comparison between (a) AR experience and (b) actual remote laboratory.

Chapter 2 - Cyber-Physical System

The concept of Cyber-Physical Systems (CPS) was initially introduced in 2006 by Helen Gill of the National Science Foundation in the United States [48]. Gill's concept aimed to describe a new dimension where the physical world and virtual control and observation capabilities are intricately connected. CPS represents an evolution beyond traditional embedded systems, where computational capabilities permeate every physical component and even the materials themselves [49].

Since its inception, the concept of CPS has evolved significantly, making it challenging to provide a definitive and unambiguous definition. The commonly accepted definition of CPS involves the integration of computational resources and physical processes, but this description has become overly simplistic as CPS has expanded to include elements like large-scale network connectivity.

In its current most common definition, CPS represents the integration of diverse systems with the primary goal of controlling a physical process and dynamically adapting to changing conditions in real-time. This integration combines physical objects and processes, computational platforms, and telecommunications networks [50], [51].

The term "physical" in CPS refers to tangible objects perceivable by human senses, while "cyber" relates to the virtual representations of these objects, often enriched with additional layers of information. In literature there are several examples that have aptly referred to the relationship between physical objects and their virtual counterparts as the "social network of objects" [52].

2.1 State of Art

CPS systems are built on interconnected objects equipped with sensors, actuators, and network connections. These components generate and collect various types of data, reducing distances and information disparities within the system [53]. Sensors enable CPS to autonomously assess its current operational state and the relationships among its constituent objects. Actuators execute planned actions and implement corrective measures, optimizing processes and solving problems [54].

Intelligence plays a pivotal role in CPS, as it evaluates internal information within the system and, in certain scenarios, considers information from other CPSs [55]–[57]. Interactions with measurement systems, including sensors, sensor networks, and actual measurement instruments, are crucial within CPS. The objective is to seamlessly integrate measurement systems into CPS, effectively creating digital twins of these systems. This integration enables users to interact with and understand measurement systems as an integral and prioritized part of the CPS, enhancing the overall user experience [58].

It is possible to use the framework and the solution proposed in the previous paragraph to realize a CPS system that provides the creation of a digital twin of the measuring instrument, which can be controlled and operated remotely. To achieve this goal, various enabling technologies drawn from the paradigms of Industry 4.0 and the Internet of Things (IoT) are leveraged. As seen before two key technologies in this context are augmented reality and MQTT communication protocols.

Augmented reality technology is harnessed to construct a digital replica of the measuring instrument, providing users with a visual and interactive representation. This digital twin aims to faithfully emulate the physical instrument, offering a rich and immersive experience for remote operators.

Additionally, the utilization of MQTT communication protocols enhances the connectivity and data exchange between the remote operator and the instrument.

This approach seeks to bridge the physical gap between operators and instruments, opening up new possibilities for education and industry alike.

2.2 Application Example of the Implemented Ar-Based Cyber-Physical System

This section explores into a case study that showcases a practical application, specifically in the context of basic metrology courses where students typically work with a digital oscilloscope. To evaluate the effectiveness and reliability of this solution, a dedicated mobile application has been developed.

Students engage with a rendered 3D digital oscilloscope through the mobile application, simulating the actions they would perform on an actual instrument. The first step is to power on the oscilloscope, mirroring the real-world procedure. Upon pressing the power button in the Augmented Reality application, a query is sent to the physical oscilloscope to retrieve the waveforms currently displayed and its configuration parameters, such as horizontal (s/div) and vertical (V/div) resolution (as illustrated in Figure 14).

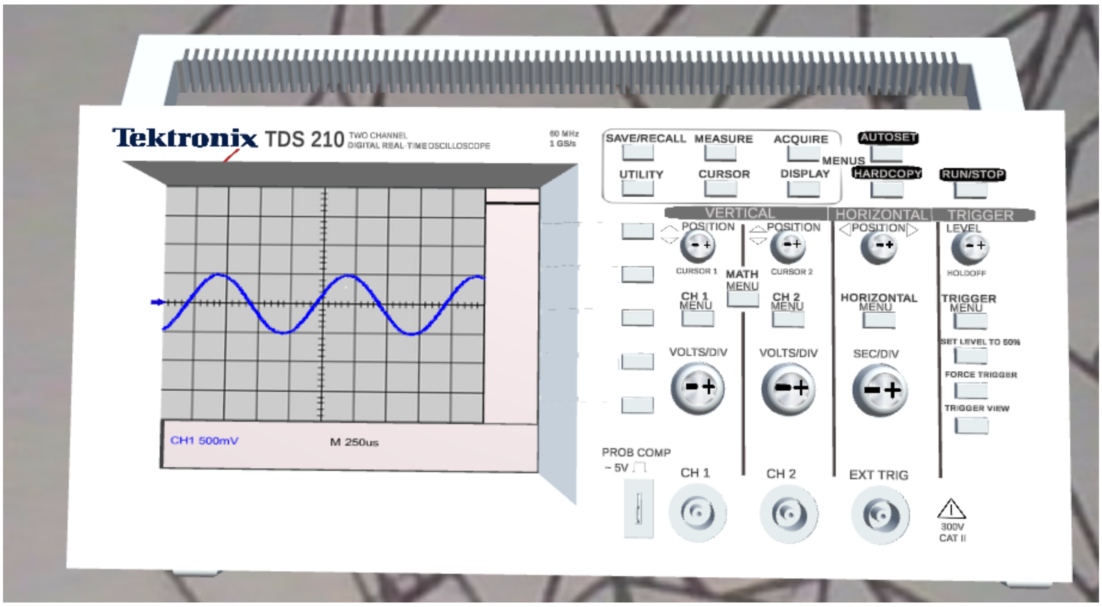

Figure 14. Waveform and resolution information on the AR display after turning on.

In this way students gain a comprehensive understanding of the signal currently captured and displayed on the physical oscilloscope. Consequently, they can modify parameters, such as V/div and s/div, by manipulating the corresponding knobs on the AR interface, aligning them with the specific tasks they need to accomplish.

Furthermore, students can access information about signal coupling, copying the process on an actual oscilloscope. Clicking the "*CH1 MENU*" button in the AR application reveals relevant information on the display's right-hand side (as shown in Figure 15).

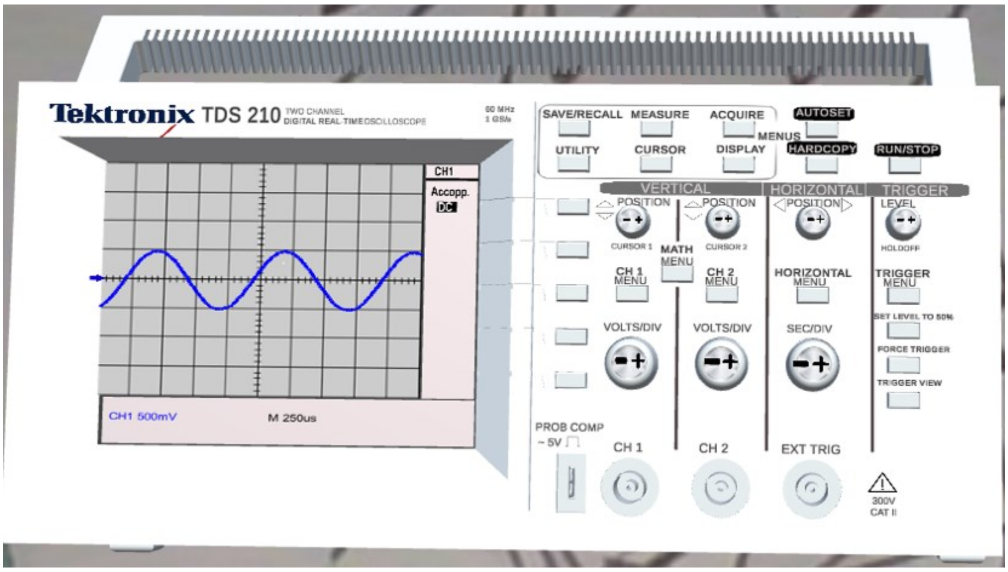

Figure 15. CH1 Menu Selection on the AR instrument.

For instance, the coupling type may be "*DC*." By turning the knobs associated with the "*CH1 MENU*" button, students can adjust the signal level (as depicted in Figure 16), shifting the signal vertically on the axis. This feature is particularly useful when students wish to display multiple signals on the screen without overlap.

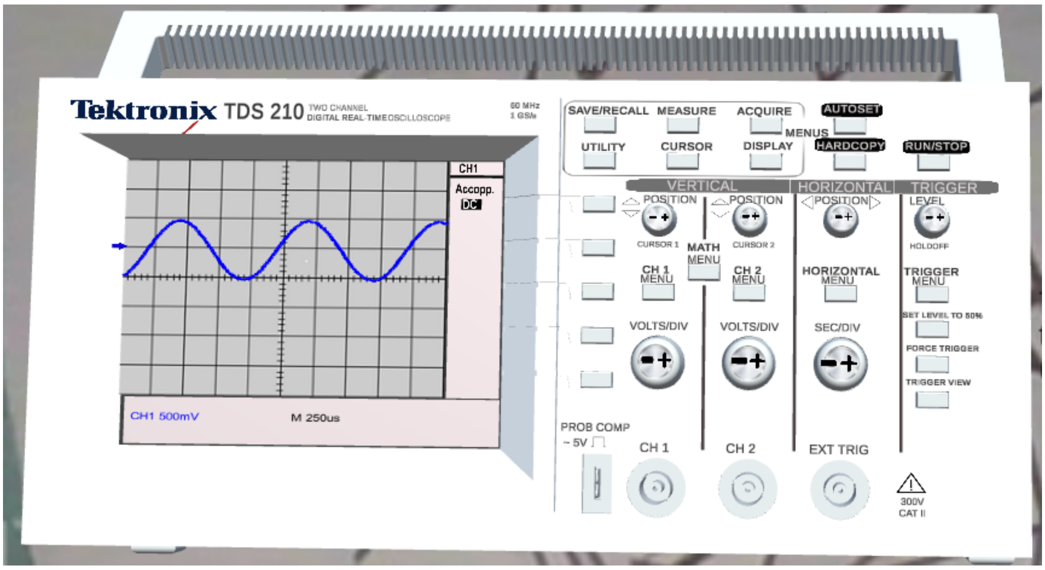

Figure 16. Signal level.

Additionally, the students have the capability to modify the trigger level and utilize cursors for measuring signal properties, mirroring the actions possible on a physical oscilloscope. Figure 17.a exemplifies the use of cursors to measure peak-to-peak amplitude, while Figure 17.b demonstrates how to measure the signal's period. Notably, there is a striking resemblance between the display within the AR application and that of the physical instrument in the laboratory.

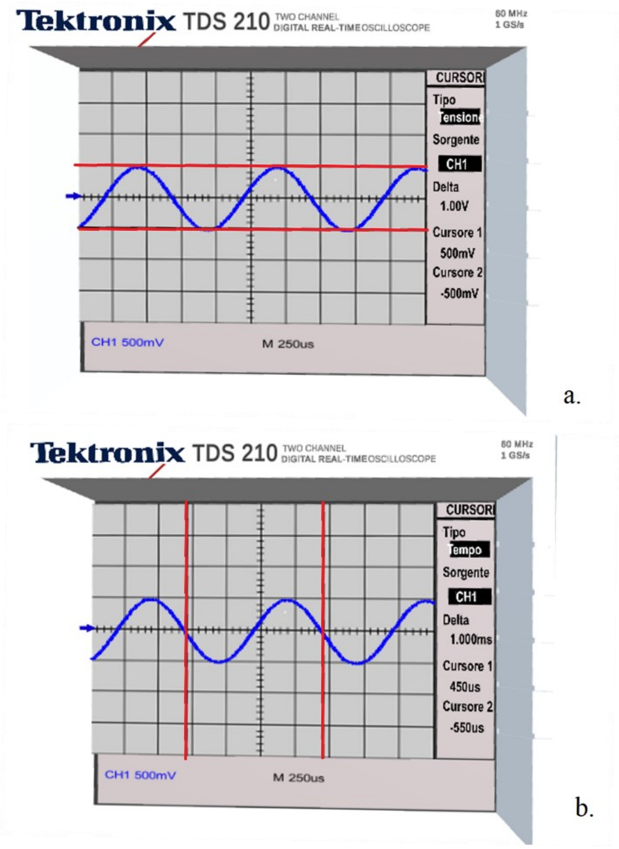

Figure 17. Evaluation of a) peak-peak amplitude and b) period of the signal.

Expanding upon the case study, a typical student exercise involves measuring amplitude and phase variation in the output signal of an RC filter circuit, specifically one with a cut-off frequency of 1.7 kHz. Figure 18 provides an overview of the setup in the physical laboratory, where channel 1 of the oscilloscope captures the input signal, and channel 2 displays the output signal from the filter.

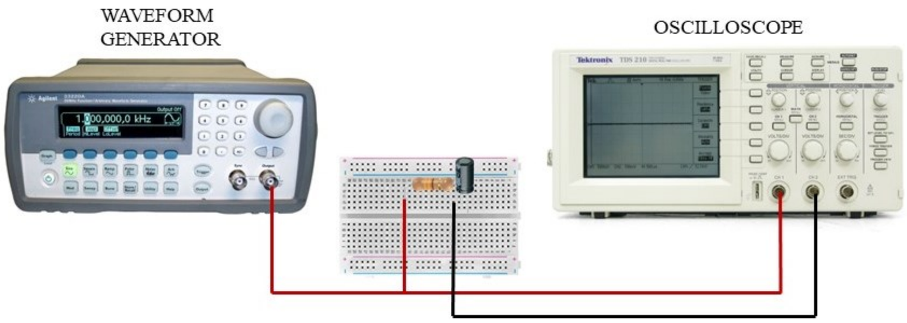

Figure 18. Laboratory setup in experiments with RC Filter.

Figure 19 further illustrates the results as the input signal's frequency varies. Figure 19.a exhibits nearly superimposed waveforms of both channels when a 200 Hz input sine wave is applied. As the input frequency goes up to 1 kHz (Figure 19.b), the output waveform is subjected to attenuation and delay compared to the input. Finally, at 5 kHz (Figure 19.c), the filter's effects are prominently evident, with significant attenuation and phase shift in the output waveform.

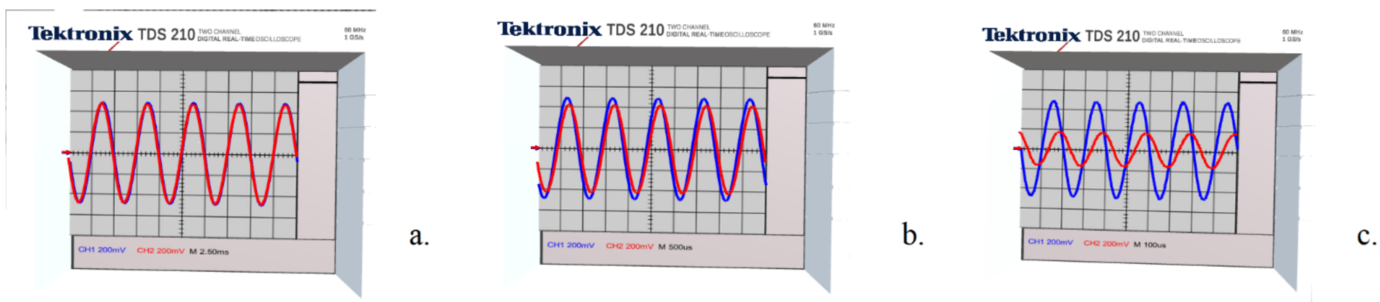

Figure 19. Evolution of signal output of RC filter: a) signal frequency input equal to 200 Hz, b) signal frequency input equal to 1 kHz, c) signal frequency input equal to 5 kHz.

Similar to the physical laboratory experience, students can employ cursors to measure the filter's gain and phase shift, as demonstrated in Figure 17.

In essence, this case study showcases how it's possible to mirror the real-world laboratory experiences, enabling students to gain practical knowledge and skills in a virtual environment that closely simulates their physical learning environment.

This example shows how a CPS for the measuring instruments can be realized, highlighting that instrument as Digital Twin acts in the same way as those in the real world.

Chapter 3 - Remote Control of Instruments for Safe Experiments

The solution proposed in paragraph 1.1 can be used in different contexts where remote control of an instrument is envisaged. In this section it shows how it’s possible to apply the method for physics experiments involving radioactive materials, sources of dangerous radiations.

A fundamental aspect of STEM (Science, Technology, Engineering, and Mathematics) laboratory activities is fostering students' problem-solving skills. These laboratory sessions serve as a platform for students to engage with STEM materials, conduct experiments, explore concepts, and make their own discoveries. In the context of physics, conducting experiments plays a pivotal role in comprehending the underlying physical phenomena [59].

However, it's important to recognize that certain experiments can carry a level of risk, particularly those involving potentially hazardous phenomena like radioactivity. In such cases, students must adhere to strict safety protocols and employ personal protective equipment to mitigate risks. Additionally, the presence of qualified personnel is often necessary to supervise and ensure the safe execution of these laboratory activities.

It's worth emphasizing that while these safety measures and requirements can be effectively implemented at the university level, they pose significant challenges when applied to high schools or primary schools [60]. The constraints and limitations faced by educational institutions at these levels make it considerably more difficult to provide the same level of safety assurance as universities can offer. This highlights the need for specialized resources, training, and a heightened level of vigilance to manage and mitigate risks effectively.

Leveraging the distinctive features and protocols inherent to the Internet of Things (IoT) paradigm offers a practical solution to create a clear demarcation between the student's laboratory setting and the actual experiment's physical environment. IoT technology proves to be an invaluable educational tool, as it enables seamless communication over the Internet or other networks/protocols among objects situated in disparate locations [61].

3.1 State of Arte

IoT essentially functions as a network of interconnected devices of diverse types and sizes, ranging from industrial systems and medical instruments to smartphones and sensors. These devices collaboratively share information, fostering real-time online control and monitoring [62], [63]. This capability holds immense potential for enhancing the educational experience within STEM (Science, Technology, Engineering, and Mathematics) laboratories and beyond.

By integrating IoT into the educational landscape, students can remotely access and interact with experimental setups located in separate physical spaces. This innovation not only enhances the flexibility of learning but also promotes collaborative and remote problem-solving. It allows students to perform experiments, gather data, and analyze results without being physically present at the experiment site. This is particularly beneficial in scenarios where experiments involve hazardous materials or complex equipment, as it ensures the safety of the students while providing them with hands-on learning experiences.

Furthermore, IoT enables real-time data sharing and feedback, making it possible for educators to monitor student progress and provide guidance in real-time. It also encourages collaboration among students, promoting a more dynamic and interactive learning environment.

Besides the things interconnection, other technologies supportive of IoT can be considered, such as Augmented Reality (AR). Ar involves an alteration of reality, thanks to virtual information overlapped on the reality felt by senses. As described in [64], this technology is beginning to increase its exploitation and impact in STEM learning.

Thanks to the technologies discussed earlier and it has been implemented a mixed-reality solution that combines Augmented Reality (AR) with IoT communication protocols. This innovative approach serves as a means to conduct laboratory activities with a potential risk factor safely.

The core components of this solution comprise an AR mobile application and a microcontroller-based mock detector. Together, these elements enable students in a classroom setting to manipulate a detector in real-time, relative to a radioactive source located in a remote laboratory. The detector captures the corresponding gamma-ray energy spectrum, which is then transmitted using an IoT protocol. Subsequently, the spectrum data is displayed on the students' mobile phones.

Notably, the versatility of this proposed solution extends beyond radioactive spectrum measurements. It can be effectively employed in various application domains involving hazardous materials or unsafe environments. For instance, it is adaptable for handling nuclear waste, where physical proximity to the materials is a concern. Similarly, this technology can be employed in healthcare settings, particularly in the use of diagnostic tools based on X-rays in hospitals.

This mixed-reality solution offers several advantages. Firstly, it ensures the safety of students by allowing them to engage in experiments with potentially hazardous materials while being physically separated from the source of risk. Secondly, it enhances the learning experience by providing real-time data acquisition and analysis, promoting active student participation. Additionally, it facilitates remote collaborations and knowledge sharing, enabling educators and students to work together seamlessly, regardless of their physical location.

In summary this solution, which integrates AR and IoT technologies, represents an innovative approach to conducting laboratory activities in a safe and engaging manner. Its adaptability to various domains with safety concerns, coupled with its potential for remote learning and collaboration, positions it as a valuable tool in modern education and scientific research.

In literature there is no existing example of Augmented Reality (AR) utilization that enables students to reenact a laboratory experience by directly manipulating real instruments and conducting real-time, non-simulated experiments. A noteworthy AR application in chemistry education is presented in [65], allowing students to visualize molecules from various perspectives, observe atomic structures within matter, and grasp abstract chemical concepts. However, this solution lacks interaction with actual chemical substances, compounds, or laboratory equipment. The outcomes are derived from approximated models, and certain aspects of real experiments remain unattainable through simulation, regardless of model accuracy.

While remote-controlled instruments and tools are notably employed in surgery, exemplified by the Da Vinci robot [66], [67] the associated technological requirements hinder their widespread adoption for educational purposes.

3.2 Proposed Solution

The primary focus revolves around addressing the challenge of enabling students to safely engage in experiments that involve potentially hazardous conditions, such as those using radiation sources. These experiments typically necessitate the supervision of qualified personnel and specific laboratory conditions to ensure the students' safety. Unfortunately, these requirements might not always be met, especially in non-university educational settings, which can deprive students of valuable learning experiences. While the proposed solution can be adapted to various physics experiments and other STEM subjects.

To ensure the safe execution of experiments in this context (Fig. 20), the first crucial step involves creating a clear separation between two environments: the "*Safe Environment*" where students and teachers are located, and the "*Real Environment*" housing the actual measurement instruments, dangerous materials, and laboratory equipment. Effective communication between these environments is paramount to ensure the alignment of actions in the safe environment with those occurring in the remote laboratory. This approach enables students to virtually experience the laboratory activity as if they were physically present in the real environment.

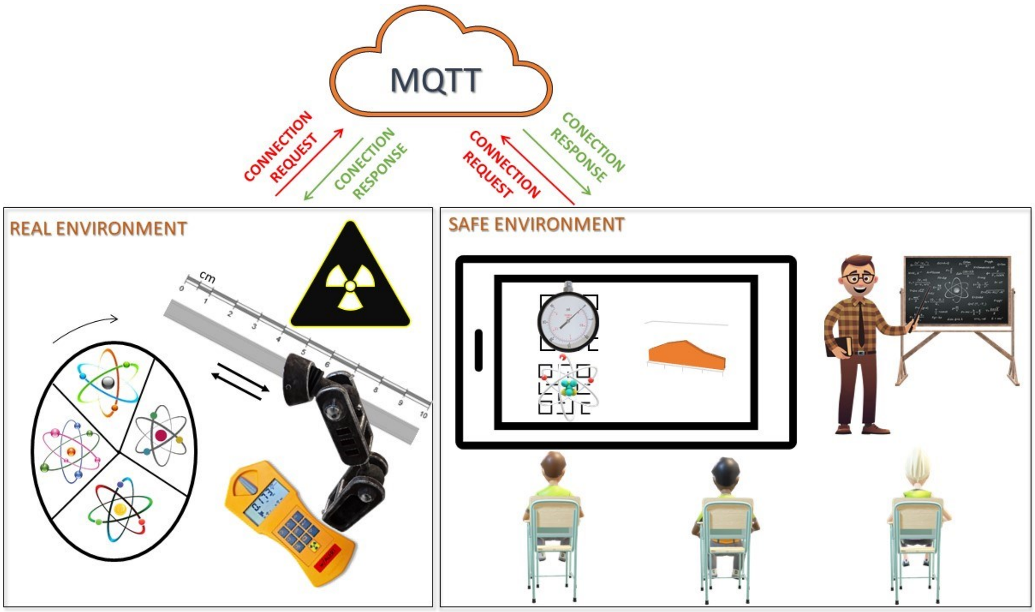

Figure 20. Proposed solution for safe physics experiments: the environment where students can carry out safe AR experiments is specially separated from actual laboratory with hazard condition. Communication between the environments is assured by means of IoT protocol

- **Safe Environment**: this environment comprises the classroom where students and teachers are located. To safely manipulate actual detectors and radioactive sources, all interactions are mediated through a specialized mobile app based on Augmented Reality. This app renders a faithful representation of the experimental equipment when the fake detector and radioactive source (both represented by specific targets) are framed through the mobile phone's camera. The detector target incorporates an embedded system that measures its distance and inclination concerning the fake source. These measurements are transmitted to the laboratory to adjust the actual source and detector positions. Within the app, students can request and view the measured values, such as the energy spectrum of the radioactive source.
- **Real Environment**: in this environment, the remote laboratory houses the actual measurement instrument (the detector), radioactive source, and a motion system for safe positioning. The motion system can utilize stepper motors, a robotic arm, or any suitable mechanism to move the measurement instrument concerning the radioactive source. Additionally, another motion system can be employed to switch between different radioactive sources, such as a rotating flange supporting various materials, selected based on the specific angular

position corresponding to the framed fake source. In the real environment, the required measurements are conducted, and the results are transmitted back to the safe environment for display on students' mobile phones.

- **Communication**: The seamless connection between the safe and real environments is established through communication protocols typical of the Internet of Things (IoT) paradigm, ensuring scalability and integration within the broader network of interconnected devices, and specifically MQTT.

3.3 Case Study

To evaluate the practicality of the proposed approach, it has been successfully implemented a prototype of a mixed-reality solution designed for the secure execution of gamma-ray energy spectrum measurements. However, before delving into the case study, it's essential to provide some context regarding the type and level of ionizing radiation involved. Even within school premises, students are exposed to various sources of ionizing radiation, including X-rays, gamma rays, and electron radiation from materials like concrete walls, as well as alpha radiation originating from radon in the ground and cellars. These sources typically emit radiation at levels that are not harmful during normal living or measurements.

From an educational perspective, it would be both fascinating and instructive to allow students to conduct measurements involving such low levels of radiation. This hands-on experience would not only familiarize students with the instruments but also engage them with the underlying scientific principles. However, equipping schools with the necessary equipment to perform these operations, such as a gamma-ray detector similar to the one used in the case study (which costs approximately 3500 €), could be cost-prohibitive.

In contrast, the prototype implementation of the mixed-reality solution comes at a considerably lower cost, totaling around 300 €. The hardware components for the safe environment are even more affordable, amounting to only 60 €. This makes it a cost-effective option for all schools and opens the door to rental contracts for the measurement service, further reducing the financial burden. Furthermore, the solution allows for the exclusion of any radiation sources that pose significant health risks.

While harmful radiation sources are fortunately uncommon in everyday life, their associated risks can pique students' interest, much like in other educational areas. This engagement and real-world relevance can enhance the learning experience and foster a deeper understanding of radiation and its effects [68], [69].

In the next subsection it will be provided detailed descriptions of the hardware and software architectures of both the safe and real environments, along with an overview of the conducted experiments and the detector used. This context sets the stage for a comprehensive understanding of the prototype's implementation and its potential impact on education in STEM fields.

3.3.1 Gamma Ray Energy Spectrum Measurements

Gamma rays represent the highest energy segment of the electromagnetic spectrum. While they share fundamental characteristics with other forms of electromagnetic radiation like X-rays, visible light, infrared, and radio waves, they are distinct due to their exceptionally short wavelength, which results in their high energy levels. Gamma rays are frequently emitted by radioactive nuclei, falling within the energy range of a few keV to about 10 MeV, aligning with the typical energy levels of atomic nuclei [70].

The interaction of gamma rays with matter differs fundamentally from that of charged particles such as electrons or alpha particles. Charged particles continuously deposit their energy into the absorbing medium, following well-defined paths through various substances. In contrast, gamma rays act sporadically, and their intensity is never reduced to zero, even when passing through progressively thicker layers of material [71]. Handling a gamma-ray source without the necessary precautions can be hazardous.

The measurement of gamma rays is typically conducted using a detector, which is essentially an instrumental system designed to determine the energy distribution of gamma photons in differential form. The data generated by a gamma ray detector is commonly represented as a two-dimensional plot, showing pulse frequency against the energy of the gamma radiation, commonly referred to as the gamma spectrum. The interpretation and analysis of this spectrum provide the essential information required

for the qualitative and quantitative identification of gamma-emitting radionuclides [72].
A gamma spectrometer comprises three primary components [73]:

1. **Detection system**: this includes the detector and a shield. When incident gamma photons interact with the detector, they turn down a portion or all of their energy, depending on the type of interaction. The detector's role is to convert this energy into a proportional electric charge. The shield serves to minimize structural background noise caused by environmental gamma radiation. Additionally, it influences the spectrum's shape due to the backscattering of detector photons.
2. **Pulse analysis system**: a gamma ray detector not only records a certain number of pulses but also categorizes them based on the amplitude of their energy levels. To achieve this, the electrical pulses leaving the detector must be amplified and directed to an amplitude analyzer. The number of pulses within each energy range is then stored in a dedicated memory unit.
3. **Data recording and processing system:** the data stored in the memory unit are subsequently extracted using specialized recording, printing, or display units. Moreover, the memory unit can be linked to a computer for comprehensive data analysis and processing.

In theory, when a monochromatic gamma-ray beam interacts with a detector, it should yield an electron distribution characterized by one or more monoenergetic groups and a continuous distribution, commonly referred to as the "ideal spectrum." However, real-world spectra deviate significantly from this ideal shape due to various factors [74].
A crucial aspect of a gamma spectrometer is its efficiency, which can be adversely affected by changes in the distance and orientation of the detector relative to the radiation source. Thus, it is advisable for educational purposes to allow students to assess how these factors impact the spectrometer's performance [75]–[77].

3.3.2 Hardware Architecture

The hardware architecture consists of two distinct environments: the safe environment and the real environment, each serving specific purposes and functions.

In the **Safe Environment**, the hardware components are primarily aimed at enabling distance and orientation measurements concerning radioactive sources. These measurements are essential for maintaining safety standards. To accomplish this, two commercial electronic boards manufactured by STMicroelectronics were selected for the task: the *X NUCLEO 53L0A1* [78] and the *X NUCLEO IKS01A2* [79].

The first board is equipped with a VL53L0X Time of Flight (ToF) sensor [80], which offers precise distance measurements. This sensor is known for its cost-effectiveness and boasts a measurement accuracy of less than 3% in high-accuracy configurations, with a maximum range of 2 m. Additionally, it utilizes a 940 nm VCSEL emitter, allowing it to cover long distances while maintaining immunity to ambient light and robustness against optical crosstalk [80].

For inclination measurements relative to the vertical direction, the *X NUCLEO IKS01A2* board employs an *LSM6DSL* triaxial acceleration sensor [81]. It calculates the desired angle by analyzing gravity acceleration projections onto the sensor's reference frame. The *LSM6DSL* combines a 3D digital accelerometer and a 3D digital gyroscope, known for low power consumption and resistance to mechanical shock. The LSM6DSL has full-scale acceleration ranges of ±2/±4/±8/±16 g and angular rate ranges of ±125/±250/±500/±1000/±2000 dps [81].

Both boards are connected to a NUCLEO L152RE board from STMicroelectronics [82], which hosts an STM32L152RE microcontroller. This microcontroller manages the measurement operations, communicates with the sensors via the Inter-Integrated Circuit (I2C) protocol, processes the collected data to derive inclination information, and sends the results through Universal Synchronous-Asynchronous Receiver/Transmitter (USART) to an ESP32 microcontroller from Espressif Systems [83] mandated to the implementation of MQTT protocol. The ESP32 is mounted on an ESP32-DevKITC-V4 board, which is commonly used for IoT applications. It features integrated Wi-Fi connectivity, enabling direct internet access through a Wi-Fi router. This microcontroller is chosen for its low current dissipation, making it suitable for battery-powered and wearable electronics applications. The Wi-Fi module on the ESP32 supports data rates of up to 150 Mbps and provides 20 dBm output power at the antenna, ensuring a wide physical range [83].

Figure 21.a shows a block diagram of the hardware architecture of the devices involved in the Safe Environment, while Figure 21.b shows the target for the reproduction of the gamma ray detector with the embedded system inside.

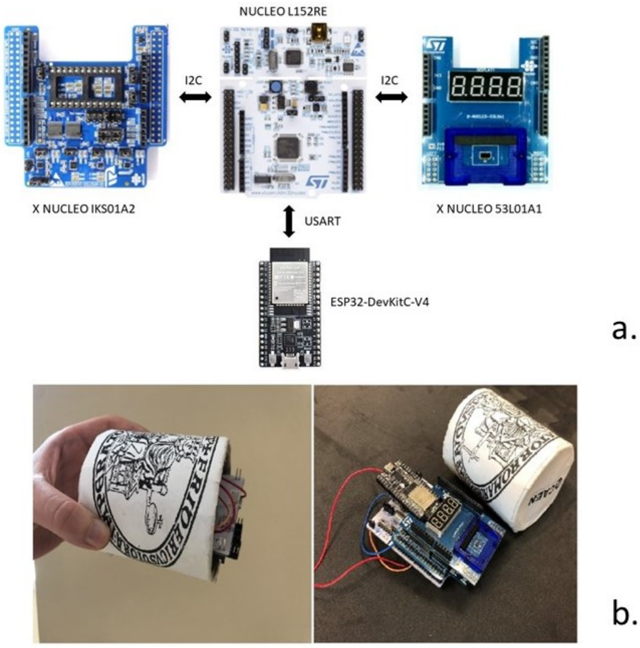

Figure 21. Hardware architecture for the safe environment, composed by a microcontroller, an inertial sensor, a time of flight sensor, a Wi-Fi module (a) and target for AR app (b).

In the **Real Environment**, aside from the radiation sources, the main components include a gamma-ray detector and a motion system. The selected gamma-ray detector is the i-Spector Digital, developed by Caen S.p.A [84]. It offers an integrated multi-channel analyzer (MCA) and optional wireless connectivity based on the LoRaWAN protocol. This compact unit can be configured with different silicon photo-multiplier (SiPM) areas and features a preamplifier stage, integrated power supply for SiPM biasing with temperature feedback, a shaper, and a full-featured MCA based on an 80 MSps, 12-bit ADC, and digital charge integration algorithm. The i-Spector Digital can be controlled through Ethernet and provides both an analog amplified signal and the measured 4k channels energy spectrum [84].

The real environment also incorporates two motor drivers, *XNUCLEO IHM01A1* by STMicroelectronics, which are based on L6474 current control and used to drive two stepper motors for angular and linear movement, respectively. These controllers operate the motors through an H-bridge circuit. In this circuit, the appropriate activation of two pairs of electronic switches allows to select the direction of the current flowing in the load placed on the output terminals (the topology is called bridged because the load is located between two branches of the circuit) and, consequently, the rotation direction of the motor [84]. Moreover, the switching period and duty cycle allow to modulate the current flowing through the motors thus allowing to select their rotation speed. For inclination movement, a MotionKing 17HS4401 motor is used, featuring an angular step of 1.8 degrees, nominal current of 1.7 A, and a step accuracy of 5% [85]. For linear movement, a 500mm linear guide with a 1cm step is chosen, equipped with the same motor mentioned earlier. The motor drivers are managed by a NUCLEO L152RE board, connected to the motor control shields via the Serial Peripheral Interface (SPI) protocol. It's worth noting that the standard configuration of the IHM01A1 motor drivers doesn't allow the simultaneous control of multiple motor drivers from a single microcontroller. Therefore, an alternative configuration with resistors placed on the shields has been adopted [86].

The NUCLEO L152RE board is connected via USART protocol to an additional ESP32 microcontroller. This ESP32 receives distance and angular data transmitted from the Safe Environment and utilizes this information to control the motors in the Real Environment effectively.

Figure 22 shows a block diagram of the hardware architecture of the devices involved in the Real Environment.

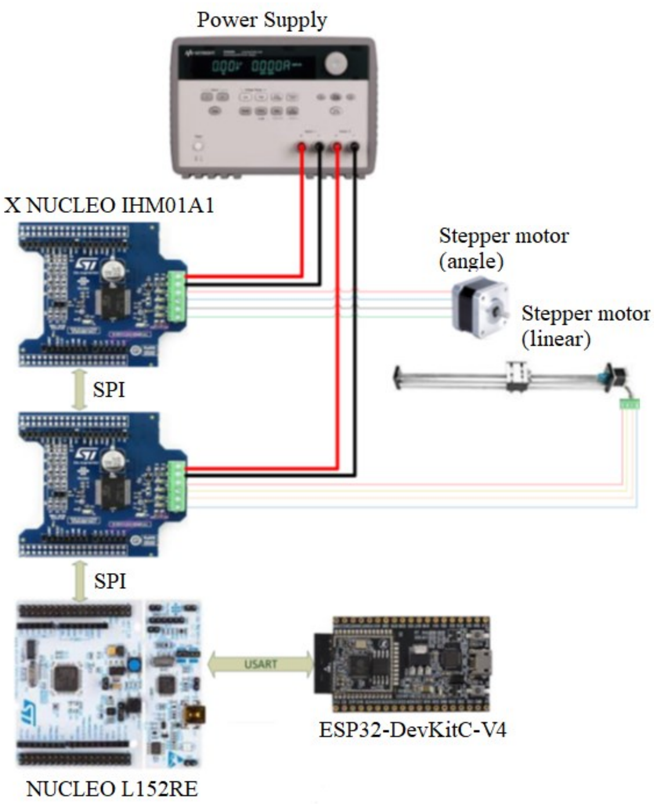

Figure 22. Hardware architecture for the real environment, composed by a power supply, two motor drivers, a microcontroller, Wi-Fi module and two stepper motors, for linear and angular movements, respectively.

3.3.3 Software Architecture

The firmware implemented on the management boards as well as the main integrated development environments exploited for the realization of the proposed case study are presented and described in the following. As for the Safe Environment, the main goal has been the implementation of a mobile app capable of making the students relive the laboratory experience as they were using the actual detector. As for Real Environment, the attention has been focused on the movement of actual detector and the transmission of the measured gamma ray energy spectrum.

3.3.3.1. Safe Environment

An Android application has been developed using the Unity 3D environment, designed to provide students with a realistic visualization of a gamma-ray detector and radioactive sources. The goal was to create a virtual representation that closely resembles their real-world counterparts. To achieve this, the app relies on the placement of specific markers within the virtual environment.

The app also offers the functionality to request and view the energy spectrum of the radioactive source. This spectrum is updated at regular intervals of 10 seconds through a dedicated menu. Furthermore, users have the option to clear the spectrum samples, effectively resetting the graph, and to exit the application.

One important feature of the app is its ability to reset the energy graph whenever a new source, different from the previous one, is framed. This ensures that each measurement starts fresh and is not influenced by previous data.

In the case of the gamma-ray detector, a meticulous process was undertaken to capture its 3D representation. This was achieved, as mentioned in 1.1.1.1 paragraph, using a non-contact Laser ScanArm by FARO, a sophisticated measurement system capable of capturing the object's shape and size.

The scanning operation involved capturing each internal and external component of the detector. Once all components were scanned, they were integrated into a cohesive whole using the SolidWorks CAD system. The resulting 3D object was then imported into the Unity environment. Within Unity, an algorithm was developed to enable users to access an exploded view of the detector. This functionality is accessible through a dedicated button on the display (as depicted in Figure 23).

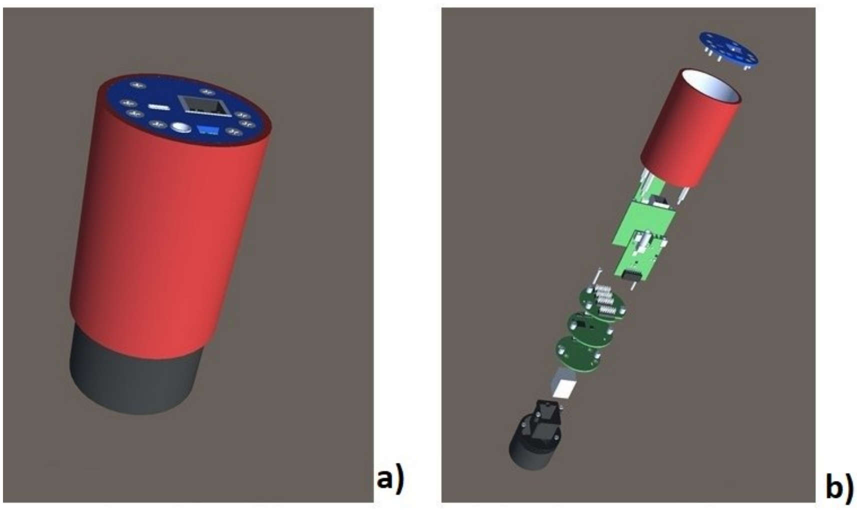

Figure 23. Results of the gamma ray detector scan through Laser ScanArm (a) and exploded view allowing students and teacher to visualize the internal components of the detector (b).

This exploded view is a crucial aspect of the app as it allows students to gain a deeper understanding of the detector's operating principles. By dissecting the object into its electronic components, students can explore and comprehend the concepts they have learned in their theoretical lectures.
In order to effectively integrate the detection and recognition of markers for detectors and sources within the app, it has been employed an open-source tool called "*Vuforia Object Scanner*," provided by Vuforia. This tool is instrumental in defining and identifying the corresponding markers. Essentially, the markers need to be observed from various perspectives to facilitate the training of a software component responsible for their recognition. To visually assess the quality of this training, we've utilized a graphical representation in the form of a dome. Different parts of this dome are filled with a green color to indicate successful viewpoint recognition (as depicted in Figure 24).

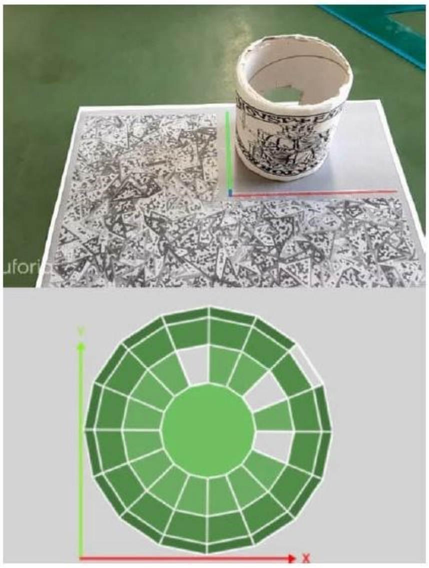

Figure 24. Training stage of detector marker recognition by means of Vuforia object scanner: on the top is represented the marker to scan while on the bottom the result of the scanning.

This process has significantly enhanced the recognition capabilities of the gamma-ray detector marker. It's now capable of accurate recognition even when the marker's inclination varies. This ability is crucial for users who need to assess changes in the spectrum and, therefore, may need to manipulate the marker's orientation.

As mentioned earlier, the detector marker serves the purpose of measuring both distance and inclination concerning the representation of the radioactive source. These measured parameters are subsequently transmitted to the Real Environment. To obtain these values, we've leveraged the hardware architecture outlined in the previous paragraph. The algorithm responsible for extracting angle and distance data from the radioactive source has been implemented on the STM32L152RE microcontroller.
The algorithm, as shown in Figure 25, initially involves the initialization of the *X NUCLEO 53L0A1* and *X NUCLEO IKS01A2* boards, including the configuration of parameters like baudrate and data format used for USART communication. Assuming no errors occur during the initialization phase, data related to distance and the components of gravity acceleration are collected from the sensors. The inclination angle is subsequently computed based on the acceleration data across all three axes, utilizing the following equation:

$$\vartheta = tan^{-1}\left(\frac{A_x}{\sqrt[2]{A_y^2 + A_z^2}}\right) * \frac{180}{\pi} \qquad (1)$$

Obtained results are, finally, sent via USART to the ESP32 microcontroller, on which the MQTT communication protocol is implemented to send such data to the Real Environment.

```
Initialize X NUCLEO 53L0A1 and X NUCLEO IKS01A2 boards;
Setting parameters for USART communication.
LOOP Process
if X NUCLEO 53L0A1 board status and X NUCLEO IKS01A2 is ok? then
    while true do
        Receive distance and accelerometer data from shields;
        Evaluate angle from acceleration projections on the three axes;
        Send data via USART to ESP32 microcontroller
    end while
else
    stop the execution
end if
```

Figure 25. Algorithm for distance and inclination Measurements in Safe Environment

This comprehensive approach ensures that our app can effectively interact with the markers, measure the necessary parameters, and provide users with the crucial information they need to evaluate changes in the spectrum.

3.3.3.2. Real Environment

Within this operational environment, data originating from the Safe Environment needs to be replicated accurately. To achieve this, it has been employed two stepper motors for specific functions. The first motor is responsible for driving a linear guide, enabling precise distance adjustments from the radiation source. Meanwhile, the second motor facilitates tilt movements (as illustrated in Figure 26).

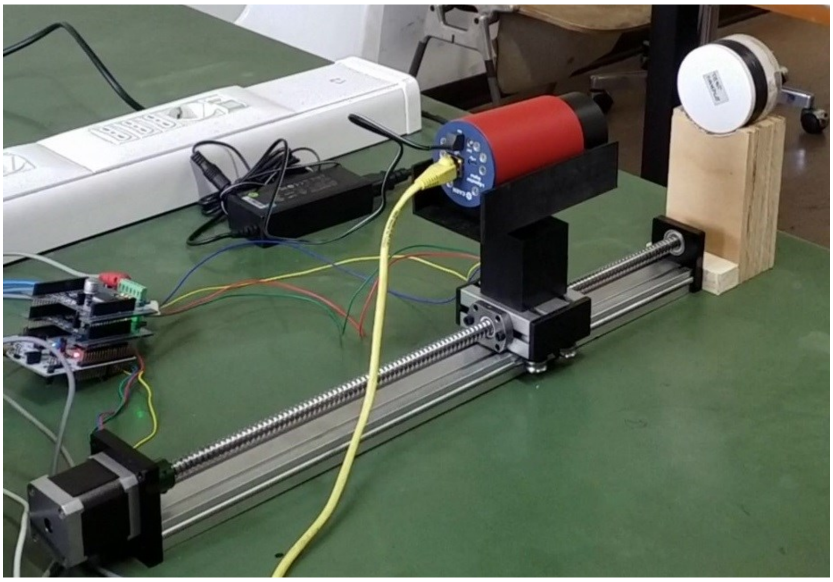

Figure 26. Real environment: the gamma ray detector placed on a system of stepper motor remotely controlled by user that allows the movements towards the radiation source.

The control of these two stepper motors is entrusted to the drivers defined in the previous section.

The values corresponding to the desired distance and inclination parameters are received by the ESP32 microcontroller, which is situated within this environment. Subsequently, these values are transmitted to the STM32L152RE microcontroller via the USART protocol. The microcontroller, in turn, converts these received values into specific motor steps. These steps are then sent to the two drivers utilizing the I2C protocol, effectively translating them into physical motor movements. It's important to note that the step values are calculated in accordance with the dimensions of the guides and the maximum current capacity supported by the drivers.

Upon system initialization, the algorithm outlined in Figure 27, embedded within the *STM32L-152RE* microcontroller's firmware, is responsible for returning the gamma-ray detector to its initial position in terms of both distance and inclination. To achieve this, the last recorded values for distance and inclination are written into the microcontroller's EEPROM memory. This action effectively restores the two guides to their starting positions.

```
Initialize the two X NUCLEO IHM01A1 boards.
LOOP Process
if boards status ok? then
    Read the stored values from EEPROM Memory to take
    the gamma ray detector to its initial position (minimum
    distance and inclination respect to the source)
    while true do
        Read data sent by ESP32 microcontroller.
        if Difference between actual and prior value is
        greater than or equal to 1 cm then
            Actuate received value;
            Save values to EEPROM memory.
        end if
    end while
else
    stop the execution
end if
```

Figure 27. Algorithm to Actuate Angle and Distance Sent by Safe Environment

Subsequent control over the detector's position and rotation is executed by utilizing values received by the ESP32 microcontroller. Furthermore, to prevent flickering or erratic movements due to imperfect marker handling, adjustments are only made when the difference between two consecutive distance values equals or exceeds 1 cm. This measure ensures smoother and more stable movements while maintaining the desired accuracy in the replication of data from the Safe Environment.

3.3.3.3. Remote Communication

In this section, it will be described the process of displaying the spectrum data generated by the gamma-ray detector within the Android app. The gamma-ray detector transmits its data using the HTTP protocol, necessitating the development of an algorithm to convert these HTTP messages into MQTT format before dispatching them to the Safe Environment. The algorithm was designed and implemented within the Node-Red environment, as illustrated in Figure 28.

For every request, whether for accessing available spectrum data or resetting the system by students, an associated HTTP command is issued. The workflow,

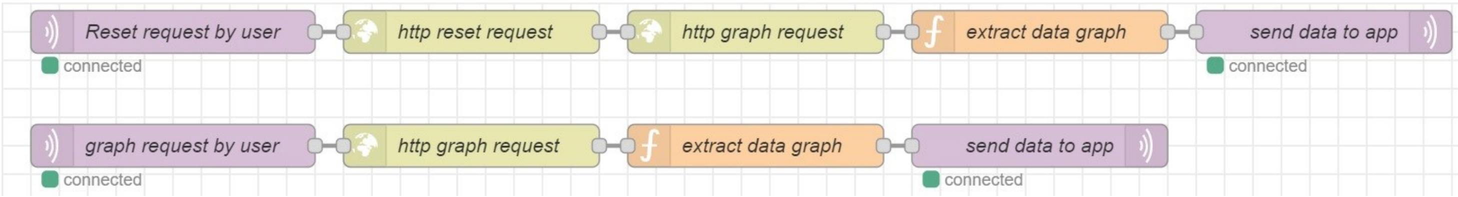

Figure 28. The developed node-red flowchart that converts MQTT message in HTTP message to allow communication between the gamma ray detector and AR application.

embodied by the Node-Red algorithm, then waits for the instrument's response. Once the response is received, it undergoes a meticulous processing phase using a dedicated function. The processed data is subsequently forwarded to the AR application.

The implementation of this function is indispensable due to the format of the data provided by the gamma-ray detector, which includes alphabetic characters preceding the numerical samples. To ensure compatibility with further analysis, these alphabetic characters are discarded, leaving only the numerical data array intact, as illustrated in Figure 29.

{ "command" : "GET_SPECTRUM", "Result": "ok", "ErrorCode":0, "Reason":"", "data" : [0,0,0,0,0,0,0,0,0,0,0,0,0,0,0,0,0,0,0,0,0,0,0,0,0,0,0,0, …, 65,82,72,101,77,76,97,98,32,115,117,99,97,97,97,………,76,101,111,112,111,108,100,111,32,65,110,103,114,105,115,97,110,105,32,118,117,111 108,101,32,102,97,114,32,98,97,110,100,105,114,101,32,117,110,32,112,111,115,116,111,32,100,97,32,97,115,115,111,99,105,97,116,111,32,105 110,32,73,78,71,45,73,78,68,47,49,50,32,112,101,114,32,108,97,32,109,111,103,108,105,101,32,65,110,110,97,114,105,116,97,32,84,101,100,101 ,115,99,111,………..,0,1,1,0,0,0,0,0,0,0,0,0,0,1,0,1,0,0,0,1,0,0,0,0,0,0,0,0,0,0,0,0,1,1,0,0,1,0,2,1,0,0,0,1,0,1,0,0,0,0,1,0,0,0,0,1,0,0,0,1,2,2,1,0,0,1,2, 0,0,0,0,1,0,750] }

Figure 29. Example of message provides by gamma ray detector as http answer.

Regarding the use of the MQTT protocol, a private broker was selected to facilitate communication. This decision was informed by several advantages, including immunity to issues such as high data traffic, loss of connection, and service suspension. To facilitate this, the Eclipse Mosquitto Software was employed to operate a local broker on a personal computer.

While it may appear simpler to transmit data directly to the Safe Environment via the HTTP protocol since the measurement instrument communicates using this protocol, adopting MQTT introduces a significant advantage. MQTT's "*one-to-many*" communication capability ensures that all students subscribing to the relevant *topic* can simultaneously receive data from the instrument, all without adding any unnecessary network overhead.

It is possible to say that the transition from HTTP to MQTT within the Node-Red environment allows for efficient and synchronized data distribution to multiple recipients, such as students using the AR application, thereby enhancing the overall experience and utility of the system.

3.3.4 Experimental Results

The performance evaluation of the proposed solution involved a comprehensive series of tests conducted within the context of the chosen case study. Initially, a primary set of tests focused on assessing the delay and stability of communication between the Safe and Real Environments through the MQTT protocol. The implementation of a private broker dedicated exclusively to managing messages for the specific application ensured that message delays never exceeded 70 milliseconds. This was consistent across messages related to distance and inclination control, regardless of the network's load conditions.

Furthermore, the evaluation encompassed a meticulous examination of the disparities between nominal, measured (in the Safe environment), and actuated (in the Real environment) distances and angles. To achieve this, both marker and actual detectors were affixed to rulers and protractors. Nominal distances ranged between 10 and 40 cm, corresponding to the linear track's stroke, while angle values spanned from -30° to 30°. For each value, 30 measurements were conducted, and the results, expressed in terms of both the average (Δ) and experimental standard deviation (σ), were documented in Table 1 for distances and Table 2 for inclination.

Table 1. Average and experimental standard deviation among either measured or actuated and nominal distances.

Nominal distance [cm]		**10**	**20**	**30**	**40**
Safe	Δ	-0,8	-0,4	0,1	0,9
	σ	0,7	1,4	1,5	1,0
Real	Δ	1,2	-1,4	1,6	1,1
	σ	2,0	1,2	2,4	2,4

Table 2. Average and experimental standard deviation among either measured or actuated and nominal angles.

Nominal angle [°]		-30	-20	-10	0	10	20	30
Safe	Δ	-0,4	0,2	-0,2	-0,3	0,2	0,3	-0,1
	σ	1,2	1,4	0,9	1,1	1,3	0,8	1,6
Real	Δ	0,9	1,2	-0,7	-0,8	0,6	-1,0	1,4
	σ	1,8	2,2	1,5	1,6	1,8	1,9	1,7

The table 1 presents the average (Δ) and standard deviation (σ) for distance measurements at different nominal distances (10 cm, 20 cm, 30 cm, and 40 cm):

1. In the “Safe” Environment, the average values demonstrate a slight underestimation at 10 cm and 20 cm, followed by a slight overestimation at 30 cm and 40 cm.
2. The standard deviation values in the “Safe” Environment show variability in the measurements, with higher variability observed at 30 cm and 40 cm.
3. In the “Real” Environment, the mean error values indicate an overestimation across all nominal distances, with larger deviations seen at 30 cm and 40 cm.
4. The standard deviation values in the “Real” Environment demonstrate varied levels of variability, peaking at 40 cm.

The table 2 illustrates average (Δ) and standard deviation (σ) for angle measurements at different nominal angles (-30° to 30°).

1. In the “Safe” Environment, the average values suggest a slight underestimation for most angles, with deviations close to zero, except for -20° and 20°.
2. The standard deviation values in the “Safe” Environment show consistent variability across all nominal angles.
3. In the “Real” Environment, the mean error values indicate an overestimation for most angles, with larger deviations observed at -10°, 0°, and 30°.
4. The standard deviation values in the “Real” Environment exhibit varying levels of variability, peaking at 20°.

The average and standard deviation values do not affect the laboratory experience, as the signal spectrum of the radioactive source was found to be consistent with that is expected.

Finally, the functionality of the proposed case study was rigorously assessed. To enhance clarity, a compilation of illustrative images depicting a typical application scenario is presented in Figure 30.

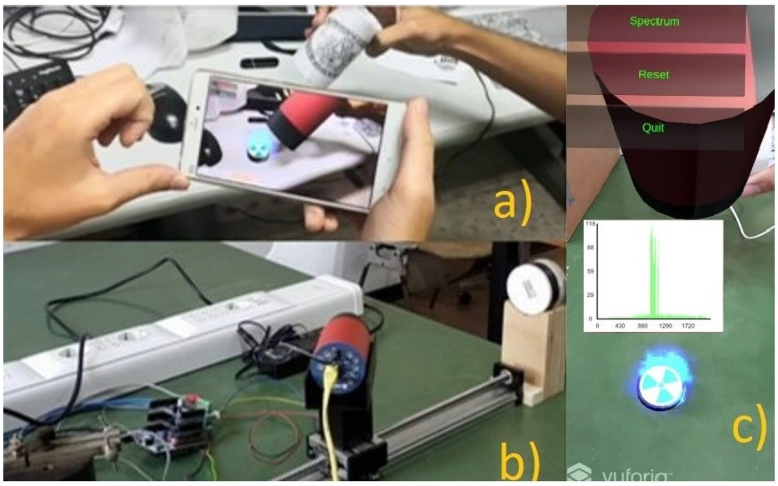

Figure 30. The implemented prototype of the proposed solution where in a) it's shown the safe experimental operation, while in b) the real environment that is remotely controlled and finally in c) the interface of the suitable application developed for the measurements of gamma ray energy spectrum.

Specifically, Figure 30.a showcases the targets that users must align with their smartphone cameras to replicate the detector and radioactive sources in the Safe environment. In opposition, Figure 30.b illustrates the corresponding configuration of stepper motors and the actual gamma-ray detector in the Real environment. In Figure 30.c, the mobile app's interface is featured, complete with a button menu enabling users to request the energy spectrum, which is seamlessly displayed within the same interface. Importantly, the typical delays observed between requesting the spectrum and its representation were consistently below 200 milliseconds, ensuring an uninterrupted and satisfying user experience.

SECTION 2 - IoT FOR LOCALIZATION AND MONITORING

The second Section deals with the definition and implementation of methods exploiting the enabling technologies of Internet of Things for localization and monitoring applications; to this aim, the attention is focused on smart sensors, low-power communication protocols and artificial intelligence . A first solution explores Bluetooth Low-Energy Fingerprinting, a cutting-edge approach, to implement a Passive Entry/Passive Start (PEPS) system for terrestrial vehicles; a suitable measurement method, comprising a positioning algorithm, filtering algorithms, and classification using K-NN, has been defined and implemented. The study meticulously addresses challenges, such as spatial orientation, data filtering techniques, and network topology, ensuring remarkable accuracy. Through this method, the system achieves a global accuracy of 98.5%, distinguishing whether the driver is inside or outside the vehicle with remarkable precision.

Subsequently, a Structural Health Monitoring (SHM) systems, based on Micro-Electro-Mechanical Systems (MEMS) technology, will be presented. The proposed solution represents a novel approach employing redundant configurations of cost-effective MEMS accelerometers and Kalman Filter techniques. Through rigorous testing, the method compensates for sensor errors, offering reliable data. The development of a sensor node utilizing LoRaWAN and NFC protocols enhances real-time monitoring capabilities, providing a comprehensive solution for SHM systems.

Lastly, the attention will be focused on the importance of predictive maintenance to minimize train unavailability and reduce operational costs. By accurately capturing long-term dependencies in gradually changing data, the system predicts and forecasts failures in rolling stock equipment and in particular on the traction converter cooling system. The methodology, featuring data exploration, data pre-processing, and fault analysis, will be detailed.

Chapter 4 - Bluetooth Low-Energy Fingerprinting for the Implementation of PEPS System

Location tracking plays a pivotal role in both industrial and academic domains due to its diverse applications. While the Global Positioning System (GPS) has been a fundamental tool, it faces limitations, especially in indoor or challenging environments, necessitating the development of alternative technologies. Among these, *Bluetooth Low Energy* (BLE) has emerged as a promising medium-range wireless communication technology with the potential to address issues related to energy consumption, costs, bandwidth, and power usage. This technology has gained significant traction, particularly in Internet of Things (IoT) applications, with a focus on human-to-machine interaction.

4.1 State of Art

Several research efforts in the literature have leveraged BLE to implement indoor localization methods. For instance, in [87] researchers have proposed fingerprint-based indoor localization methods using techniques like Principle Component Analysis (PCA) or Autoencoder (AE) to extract fingerprint features. In [88], the BLE transmitter's position was estimated through a Deep Neural Network-based indoor localization by the signal received from several Anchor Points. To train and test the proposed Convolutional Neural Network (CNN) a large dataset was obtained by means of a simulated environment. Additionally, simultaneous indoor pedestrian localization and house mapping have been explored by combining data from Inertial Measurement Units and Bluetooth Low-Energy beacons placed indoors [89]. Real-time location and guidance applications have also been developed, utilizing BLE signals and Building Information Modeling (BIM) data.

In [90], a system that locates and guides a user inside a building in real-time is presented. This smartphone application captures the Bluetooth Low-Energy signal from the beacons and displays the location of the user's smartphone on a map that is obtained from Building Information Modeling (BIM), guiding the user to the desired destination.

In [91], BLE protocol is used to define the position of a user and multi-users in indoor environments; as the first scenario, the authors propose a localization server, client and user application based on a trilateration and Center of Gravity (COG) calculation; a second research element was an algorithm to improve the localization performance by means of a range-average algorithm exploiting the inertial sensors.

In the automotive field, human-to-machine interaction is critical, particularly in Passive Entry Passive Start (PEPS) systems. These systems often rely on *RF ranging* algorithms, which estimate distances based on signal strength. The estimation of distance in radio wave propagation relies on the principle that radio waves follow the inverse-square law [92]. This law stipulates that the strength of a signal decreases proportionally to the square of the distance from the source. Therefore, distance estimation can be inferred from the transmitted and received signal strengths, assuming there are no other factors introducing errors into the calculation. However, in indoor environments, the accuracy of distance estimation is significantly affected by the presence of signal interference. This interference results from various phenomena, such as signal reflection and absorption, which are characteristic of indoor structures [93]. These factors cause signal strength to fluctuate and become highly unreliable for distance calculations. Consequently, indoor localization algorithms must contend with these sources of noise to provide accurate position estimates.

In [94], the advantages of adopting Bluetooth Low Energy (BLE) over Wi-Fi are emphasized within an indoor application. This emphasis arises from the critical relationship between *Received Signal Strength Indicator* (RSSI) measurements and distance, a key factor in evaluating the positions of nodes. Indeed, the distance between transmitting and receiving nodes significantly impacts the strength of the RSSI signal. To address this challenge, various radio frequency-based positioning algorithms have been explored, including:

- **Time of Arrival (ToA)**: ToA calculates the distance between the transmitter and the receiver by considering the time taken for the signal to travel between them. It relies on knowing the speed of signal propagation in the medium and measuring the time it takes for the signal to travel from one point to another (often referred to as *Time of Flight* or *ToF*);

- **Time Difference of Arrival (TDoA)**: similar to ToA, TDoA calculates distance based on the time it takes for a signal to reach the receiver. However, TDoA relies on the difference in time of flight between multiple receivers to estimate the distance to a reference node with known coordinates;
- **Angle of Arrival (AoA)**: AoA determines the position of a mobile device by measuring the angle at which the signal reaches two sensors with known coordinates. Using triangulation techniques, this information is then used to calculate the coordinates of the transmitter's location, which is where the signal intersected the two directions.

Another approach to localization is RF Fingerprinting [95]. This technique leverages existing access points within an environment to determine the position of a device by matching observed signal patterns to a database of pre-recorded fingerprints.

In [96], BLE is introduced for the purpose of creating PEPS system. The primary focus of this work is on reducing the power consumption of BLE, rather than optimizing localization accuracy. In contrast, [97] proposes an adaptive BLE-based PEPS system. This system employs six BLE beacons for localization and nine additional BLE scanners for environment prediction. Data collected from these devices is consolidated through a smartphone acting as a concentrator.

In general, other indoor localization techniques are based on *Ultra-WideBand* (UWB) technology, which is typically used in complex, multi-environment scenarios. UWB operates at higher frequencies than BLE but consumes more power. For example, [98] achieved a remarkable 95% accuracy in identifying rooms within indoor environments using UWB. However, this approach required a significant infrastructure of sixteen anchors and distances to predefined landmarks, which served as input parameters for a neural network.

The solution that will be described it will focus on enhancing the accuracy of driver localization within a vehicle. It utilizes BLE to establish a connection between the driver (via a smartphone) and the vehicle, effectively creating a PEPS system. This connection is facilitated by six ESP32s, 32-bit micro-controllers equipped with integrated antennae, strategically positioned within the passenger compartment. These ESP32s function as BLE scanners and are arranged according to a network topology known as a *Y* network, which has been specifically designed and tested to improve the overall performance of the localization method. In contrast, the driver's smartphone acts as a BLE advertiser. One of the six ESP32s is responsible for classifying the smartphone's location using the k-Nearest Neighbor (k-NN) classifier [99]. The BLE Fingerprinting positioning technique relies on RSSI [99] acquisition, which is subsequently refined using a Kalman Filter to further enhance the accuracy of fingerprinting and classifier performance [100]. Particular attention is given to optimizing the spatial orientation of each BLE scanner to maximize the received signal strength (RSSI).

4.2 Proposed Method

In this section, we will present the solution employed for the implementation of the Position Entry and Position Start (PEPS) system, as illustrated in Figure 31. Initially, it will be described the hardware specifications of the chosen microcontroller. Subsequently, it will be outlined the methodologies and techniques applied to address the challenges that have been highlighted in existing literature.

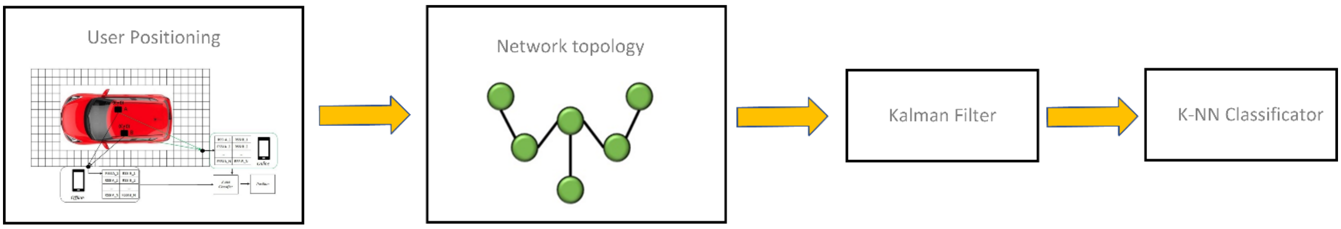

Figure 31. Proposed architecture for the implementation of a PEPS system.

Given the inherent limitations of GPS in scenarios involving enclosed environments or structures, the selection of suitable alternatives becomes crucial. Two prominent options that have been considered are Wi-Fi and Bluetooth Low Energy (BLE). Prior research has shed light on the drawbacks of each technology:

- *Wi-Fi Limitations*: Wi-Fi localization is often hindered by its reliance on routers. It necessitates the presence of Wi-Fi routers in the environment, which may not always be feasible or practical. Furthermore, signal attenuation occurs as the user moves farther away from the router, affecting the accuracy of localization.

- *BLE Advantages*: In contrast, BLE offers distinct advantages. The establishment of a BLE connection relies primarily on the distance between the reference point and the user, regardless of the specific environment. This attribute makes BLE a promising choice for overcoming localization challenges in a variety of scenarios.

In the next sections it will be explored how these considerations have influenced the approach to implementing the PEPS system.

4.2.1 Positioning Algorithm

Indoor positioning presents a host of challenges due to the particulars of indoor environments. These challenges include the multipath effect [101], signal attenuation, and dispersion caused by obstacles, as well as the issue of *Non-Line of Sight* (NLoS) signal transmission. To address these challenges, various ranging methods are employed to determine the location of a transmitter relative to a set of known reference points. These methods vary in terms of accuracy, hardware requirements, and operational logic.

To calculate the emitter's coordinates, information such as the time elapsed between signal emission and reception, and the direction from which the signal originates can be utilized. One common technique for obtaining distance information is RSSI, which relies on the relationship between signal attenuation and the distance it travels. Achieving accurate localization necessitates a prior analysis of the environment to gather reference data, which will be compared with real-time data during position detection. The Fingerprinting technique is often applied for this purpose.

Once distance information is acquired through ranging methods, it is essential to process this data to convert distances, time measurements, and signal strength into coordinates and, consequently, determine the precise position. The Fingerprinting technique is commonly employed for position determination, typically using RSSI measurements as input. This technique involves detecting BLE signals within a defined area to create a "Fingerprint" that can be used for localization by one or more

devices. The position is then determined using a cluster-matching algorithm. This algorithm entails identifying, among all the previously recorded detections, the one that best matches the real-time detection made by the device.
The adopted Fingerprinting algorithm [99] typically involves two distinct phases (Figure 32):

1. *Offline Phase*: during this phase, the environment is systematically analyzed using a grid of reference points. Groups of RSSI values are associated with each reference point, effectively creating a database of potential signal patterns associated with specific positions;
2. *Online Phase*: in this phase, the real-time RSSI values acquired by the device are compared with the groups of RSSI values established in the offline phase. This comparison leads to the determination of the most accurate and reliable position for the device at runtime.

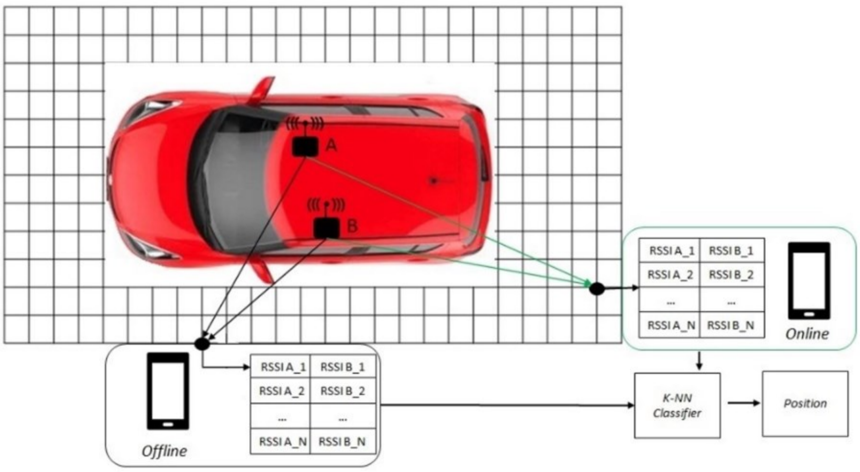

Figure 32. Localization system using BLE Fingerprinting.

While this Fingerprinting approach demands more time for implementation and incurs a higher computational cost, it has demonstrated its ability to deliver exceptional localization accuracy, making it a preferred choice in many indoor positioning scenarios.

4.2.2 Filtering Algorithms

Due to the aforementioned effects, the RSSI values demonstrate casual and unstable behavior, resulting in noise even when both the reference and target remain stationary. To mitigate these uncertainties, various filtering algorithms were considered for both pre-processing and post-processing stages:

- *Moving Average Filter (MA)*[102]: this filter involves collecting 'n' RSSI samples and computing their average to obtain a smoothed value.
- *Median Filter*: this filter calculates the median of 'n' RSSI samples by dividing the ordered sequence into two equal-length subsequences. One subsequence contains values lower than the median, while the other contains values higher than the median. This filter is effective in eliminating outliers in the measured data.
- *Kalman Filter (KF)*: the Kalman Filter employs a prediction and correction approach. In the prediction phase, it provides an a priori estimate of the state vector based on the previous step. The estimate is then refined in the update phase using measurements, resulting in a posteriori estimate for the next cycle.

Among these filtering methods, the Kalman Filter demonstrated the best performance. The operational steps of the Kalman Filter can be described using the following expressions:

Prediction:

- *Prediction of the current state*:

$$x_k = A \times x_{k-1} \tag{2}$$

- *Prediction of the covariance of the error*:

$$P_k = A \times P_{k-1} \times A^T + Q \tag{3}$$

Update:

- *Calculation of the Kalman gain*:

$$K = P_k \times H^T \times (H \times P_k \times H^T + R)^{-1} \tag{4}$$

- *Calculation of the new state*:

$$x_k = x_{k-1} + K \times (Z_k - H^T \times x_{k-1}) \tag{5}$$

- *Calculation of the new covariance of the error*:

$$P_k = P_{k-1} - (K_k \times H \times P_k) \tag{6}$$

In these equations:

- x_k: Estimate of the current state.
- A: State transition matrix.
- P_k: Average error estimate for the current state.
- Q: Estimated covariance of process errors.
- K: Kalman gain.
- H: Observation matrix.
- R: Estimated covariance of the measurement error.
- Z_k: Measurement vector for the current state.

For the proposed meyhod, the identity matrix was chosen for both matrices H and A. Additionally, Z_k corresponds to the *k-th* sample of the measured RSSI signal. These settings were selected due to the limited dynamic range of the parameter being observed.

4.2.3 Classification: K-NN

The *k-Nearest Neighbor* (k-NN) algorithm classifies an unknown sample by considering the class of the k nearest samples from the training set. To construct a classifier based on the k-NN approach, it is essential to compute the distances between the sample to be classified and all the training samples. This allows us to identify the k closest training samples along with their corresponding labels. Subsequently, the algorithm evaluates the labels of these k nearest points in relation to our sample. The destination class assigned to the new sample is determined by the label with the highest frequency among these k nearest points. This classifier is particularly well-suited for the BLE Fingerprinting technique, where online phase samples are compared in likelihood with the training samples, represented by the radio map of points obtained during the offline phase.

This method offers several key advantages. Firstly, it does not necessitate the process of learning or constructing a model, making it adaptable with arbitrary decision boundaries and resulting in a highly flexible model representation. Furthermore, it ensures the potential for expanding the training set, enhancing its adaptability and accuracy.

4.2.4 Network Topology

The exploration of network topologies involves defining the spatial arrangement of all nodes within the network and their interconnections, encompassing both physical and logical links. Employing principles from graph theory, critical parameters such as node count, transmission channels, and redundancy are considered, all while maintaining fault tolerance [103]. In the chase of accurately determining the smartphone's location concerning various vehicle zones, various network topologies were experimented with.

Specifically, attention was directed towards star and tree networks; however, the outcomes from these investigations proved to be highly unreliable and failed to distinguish among most of the distinct vehicle zones. To improve performance, the decision was made to implement a hybrid network known as the Ψ network (Figure 33). This network retains the same structural layout as the tree network but functions akin to the star network, with the top central node serving as the hub responsible for receiving, acquiring, and processing data. The adoption of this hybrid network affords a notably dependable means of pinpointing the smartphone's location relative to the diverse vehicle zones.

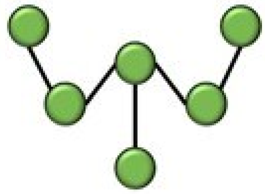

Figure 33. Ψ network topology.

4.3 Results

As mentioned previously, the Kalman Filter served as the chosen algorithm for enhancing RSSI estimations, while Fingerprinting was employed as the method for determining the driver's precise location. The execution and evaluation of the proposed approach involved a series of five key stages:

1. *Spatial Orientation of ESP32*: initially, an investigation was conducted to determine the most effective ESP32 spatial configuration that would best distinguish the smartphone's location [104].
2. *System Implementation*: the complete system was built, involving six ESP32 devices responsible for monitoring both the external and internal positions of the smartphone. This was done to generate and store a comprehensive radio map of reference points.
3. *Real-time Smartphone Position Acquisition*: the system continuously acquired and categorized the real-time position of the smartphone.
4. *Data Processing*: the data gathered during the third phase were subjected to statistical analysis, including techniques such as ANOVA (Analysis of Variance) and the Siegel–Tukey Test.
5. *Classifier Accuracy Evaluation*: the accuracy of the classifier was assessed using the Classification Learner application within the Matlab environment. This evaluation involved training, validating, and testing the classifier on the collected data.

These five steps constituted the core components of the method's implementation and assessment.

4.3.1 ESP32 Microcontroller

The ESP32 microcontroller, developed by Espressif Systems [83], is equipped with a built-in antenna that supports both Wi-Fi and Bluetooth operations at the 2.4 GHz frequency. It boasts 48 GPIO pins and is categorized as a cost-effective device. This microcontroller is capable of implementing various protocols including TCP/IP, MAC WLAN, Wi-Fi, and Bluetooth. Additionally, it provides interfaces like UART, SPI, I2C, I2S, and Capacitive Touch.

The ESP32 is highly regarded for its exceptional performance, durability, and versatility, making it an excellent choice for a wide array of applications, including wearables and the Internet of Things (IoT). Its dynamic power scaling feature, influenced by the low duty cycle, allows for the minimization of energy consumption while maintaining a balanced trade-off between communication range and data transfer speed.

One notable feature of the ESP32 is its state-of-the-art digital calibration, which enables it to deliver an average power of +20.5 dBm.

In the proposed hardware system, which comprises six ESP32 microcontrollers, an important advantage is realized. This system surpasses the inherent limitations of beacons, which are typically restricted to functioning solely in Advertiser mode without the capability for low energy consumption and data processing.

4.3.2 ESP32 Orientations

The initial step in the process involves determining the most suitable orientation for the ESP32. This was accomplished through two separate measurement campaigns designed to assess whether it would be more advantageous to configure the ESP32 as a scanner and the smartphone as an advertiser, or vice versa.

Furthermore, during these campaigns, the ESP32 was rotated along its z- and y-axes (as shown in Figure 34

Both campaigns were conducted under the following sub-configurations:

1. ESP32 positioned inside the vehicle on the driver's side, with the smartphone placed either externally in four positions (i.e., driver's side or left - *LoS*,

passenger side or right - *NLoS*, front side - *NLoS*, and backside - *NLoS*), or internally in two positions (both *NLoS*), specifically, the driver's seat and the passenger's seat (as illustrated in Figure 35a).

2. ESP32 located inside the vehicle on the driver's side, with the smartphone positioned internally in two positions (both *NLoS*), namely, the driver's seat and the passenger's seat (as depicted in Figure 35b).

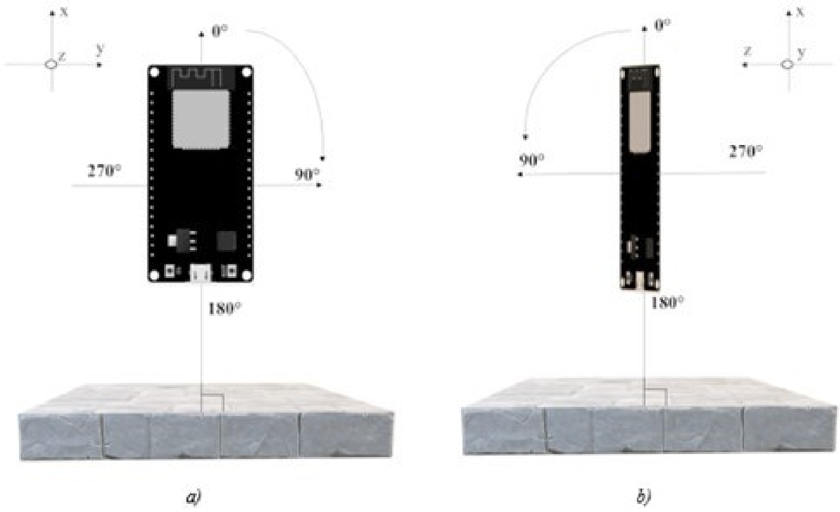

*Figure 34. ESP32 orientation: (**a**) Rotation with respect to the z-axis. (**b**) Rotation with respect to the y-axis.*

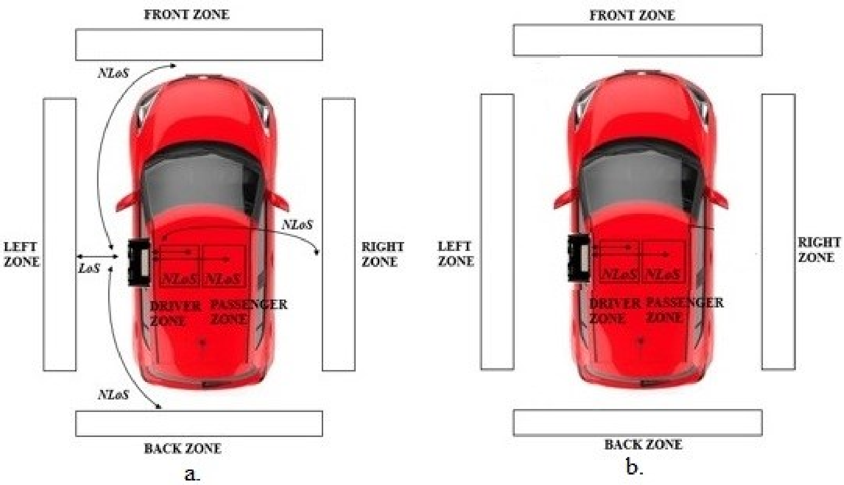

Figure 35. LoS and NLoS for different zones: (a) Configuration 1. (b) Configuration 2.

In both scenarios, the RSSI values obtained were subjected to processing and filtering using a Kalman Filter, which effectively reduces noise in RSSI measurements. To determine the optimal ESP32 orientation, a loss function was assessed. This loss function aimed to establish a connection between the average and standard deviation of RSSI value distributions and to identify the maximum separation between distribution centers with small standard deviations. Here's how it was calculated:

$$f_{loss} = \frac{\mu_{sx} - \mu_{dx} - \mu_{ant} - \mu_{pos}}{\sqrt{\sigma_{sx}^2 + \sigma_{dx}^2 + \sigma_{ant}^2 + \sigma_{pos}^2}} \tag{7}$$

$$f_{loss} = \frac{\mu_{drv} - \mu_{pass}}{\sqrt{\sigma_{drv}^2 + \sigma_{pass}^2}} \tag{8}$$

where:

- μ_{sx}, μ_{dx}, μ_{ant}, μ_{pos}, μ_{drv}, μ_{pass} (dB): these represent the average values of RSSI for different zones, calculated from the respective arrays of RSSI values.
- σ_{sx}, σ_{dx}, σ_{ant}, σ_{pos}, σ_{drv}, σ_{pass} (dB): these denote the standard deviations of RSSI values in different zones, calculated from the respective arrays of RSSI values.

The most favorable outcomes were associated with configuration 1, specifically, the orientation at 180°–90°. This orientation exhibited a significant loss function value and proved to be more manageable in terms of software implementation and overall system realization. Although some orientations in Table 3 had loss function values greater than the chosen orientation, they were characterized by unfavorable features such as non-Gaussian data distribution, overlapping averages in different zones, and high standard deviations, which did not meet the selection criteria.

Table 3. Loss function results for ESP32 orientation referring to the two different configurations evaluated as scanner and smartphone as advertiser.

	Configuration 1		Configuration 2	
Orientation	**Raw Values**	**Smoothed Values**	**Raw Values**	**Smoothed Values**
0°- 0°	13,0633	26,1039	1,0604	2,9444
0° - 90°	12,5879	23,8130	0,0562	-0,1474
0° - 180°	12,4053	22,6049	1,1373	1,2806
0° - 270°	11,7701	17,4743	-0,2721	-2,1425
90° - 0°	8,9414	16,4160	0,2833	0,2847

90° - 90°	10,4545	17,5767	0,6223	1,5775
90° - 180°	13,5501	23,3651	-0,8943	-1,0363
90° - 270°	10,7310	19,9310	0,5055	3,4045
180° - 0°	11,7475	32,4822	0,8637	1,3109
180° - 90°	12,2626	27,5023	0,1383	0,2263
180° - 180°	14,7112	27,5250	1,2878	4,2162
180° - 270°	13,8268	25,4591	0,7454	2,3117
270° - 0°	9,6949	18,2563	-0,0980	-0,3246
270° - 90°	12,6398	22,4502	0,5281	0,7525
270° - 180°	12,5429	20,6201	-0,2232	-1,7390
270° - 270°	11,9059	19,7627	0,2115	1,8816

4.3.3 System and Radio Map Realization

After the ESP32's orientation was established, the PEPS-BLE system was evaluated for its localization performance. This evaluation was conducted using a Suzuki Swift as the test vehicle and a Huawei P10 Lite smartphone simulating the smart key. The test environment, including both the vehicle and its surroundings, measured 4.0 meters by 6.0 meters.

For the offline phase of the BLE-Fingerprinting model, a radio map was meticulously constructed. This radio map consisted of 90 reference points, with a 50-centimeter spacing for external areas and a 15-centimeter spacing for internal areas. The coordinates of the test environment were categorized into six distinct areas:

1. *Left area*
2. *Front area*
3. *Right area*
4. *Rear area*
5. *Driver's area*
6. *Passenger's area*

Each of these areas was subdivided into fifteen points, marked at the intersections of the rectangle sides, as illustrated in Figure 36.

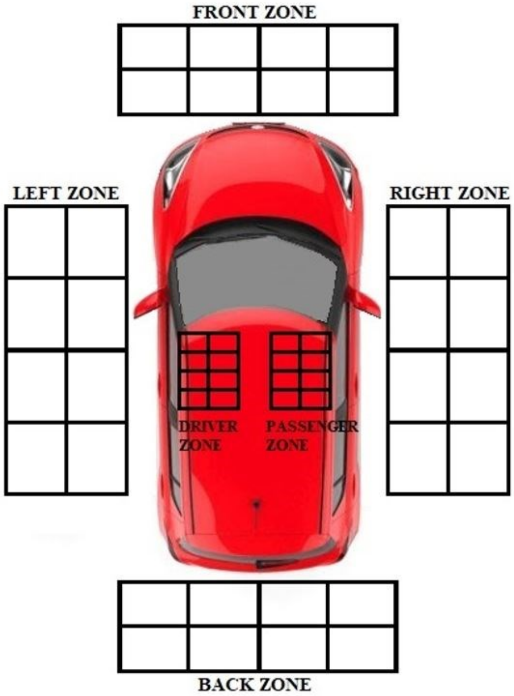

Figure 36. Radio Map

Once the radio map has been established, the entire system was assembled in accordance with the layout determined by the selected network topology (as depicted in Figure 37). During the offline phase, the RSSI values collected by each ESP32 were transmitted using the Universal Asynchronous Receiver-Transmitter (UART) protocol, as illustrated in Figure 38. In particular:

- *ESP32-E*, *ESP32-F*, and *ESP32-D* served as transmitters, sending their acquired data to *ESP32-A*, *ESP32-C*, and *ESP32-B*, respectively.
- *ESP32-A* and *ESP32-C* acted as receiver-transmitters, relaying the data received from the leaf nodes and simultaneously transmitting their own RSSI measurements to *ESP32-B*.
- *ESP32-B* operated as a concentrator, receiving and processing its own measured RSSI values along with those received from other nodes.

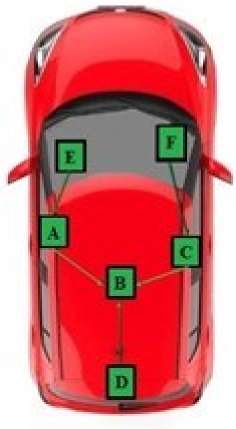

Figure 37. Layout of network topology with ESP32.

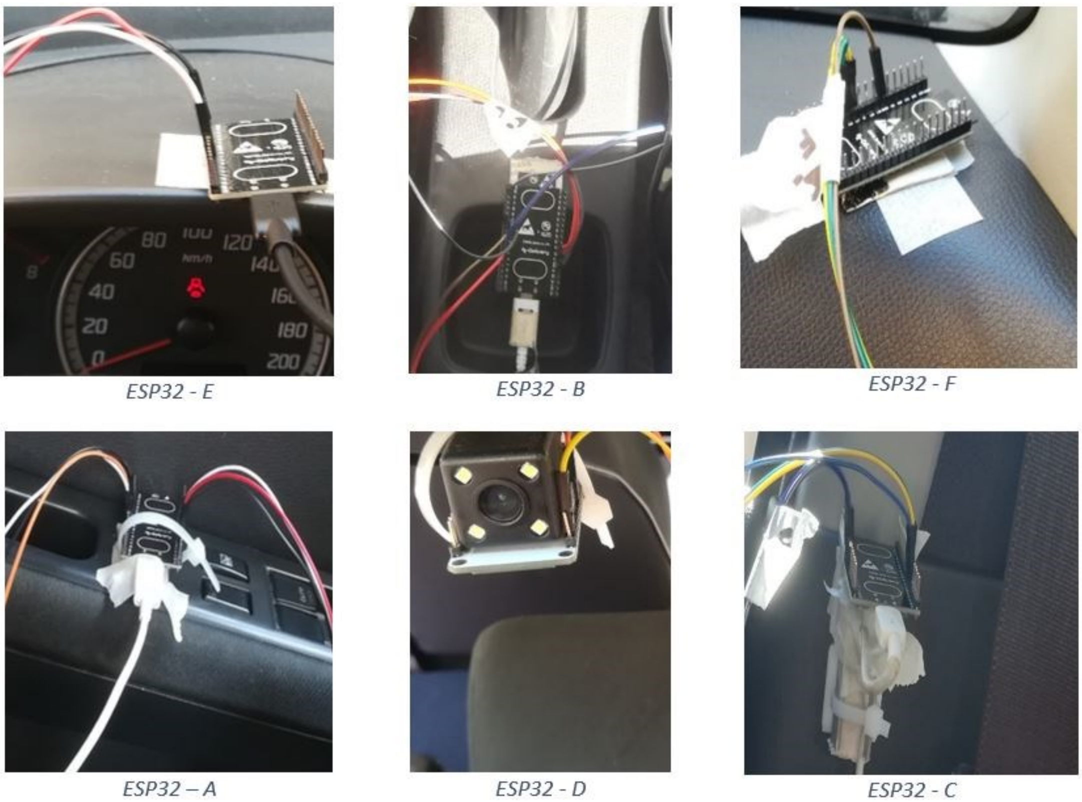

Figure 38. Definition of roles for every ESP32.

4.3.4 Offline and Online Data Acquisition

During the offline phase, numerous RSSI measurements were gathered and subjected to filtering for each distinct grid position as depicted in Figure 36. Specifically, 130 samples were collected at each grid point, with a sampling rate of 1 Hz. These collected

samples were subsequently averaged and organized into a 15x6 matrix, representing the mean RSSI values for each grid position within each zone.
These computed average values were then utilized in the training phase of the *k-NN* classifier. In the online phase, the data acquisition process for each zone occurred within a time interval ranging from 360 seconds to 420 seconds.

4.3.5 Statistical Inferences

The significance of the differences experienced in RSSI measures has been assessed by means of statistical analysis such as *One-Way ANOVA* and the *Siegel-Tukey Test*. In both analyses, the zones are associated as described in the following:

1. The Left zone;
2. The Front zone;
3. The Right zone;
4. The Rear zone;
5. The Driver zone;
6. The Passenger zone.

4.3.5.1 One-Way ANOVA

The outcomes of the ANOVA test are presented, showcasing results both for the radio map (depicted in Figure 39) and for the data derived from the classifier during the online phase (illustrated in Figure 40). The results are visually represented using box plots, where the rectangular box spans from the first quartile to the third quartile, divided by the median. The outer segments of the box correspond to the minimum and maximum values encountered within the dataset. This graphical representation effectively divides the data into four equally populated intervals corresponding to the quartiles.

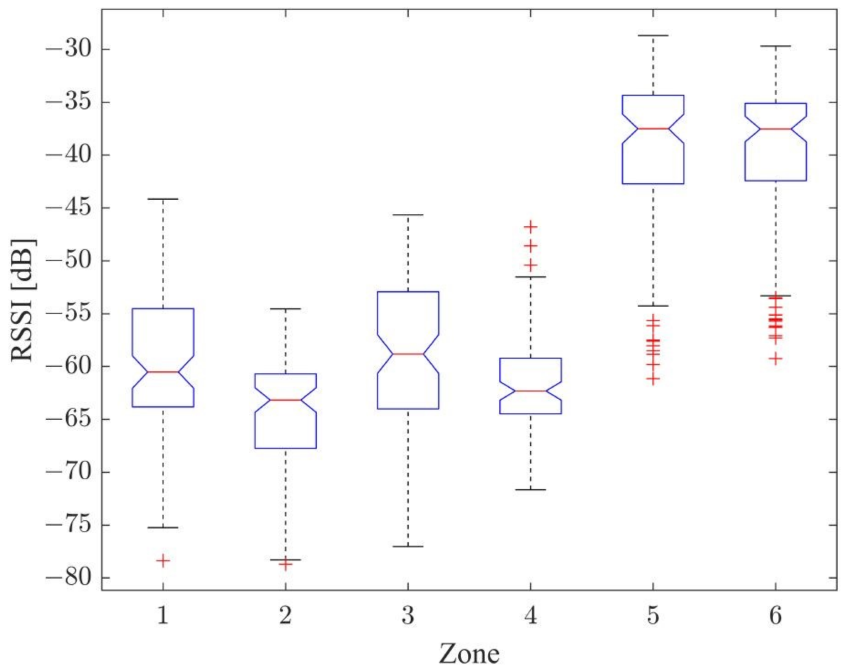

Figure 39. ANOVA Box Plot for Radio Map

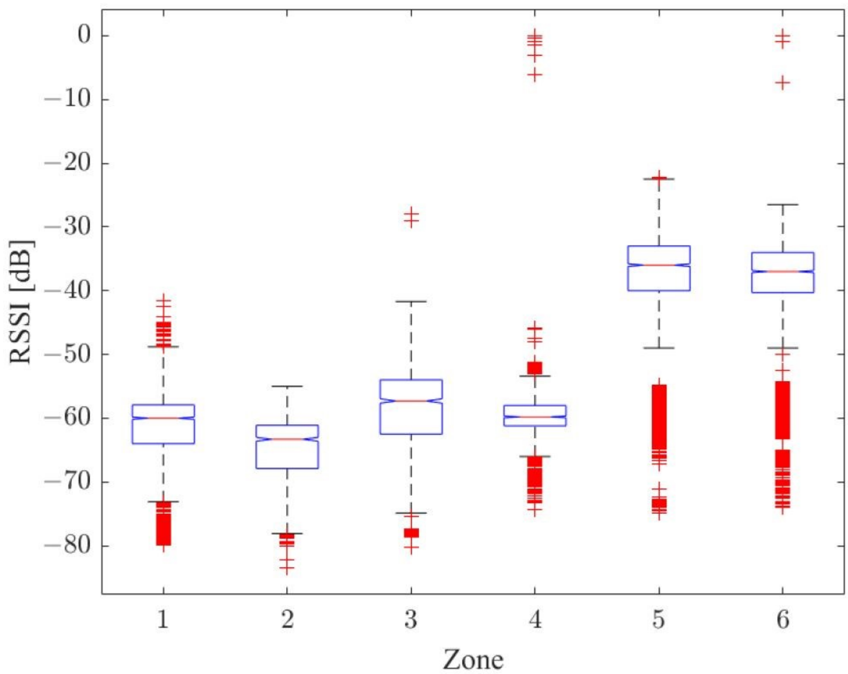

Figure 40. ANOVA Box Plot for classifier output

As evident from Figures 39 and 40, these box plots clearly demonstrate significant distinctions in the different positions of the driver, whether they are located inside or outside the vehicle.

4.3.5.2 Siegel-Tukey Test

After determining the significance of RSSI values through ANOVA, the Siegel-Tukey Test was used to determine the correlation of RSSI values in each zone where the ESP32s are positioned. To evaluate the classifier's performance, the Siegel-Tukey Test was utilized. The outcome of the Siegel-Tukey Test for the radio map, prior to processing, is showed in Figure 41. In this representation, certain zones, namely *Left*, *Right*, and *Rear*, exhibit overlapping regions, indicating that distinguishing between different positions was challenging.

However, after the filtering and classification process (as depicted in Figure 42), the Siegel-Tukey results clearly delineate the different zones, enabling the accurate identification of each specific zone.

The Tukey test for the radio map, both visually and statistically, illustrates that the group averages for internal and external zones are significantly different in terms of significance α (equal to 0.05). This highlights the system's capability to discern whether the smartphone is inside or outside the vehicle. Nevertheless, it is worth noting that the averages for the external and internal zones do not exhibit significant differences.

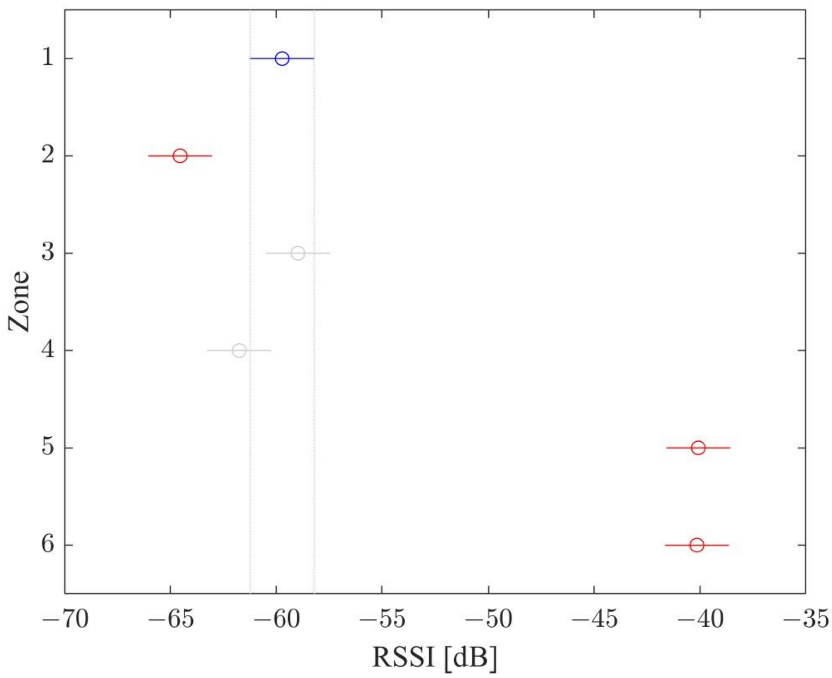

Figure 41. Siegel-Tukey Test for Radio Map.

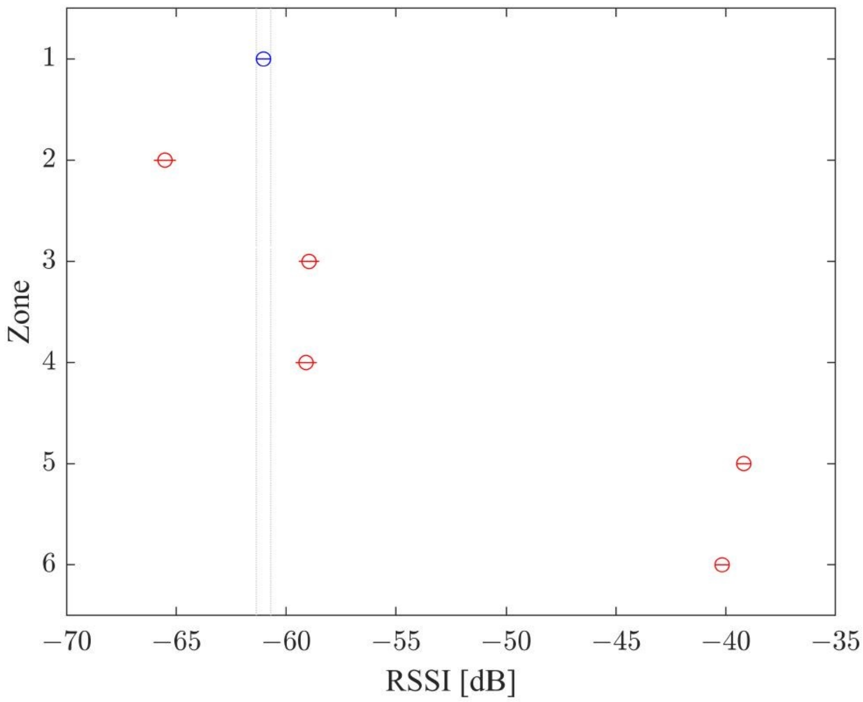

Figure 42. Siegel-Tukey Test for classifier output.

4.3.6 Classification Learner

The Classification Learner played a crucial role in training the models used for data classification. The dataset comprised columns representing values collected by the six ESP32s, the relative classification by ESP32-B (responsible for classifying), and the expected classifications related to their respective zones. This dataset, sized at 2208 rows by 8 columns, was imported and randomly reorganized to ensure unbiased data representation. It was then split into 70% for the training phase and 30% for the testing phase. The results revealed the following:

- The Scatter Plot (Figure 43) aided in assessing which features to include or exclude, visualizing training data, and identifying incorrectly classified points. The plot indicated some data dispersion, particularly in areas where occasional sample overlap led to challenges. Figure 43 demonstrated that the classifier achieved an accuracy of 98.7% in identifying RSSI values for each zone, with incorrect predictions occurring primarily between Zones 1 and 4.

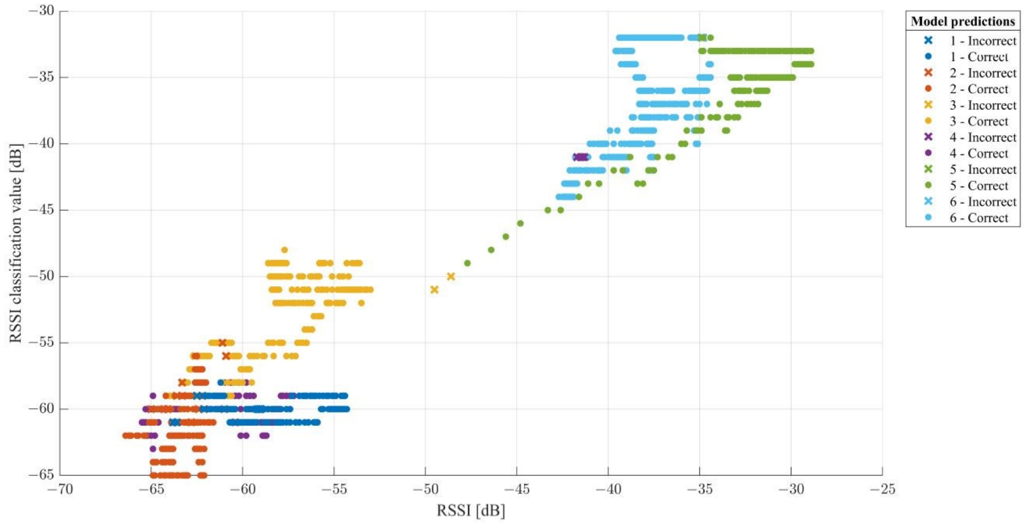

Figure 43. Dataset scatter plot

- The Confusion Matrix (Figure 44) pinpointed the areas where the classifier achieved accuracy. It helped calculate metrics like *Positive Predictive Value* (PPV), *False Discovery Rate* (FDR), *True Positive Rate* (TPR), and *False Negative Rate* (FNR), each of which assessed different aspects of classification performance (as shown in Figure 45 and Figure 46).

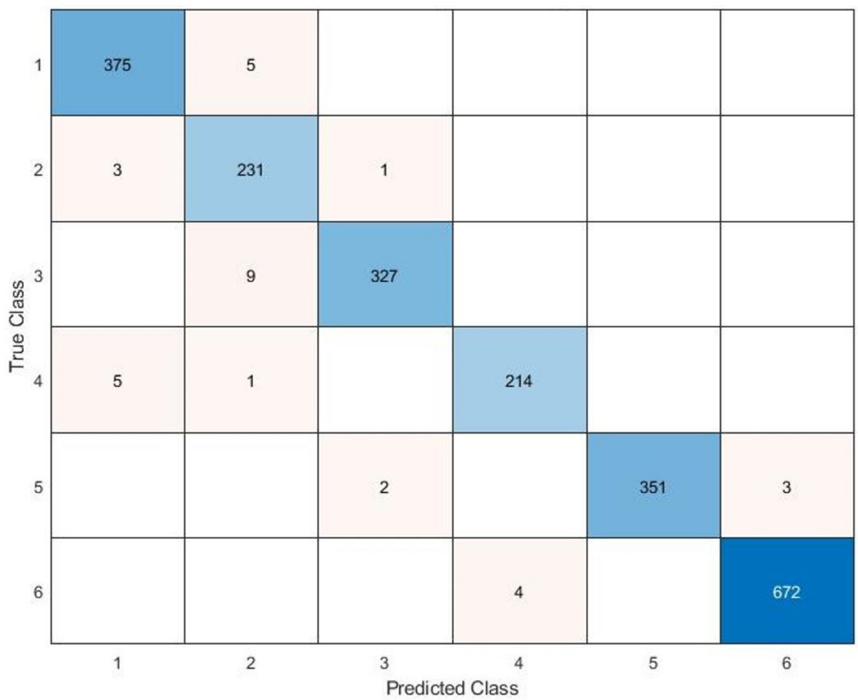

Figure 44. Confusion Matrix: Number of observations

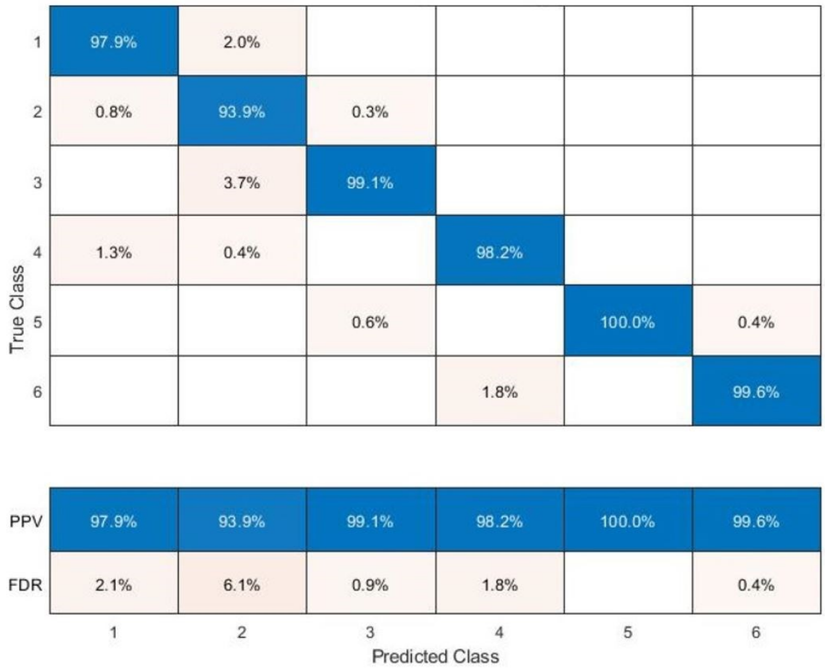

Figure 45. Confusion Matrix: Positive Predictive Values vs. False Discovery Rate

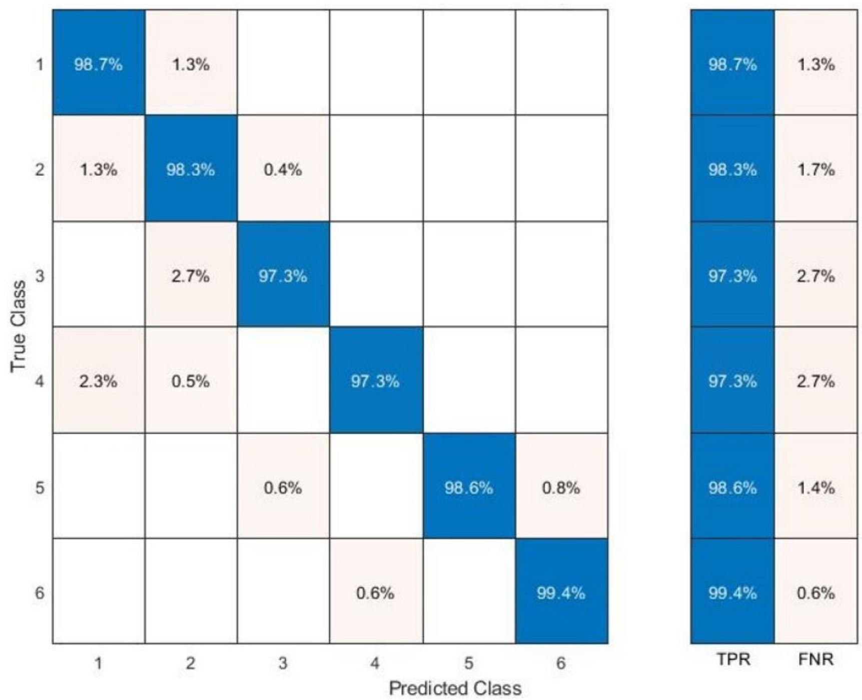

Figure 46. Confusion Matrix: True Positive Rate vs. False Negative Rate

Comparing true classes with predicted classes, it became evident that the predictive positive rates exceeded false negatives and false detection rates. This indicates that the adopted classifier method reliably identifies user positions in the different tested zones. To quantify the agreement between measured and true values, accuracy was evaluated according to [105]:

$$ACCURACY = \frac{TP + TN}{TP + TN + FP + FN} \tag{9}$$

Here, *TP* stands for true positives, *TN* for true negatives, *FP* for false positives, and *FN* for false negatives. The overall accuracy achieved by the proposed method, aided by filtering and the chosen network topology, reached 98.5%. This accuracy surpassed that of similar solutions presented in the literature [97].

Chapter 5 - Implementation of Smart Oscillation Monitoring System

Detecting the stress state of structures is a critical concern in structural engineering, offering essential insights into their well-being and the identification of damage development and propagation. *Structural Health Monitoring* (SHM), a field encompassing various techniques and technologies, has been developed to address this challenge and is extensively applied in aerospace and civil engineering [106]–[112].

In recent decades, the scope of SHM has expanded to encompass infrastructure and civil engineering, including historical and modern buildings, bridges, tunnels, industrial facilities, manufacturing plants, offshore platforms, port structures, foundations, and excavations [113]–[116].

Existing bridge structures are continually exposed to environmental and operational stresses throughout their lifespan, potentially accelerating structural deterioration. Additionally, unforeseen events like earthquakes can occur, underscoring the importance of promptly assessing a structure's condition to ensure safety. Although visual inspections have traditionally played a key role in detecting surface defects and assessing structural health, this method is labor-intensive, time-consuming, and subject to subjectivity. To mitigate these shortcomings, SHM techniques have been proposed and are increasingly applied to long-span bridges [117]–[119]. SHM is defined as the utilization of sensing techniques and structural feature analysis to identify structural damage or deterioration; it is recommended that SHM be considered within the framework of condition assessment and as a damage detection technique [120]. In essence, SHM primarily serves the objectives of damage detection and condition assessment.

SHM techniques have been employed in bridges for nearly four decades through the installation of *Structural Health Monitoring Systems* (SHMS) and have found increasing application in long-span bridges globally. In summary, SHM techniques, particularly those rooted in vibration measurements, hold immense potential in the monitoring and maintenance of bridges to ensure their safety and longevity [121]–[125].

5.1 State of Art

Among the myriad sensor techniques in SHM, the vibration-based approach utilizing accelerometers and data acquisition systems is one of the most extensively researched and applied methods. In this approach, the structure's response is measured under specific excitation, and its modal characteristics, including natural frequencies, damping ratios, mode shapes, and modal scaling factors, are determined [126]–[128]. The accelerometer's performance significantly impacts the data quality and result accuracy. Therefore, selecting an appropriate accelerometer must strike a balance between cost and overall SHM system performance [129], [130].

In recent years, the use of micro-electromechanical systems (MEMS) sensors in SHM systems has garnered significant attention. MEMS sensors are miniature devices capable of measuring a wide range of physical parameters, including acceleration, strain, pressure, and temperature, with remarkable precision and accuracy [131]. They are also compact, energy-efficient, and cost-effective, making them ideal for extensive, long-term structural monitoring. The integration of MEMS sensors into SHM systems brings several advantages, such as enhanced accuracy and reliability, reduced power consumption, and improved data acquisition and processing capabilities. MEMS sensors enable real-time monitoring of a structure's stress state, facilitating early detection of damage or deterioration and cost-effective maintenance and repair. Moreover, they can identify potential failure modes and predict the remaining useful life of the structure. In the context of bridges, MEMS sensors in SHM systems offer comprehensive, continuous monitoring capabilities capable of detecting even subtle changes in structural conditions due to external loads, traffic, or environmental factors [129]–[132]. This data aids in optimizing the bridge's performance, extending its service life, reducing maintenance and repair expenses, and ensuring user safety.

Overall, the incorporation of MEMS sensors into SHM systems holds great promise for monitoring and maintaining structures, particularly for large-scale, critical infrastructure such as bridges [133]. With ongoing advances in MEMS technology and data analytics, SHM systems are anticipated to become even more efficient, accurate, and cost-effective, offering greater benefits to both engineers and end-users.

Despite their numerous advantages, MEMS inertial sensors do have drawbacks that need consideration. Their small size renders them highly sensitive to environmental fluctuations, and random noise can complicate error compensation procedures and restrict their applicability [134], [135]. Notably, an increasing bias drift with non-linear characteristics is a significant concern, indicating that while MEMS Inertial Measurement Units (IMUs) can offer exceptional accuracy at high rates, angular velocity and acceleration data may degrade over extended periods. Consequently, particular attention is required when using these sensors, typically classified based on their bias instability and random walk parameters, both of which define their performance and suitability for specific applications [136], [137]. For instance, accelerometers with a bias instability below 0.01 mg are considered "*marine-grade*", while more economical "*consumer-grade*" sensors exhibit lower performance alongside reduced power consumption [138]–[140].

To address these MEMS limitations, various studies have explored the implementation of Kalman filters (KFs) for error compensation. Particularly in SHM applications, high-frequency noise can significantly affect accurate structural acceleration estimation. Therefore, the Kalman Filter algorithm can be employed to reduce noise in data obtained from MEMS accelerometers. It functions by estimating a system's state based on a series of noisy measurements. In the case of MEMS accelerometer data, the Kalman filter aids in estimating an object's true acceleration by filtering out high-frequency noise [141]–[144].

In the next sections, a redundant prototype of low-cost accelerometers utilizing a Kalman Filter algorithm for filtering purposes will be described. The performance of this solution is assessed through a comparison with a high-performance accelerometer sensor, utilizing a controlled oscillation generator specifically designed to produce oscillations with known frequency and amplitude. Then, a sensor node suitable for SHM applications will be presented.

5.2 Proposed Methods and Smart Monitoring Architecture

The assessment of a platform centered around the Internet of Things (IoT) and utilizing redundant low-cost MEMS accelerometers for monitoring extensive structures like bridges and tunnels has been conducted. The redundant prototype for this platform was previously introduced in [145]. The research efforts have primarily concentrated on two principal aspects:

- Evaluation of a redundant prototype of low-cost MEMS accelerometers for measuring oscillations, employing the Kalman filter for data refinement. The performance assessment involved the use of a customized testing setup designed for controlled oscillation measurements, along with a comparative analysis against a high-performance accelerometer sensor, serving as a reference system.
- Development of an IoT solution for a real-time system responsible for data acquisition and visualization. This system is based on the adoption of the redundant prototype and follows the standard IoT protocols.

5.2.1 Proposed Method

As for the first objective, the primary aim was to exploit a redundant configuration of accelerometers to mitigate the inherent errors associated with low-cost MEMS accelerometer sensors. These errors encompass factors such as bias instability, in-run bias instability, and velocity random walk. By leveraging the redundancy inherent in the prototype, it became feasible to employ it for precise oscillation measurements. To achieve this goal, it has been introduced an initialization procedure founded on the utilization of a *Zero-Velocity Update* (ZVU) filter. This filter facilitates the estimation of initial error values and initial alignment parameters. Consequently, the acceleration measurements can be effectively compensated for the estimated noise values. Subsequently, these compensated measurements undergo processing through a Kalman Filter, serving as a mechanism for high-frequency noise reduction. Finally, a *Fast Fourier Transform* (FFT) is applied to determine the oscillation frequency and amplitude, as illustrated in Figure 47.

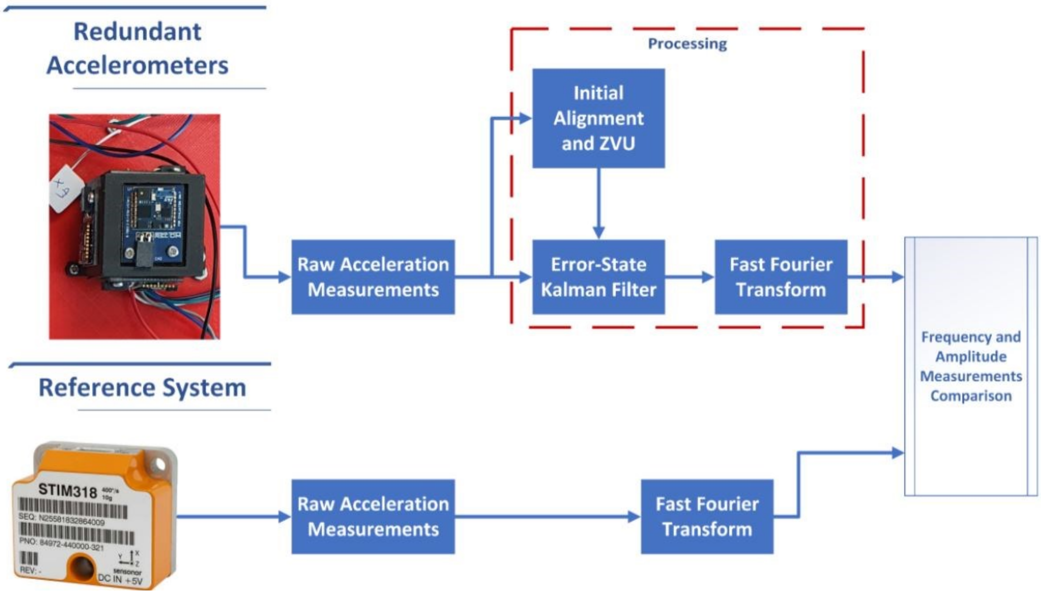

Figure 47. Proposed method based on the adoption of a Zero Velocity Update filter.

The validation of the proposed methodology's performance is conducted through a meticulously controlled oscillation generator, based on a crank-rod system capable of emulating a spectrum of oscillation frequencies. Furthermore, for the purpose of assessment and performance comparison, a marine-grade MEMS sensor has been incorporated as a reference system.

5.2.1.1 Zero-Velocity Update filter and initial alignment

The Kalman filter stands as a recursive algorithm designed to estimate the state of a dynamic system, leveraging a series of noisy measurements. Its operation involves two fundamental steps: prediction and update. In the prediction phase, the algorithm forecasts the state of the system at the subsequent time step, drawing upon a model describing the system's dynamics. Subsequently, this prediction is refined in the update step, incorporating actual measurements. Notably, the Kalman filter encompasses the adjustment of both the state estimate and the error covariance matrix based on these measurements and the measurement noise covariance matrix [137].

The Zero-Velocity Update (ZVU) filter builds upon the principles of an *Error-State Kalman Filter* (ESKF). Its methodology is based on the assumption that the system is in a stationary state, specifically, with a velocity of zero. The ZVU filter implementation unfolds through the following key steps:

1. The position vector is derived from a *Global Navigation Satellite System* (GNSS) source.
2. The velocity vector is initialized to zero, aligning with the stationary assumption.
3. Roll and pitch angles are computed via a coarse leveling procedure, as expressed in equations (10) and (11):

$$\theta = \arctan\left(\frac{-f_{ib\,x}^{b}}{\sqrt{(f_{ib\,y}^{b})^2 + (f_{ib\,z}^{b})^2}}\right) \tag{10}$$

$$\phi = arctan2\left(-f_{ib\,y}^{b}, -f_{ib\,z}^{b}\right) \tag{11}$$

where θ represents the pitch angle, Φ denotes the roll angle, and f_{ib}^{b} signifies the raw acceleration measurements along the *x*, *y*, and *z* axes, as referenced to the body frame. The predict/correct phases follow the ESKF implementation [145]. This approach entails the estimation of noise terms during the correction of the state vector and their subsequent utilization in the subsequent prediction phases. The residual error values obtained are then applied to refine the acceleration measurements, leading to enhanced accuracy in oscillation frequency and amplitude measurements.
For the sake of clarity, in this particular application, the GNSS position is evaluated only once. This is due to the accelerometers' installation on a structure where GNSS position variations are either insignificant or unobservable by most GNSS modules. Nevertheless, knowledge of the position remains crucial to effectively compensate for the gravity vector.

5.2.1.2 Kalman Filter approach

Once the initial noise parameters have been acquired through the application of the ZVU filter, a subsequent Kalman Filter is employed to further refine the acquired

acceleration samples, with the primary objective of filtering out high-frequency noise. To optimize computational efficiency, the update matrix is simplified to the identity matrix. This means that, in the prediction stage, the so-called a-priori estimated value (denoted as $\hat{x}^{-}$) is equal to the corrected value obtained in the previous iteration.
The correction stage is executed according to the following equations:

$$K = P/(P + R) \tag{12}$$

$$\hat{x}^{+} = \hat{x}^{-} + K(x - \hat{x}^{-}) \tag{13}$$

$$P = (I - K)P + (\hat{x}^{+} - \hat{x}^{-})Q \tag{14}$$

where:

- K represents the Kalman gain.
- P signifies the error covariance matrix.
- R stands for the noise covariance matrix.
- $\hat{x}$ and $\hat{x}^{-}$ refer to the state vector and the estimated state vector, respectively, which in this context represent the acceleration measurements.
- I denotes the identity matrix.
- Q is the system noise covariance matrix.

5.2.1.3 Controlled oscillation system and measurement setup

The measurement setup comprises a controlled stepper motor mechanism responsible for the rotation of a cylinder, which is connected to the beam through a linkage system designed to convert the stepper motor's rotary motion into linear motion. Sensor modules are strategically positioned on a plate that is rigidly secured to the beam. This setup allows for the creation of harmonic motion. The nominal acceleration values ($\alpha(t)$) can be determined from the maximum prescribed displacement and frequency using the following equation:

$$\alpha(t) = -\omega^2 A sin(\omega t) \tag{15}$$

Here, A represents the vertical displacement amplitude, and $\omega = 2\pi f$ denotes the angular frequency.

The geometric dimensions of the constructed system are detailed in Table 4, which also highlights the maximum displacement, calculated as the difference between the highest and lowest points of the plate along the Z-Axis.

Table 4. Geometrical dimension of the controlled oscillating system

System	Dimension (cm)
Beam	22.5 × 1 × 1 (L × W × H)
Linkage	9.5 × 0.2 × 0.5 (L × W × H)
Cylinder radius	5,5
Max displacement	0,5

Figure 48 visually portrays the controlled oscillation generator and the measurement setup. Notably, the mechanical components, depicted in black color, are fabricated using the 3D printing process [146], [147], while the stepper motor and motor driver are highlighted in orange. The measurement setup primarily consists of sensor modules, including the proposed redundant low-cost accelerometers (in red), alongside the STIM318 by SensoNor^{TM}, a marine-grade accelerometer (in green) employed as a comparative reference. Both modules are interfaced with a microcontroller, specifically the STM32F446RE from STMicroelectronics^{TM}, positioned under the plate. It acquires data via the I2C (Inter Integrated Circuit) and RS422 protocols, respectively. To enable seamless communication between the RS422 and UART protocols, an interface utilizing dual differential drivers and receivers (SN75C1167 from Texas Instruments) was used. For synchronization purposes, the microcontroller triggers the marine-grade accelerometer data sampling. The STIM318 samples data at a rate of 2 kHz and is triggered at 125 Hz, resulting in an average delay of 250 μs between the request and the sampling of measured parameters. Ultimately, the acquired data is transmitted to a personal computer via a Bluetooth module connected to the microcontroller through the UART interface for subsequent processing.

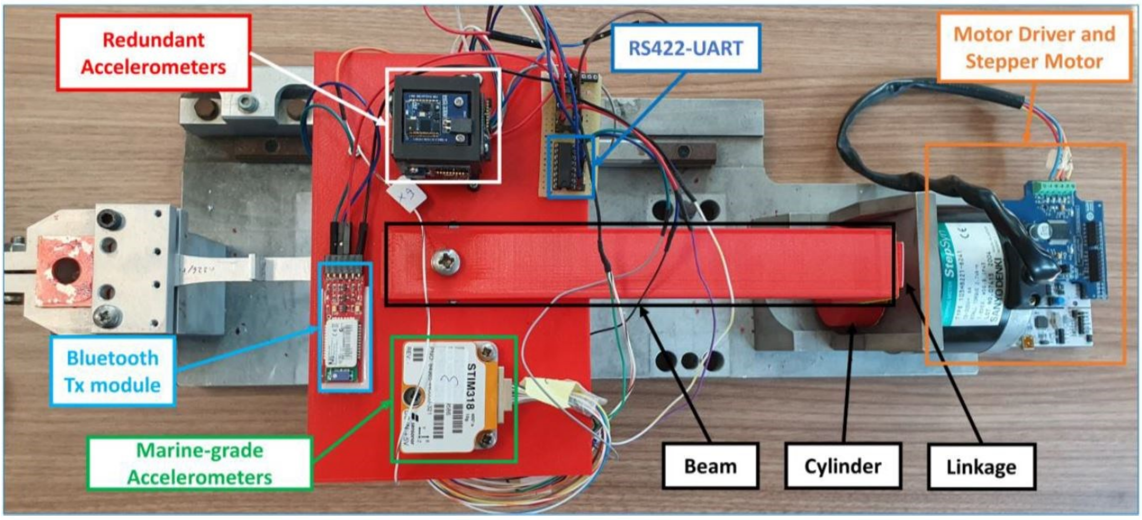

Figure 48. Realized oscillating system and measurement setup for performance assessment; thanks to the stepper motor oscillations with known frequency and amplitude can be applied to the low-cost redundant accelerometers

5.2.2 Proposed Smart Monitoring Architecture

Regarding the second aspect, the prototype device is equipped with an integrated wireless communication system that operates on the *LoRaWAN* protocol, as well as a *Near Field Communication* (NFC) module designed for remote and in-situ monitoring, as depicted in Figure 49. After performing the necessary computations to determine the quantities of interest locally, the microcontroller employs the *LoRaWAN* protocol to transmit the results. These results are transmitted to a gateway equipped with a node-red-flow, which subsequently relays the measured data via *MQTT* to a cloud-based dashboard established on the *Thingsboard* platform. Furthermore, the acquired data can also be accessed through the NFC protocol. Specifically, by using a mobile phone as an NFC reader, the node's identity is detected and employed to access the IoT platform, enabling the display of measured data on the mobile application.

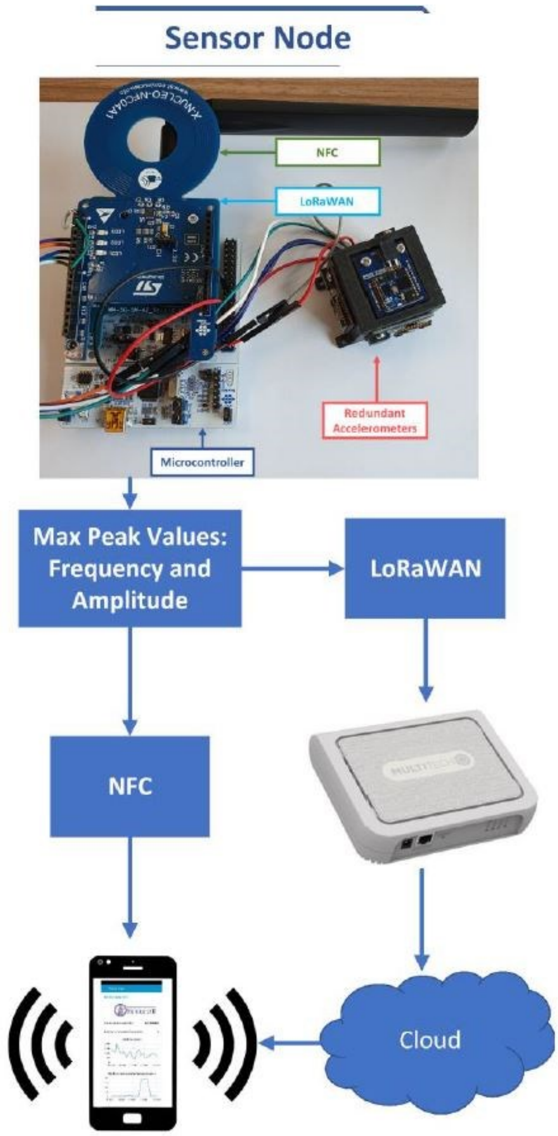

Figure 49. Sensor node and proposed smart monitoring architecture

The proposed architecture is designed to transmit only the maximum amplitude value of the signal, a value determined by the microcontroller as the peak within the frequency domain. Subsequently, the microcontroller transmits both the frequency and amplitude values, effectively minimizing the number of samples transmitted. This approach facilitates real-time monitoring and ensures that only pertinent information is conveyed, leading to a more efficient system protocol with fewer transmitted packets. This optimization streamlines the transmission of measured data via the LoRa and NFC protocols, thereby expediting NFC and Dashboard communications.

5.3 System Architecture

The hardware components, utilized for performance evaluation and the development of wireless sensor nodes for real-time monitoring, are presented in table 5 and table 6. Meanwhile, figures 50.a and 50.b illustrate the corresponding operation flow-chart.

Table 5. Performance evaluation equipment

Hardware	Part Number	Manufacturer
Redundant accelerometers	LSM6DSM (Six iNemos)	STMicroelectronics
Marine-grade accelerometers	STIM318	SensoNor
Microcontroller	Nucleo-F466RE	STMicroelectronics
Motor	StepSyn	SANYO DENKI
Motor Driver board	X-NUCLEO-IHM04A1	STMicroelectronics
Bluetooth module	RN41	Roving
RS422-UART	SN75C1167	Texas Instruments

Table 6. Sensor node realization hardware

Hardware	Part Number	Manufacturer
Microcontroller	Nucleo-F466RE	STMicroelectronics
Sensor board	X-NUCLEO-IKS02A1	STMicroelectronics
NFC Module	X-NUCLEO-NFC04A1	STMicroelectronics
LoRA Module	I-NUCLEO-LRWAN	STMicroelectronics
SPI-micro SD-Card	410-380	Diligent Inc.

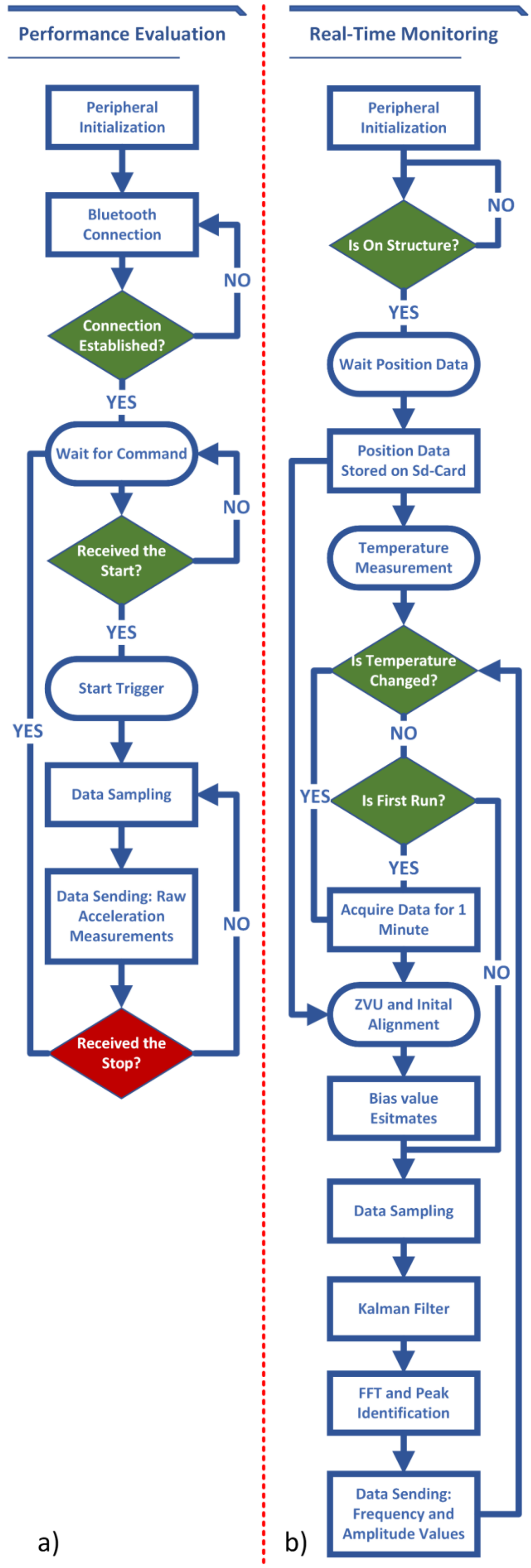

Figure 50. Data acquisition flow-chart for: a) performance evaluation; b) real-time monitoring

To ensure clarity, the redundant prototype consists of six iNemos from STMicroelectronics™ arranged in a cubic configuration. The communication between the microcontroller and the PC employs Bluetooth protocol (as depicted in Figure 50.a). This facilitates control over the beginning of data acquisition and collection. Once the start signal is transmitted, the microcontroller generates a trigger for the sensor modules and starts data collection from both modules. During testing, precise synchronization of measurements is crucial.

Therefore, data processing is conducted offline to prevent delays stemming from data acquisition in both systems. The software architecture prioritizes synchronization between both systems, aiming for comparable measurements with the reference system. This approach guarantees the reliability and accuracy of the results for meaningful comparisons.

Regarding the wireless sensor node, its software architecture is designed for real-time processing of acceleration measurements, as shown in Figure 50.b. In this setup, the microcontroller acquires and processes data following a specific method to evaluate the maximum frequency peak value. This value, along with associated amplitude values, is transmitted using the LoRaWAN protocol and NFC.

This solution relies on the ZVU filter for initial alignment and noise term evaluation. To enhance parameter estimations, it leverages GNSS position information. Consequently, the IoT architecture facilitates configuring these parameters, which can be stored on the Sd-Card. This configuration can be accomplished when the sensor node is affixed to a stationary structure. The ZVU and initial alignment, a 60 s process, is activated under two conditions:

1) Whenever the device is powered on to rectify random bias values.
2) Whenever the internal temperature of the accelerometer fluctuates by ±3°C, correcting bias value shifts due to temperature changes.

After estimating error values, the microcontroller filters out high-frequency noise from the raw acceleration measurements using the Kalman Filter. Subsequently, it processes the data with an FFT algorithm to determine the maximum frequency peak value and associated amplitude values. These results are then transmitted via IoT protocols, i.e. LoRAWAN and NFC.

5.4 Results

The proposed solution underwent evaluation using the measurement setup detailed in Section 5.1.1. In this assessment, oscillation measurements, specifically oscillation amplitudes, were compared across both systems at controlled frequencies ranging from 1 Hz to 5 Hz.

The performance of the proposed method was determined by contrasting the measurement outcomes obtained from the implemented system with those assured by a marine-grade MEMS sensor, the STIM318. The raw acceleration data were gathered by the concentrator and transmitted to a PC, where they were collected and processed using a Matlab code.

The advantages of the proposed method, which leverages the ZVU filter and initial alignment for calibration purposes-specifically, compensating for accelerometer bias drift values-were evident in the results. As illustrated in Figure 51, a comparison of the signal spectra from both systems revealed amplitude differences at 1 Hz between the proposed method (A_{est}) and the reference (A_{ref}) of 0.021 m/s^2, whereas the amplitude differences between the best sensor (i.e., one cube face, A_{one}) and the reference system were 0.137 m/s².

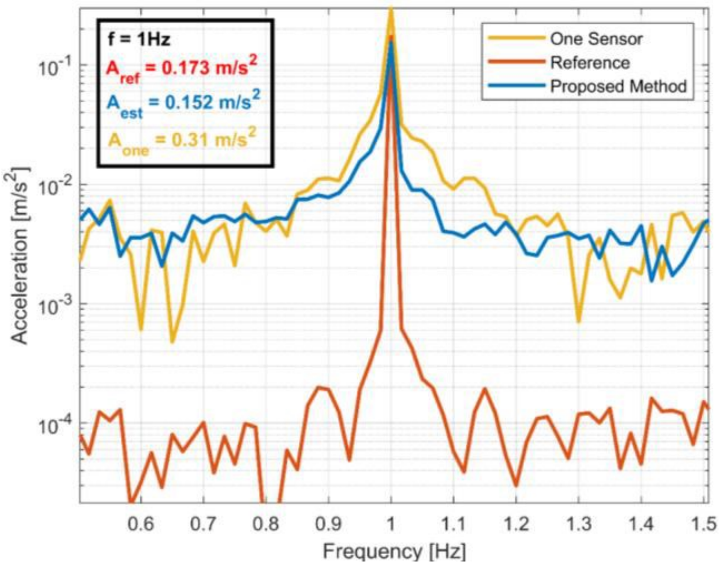

Figure 51. Acceleration amplitude comparison at 1Hz: reference system (red), proposed method (blue) and one sensor measures (orange)

While a comparison at a 1 Hz oscillation frequency is shown for clarity, similar results were obtained and are presented in Table 7. Additionally, theoretical amplitude values calculated according to equation 15 were reported.

Table 7. Acceleration amplitude results from 1Hz to 5Hz

Amplitude	Oscillation Frequency (Hz)				
	1	2	3	4	5
Reference System	0.173	0.767	1.754	3.123	4.914
Proposed Method	0.152	0.744	1.733	3.101	4.891
One Sensor	0.31	1.243	2.254	4.63	6.823
Theoretical acceleration	0.197	0.789	1.776	3.158	4.934

Table 8 highlights the benefits of the proposed method, reporting the differences between the reference system and estimated values (ΔA_{est}) as well as the reference system and the single sensor value (ΔA_{one}).

Table 8. Amplitude differences between the reference system and (i) the proposed method; (ii) one accelerometer sensor measures

Amplitude differences (m/s^2)	Oscillation Frequency (Hz)				
	1	2	3	4	5
ΔA_{est}	0.021	0.023	0.021	0.022	0.022
ΔA_{one}	0.137	0.476	0.5	1.507	1.909

These results are further depicted in Figure 52, where the differences between the reference system and uncompensated measurements increase with frequency due to typical low-cost accelerometer errors. Conversely, the proposed method, with its ZVU calibration, compensates for bias drift and bias stability, resulting in stable performance as the frequency increases.

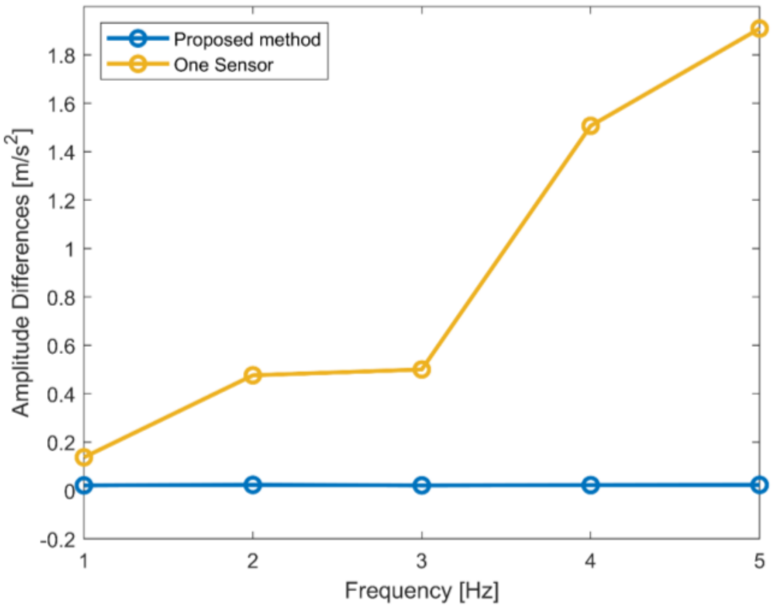

Figure 52. Differences as the frequency changes (from 1H z to 5 Hz), between the reference system and (i) the proposed method (blue); (ii) one sensor measures (orange)

Finally, Figure 53 demonstrates a second-order polynomial fit used to evaluate the quadratic trend of acceleration amplitude as frequency increases. The comparison reveals that the reference system and estimated acceleration amplitude values exhibit a similar trend to the ideal one, while uncompensated values exhibit significant drift with increasing frequency.

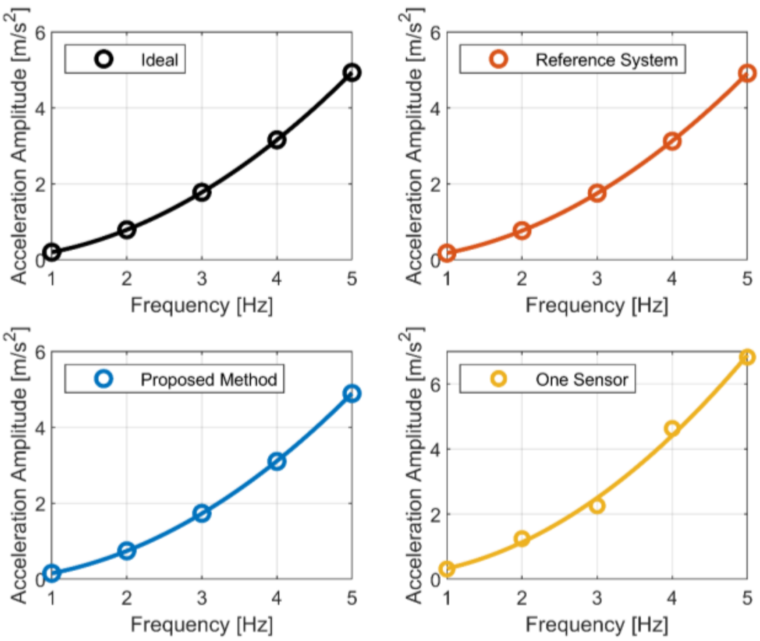

Figure 53. Polynomial fitting comparison: ideal trend (black), reference system (red), proposed method (blue) and, one sensor measure (orange)

With the performance verified, an example of sensor node operation, described in Section 5.1.2, is presented in figure 54. The monitoring dashboard is accessible from both smartphones and PCs, providing information on oscillation amplitude in *g* and about frequency. The complete dashboard also displays data from all sensor axes for clarity.

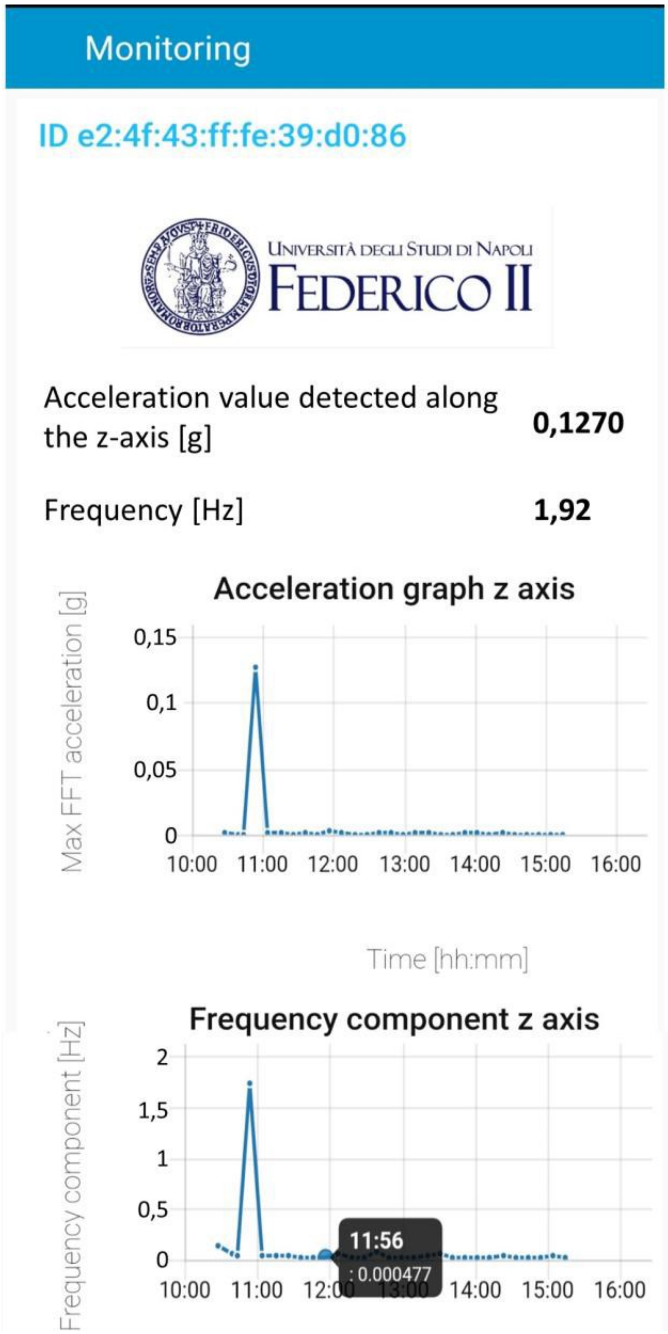

Figure 54. Monitoring dashboard example of operation

Chapter 6 - Failure Prediction for Railway Rolling Stock Equipment

In the railway domain, rolling stock maintenance is a critical factor that affects service operation time and efficiency. To minimize train unavailability and reduce capital loss and operational costs, it is essential to predict failures of rolling stock equipment and proactively trigger proper maintenance activities. Predictive maintenance is an excellent example of digital transformation within Industry 4.0, which has revolutionized several engineering processes in the railway domain.

The huge data collected from (smart) sensors and sent to diagnostic systems, either on-board or in a control room, can be utilized through appropriate methods to reveal degradation patterns of components and predict failures in a timely manner for optimal maintenance decisions. Railway transport operators typically depend on planned maintenance, which can lead to unnecessary actions and increased operating costs.

6.1 State of Art

Condition-based maintenance (CBM) is a relatively new extension that estimates the actual conditions of equipment through direct measurements; it enhances planned maintenance by being proactive, repairing or replacing degraded devices when certain conditions are met. Predictive Maintenance takes CBM a step further by using monitoring data and effective predictive techniques to determine when a fault is likely to occur. This allows companies to schedule maintenance operations when actually needed, resulting in cost reduction, reduced mean time to failures, repair stop reduction, and overall profit [148], [149]. The clear advantage is that maintenance is performed at the right time, i.e., before a fault occurs (preventing long downtime) but not unnecessarily too early, ultimately reducing the unavailability of rolling stock as well as infrastructure equipment.

Machine Learning (ML) algorithms are increasingly becoming essential tools for maintenance in various domains as they support predictive techniques. ML has been used to predict light bulb failure time [150], early detection of machine failures [151], rotating machinery failure prediction [152], remaining lifetime prediction of hard disks in computing clusters [153], [154] and Remaining Useful Life (RUL) of wind turbines

[155]. ML techniques have also been applied to evaluate the degradation of aircraft engine [156], [157] thanks to data made available by the NASA Prognostics Center of Excellence. ML handles high-dimensional and multivariate data and helps extract hidden relationships within data in complex and dynamic environments. ML is gaining popularity in improving operations and reliability in the railway domain as well. However, the performance of ML algorithms strongly depends on the appropriate choice of the ML technique [158]. Generally, rail systems deteriorate gradually over time or fail directly [159], leading to data that vary extremely slowly. Indeed, an ML approach for predictive maintenance should consider this type of data to accurately predict and forecast failures.
In the context of the railway domain, the focus has been on the following questions in the context of failure prediction for rolling stock equipment:

1. How to properly learn long-term dependencies for gradually changing data? (R1)
2. How to predict with high accuracy failures and their severity levels? (R2)
3. How to forecast with high accuracy failures? (R3)

To outline the questions above, a deep learning-based approach has been adopted. Specifically, the proposed approach enables the prediction and forecasting of failures in an ensemble to plan maintenance interventions before they occur, optimizing the overall cost and duration of maintenance interventions. It utilizes Long Short-Term Memory (LSTM) networks, an extension of recurrent neural networks (RNN), specifically designed to learn long-term dependencies for gradually changing data [160]. The proposed approach analyzes data from numerous sensors connected to various subsystems of a railway vehicle. The experimentation focuses on the train traction converter cooling subsystem, one of the most critical on-board systems.
They have been examined operational data from a train fleet over several months. The framework allows for classic statistical data analysis, such as trend estimation and correlation, to identify coarse-grained relationships between dataset features and failure characterization. It then uses LSTM networks to both predict and forecast failures, providing valuable insights to maintainers of rolling stock equipment.

This solution achieves over 99% accuracy for both prediction and forecasting tasks, outperforming other ML models and techniques in the predictive maintenance literature. Furthermore, when comparing the error in prediction and forecasting tasks, it has been achieved a false alarm rate of approximately ~0.4% and a mean absolute error on the order of 10^{-4}, respectively, which are very promising compared to existing studies. This methodology has been validated by an industry partner against the real target system, acknowledging the proper assumptions and approaches.

This solution is the first attempt at leveraging LSTM machine learning models to both predict and forecast failures of a critical train traction subsystem. The proposed methodology combines LSTM models with an advanced data pre-processing algorithm, with the final aim of supporting the optimization of maintenance activities and reducing train unavailability. It has experimented on real train operational data provided by the industry partner, producing remarkable results acknowledged by the domain experts.

6.2 Background

In this section, it will be exposed the foundational concepts necessary to comprehend the proposed methodology. The first subsection provides an insight into the cooling system of the traction converter, which serves as the central focus in the experimental section. This understanding is pivotal in delineating the essential factors that need consideration for the optimal functioning of rail vehicle traction and the detection of any potential failures. Given the gradual and evolving nature of these critical factors, it has been harnessed the capabilities of the LSTM machine learning model, which adeptly accommodates such dynamic behaviors. The second subsection it will be explored the fundamental principles of LSTM networks, which constitute a cornerstone within the framework of the proposed methodology.

6.2.1 Traction Converter Cooling System

This section provides an overview of the traction converter cooling system, which serves as the focal point for the application of the methodology detailed in Section 6.2.

Within the railway domain, the efficient cooling of electronic equipment plays a critical role in maintaining proper control over the temperature of semiconductor junctions. To facilitate effective heat transfer, a mixture of water and glycol was chosen as the medium due to its high thermal conductivity. The cooling system primarily comprises several components, including a liquid tank/expansion tank, a pump, a heat exchanger housing the modules to be cooled, and various measuring and control equipment. In the specific system, the hydraulic circuit is responsible for cooling two main power inverter modules and one auxiliary module. This hydraulic circuit efficiently cools the *Insulated Gate Bipolar Transistors* (IGBT) and resistors on each of these three modules, utilizing high thermal efficiency plates. Subsequently, the heated liquid undergoes cooling through a heat exchanger with forced ventilation air.

Positioned above the train, within a converter box, the cooling system draws in air from the front of the carriage (in the direction of the train) and expels it to the sides after passing through a sealed compartment that houses transformers and inductors.

Figure 55 illustrates the hydraulic circuit's block diagram, along with its components and measuring equipment:

- The *WT* control unit tank serves as both a filling and compensation tank, accommodating variations in fluid volume due to temperature fluctuations. The safety valve (VS) is employed to release excess pressure if abnormal overpressures occur.
- *TL1* and *TL2* switches are responsible for monitoring the cooling liquid level. *TL1* triggers a pre-alarm for liquid refilling when volume reduction is detected, while *TL2* indicates that the minimum admissible level has been reached, leading to system shutdown (excluding the converter).
- The *PM1* centrifugal pump ensures proper liquid circulation at the required flow rate.
- The *PS* pressure switch, located on the delivery pipe, is set to a minimum pressure value. Crossing this threshold can indicate malfunctions in the pump or improper valve positioning, leading to a system shutdown.
- The *P1* pressure gauge displays the pressure value within the system.

- On the return line, the flow sensor (SF), connected to the *Flow Control Board FL1* (Coflu/4 Assembly), monitors and regulates the liquid flow rate. The board is configured with a minimum flow rate, below which adequate cooling cannot be guaranteed, resulting in a system shutdown.
- During operation, the filter basket (F) traps particles larger than a specified threshold. The filter is disregarded in the nominal operating position.
- Within each module (external to the control unit), *PT100* RTDs are present, set to temperature limits suitable for semiconductor functionality. These thermometers enable continuous temperature monitoring.

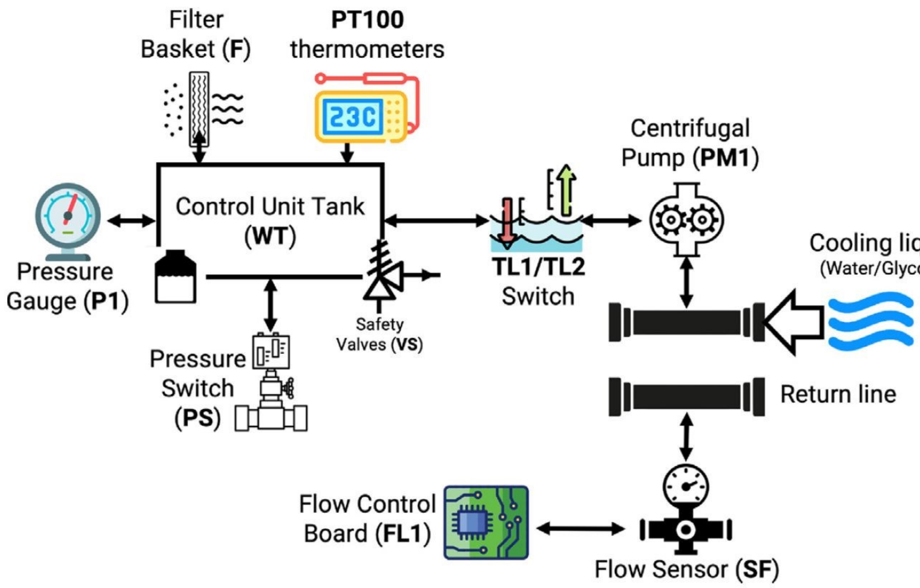

Figure 55. Hydraulic circuit, converters unit

All components are subject to continuous monitoring, and data are collected in datasets provided by the industrial partner. These datasets can be analyzed to uncover long-term dependencies among measurements of critical physical dimensions within the traction system. The experimentation focuses on measurements related to the cooling liquid level (i.e., Status Level (*TL1*/*TL2*)) and the flow sensor within the flow control board (i.e., Assembly FTF (*FL1*)). These components significantly impact the operation of traction systems, as it will be showed in section 6.2.

Figure 56 illustrates a trend of the cooling liquid flow rate in a traction control unit, specifically the *TACU1_H2OFlow* feature in a dataset. This trend exhibits gradual changes, with intermittent periods of signal drop to zero, indicating operational failures. Recognizing these pattern characteristics, it has been employed a machine learning model capable of identifying such trends. It has been harnessed the LSTM model to address research question R1, which centers on the proper learning of long-term dependencies in gradually changing data.

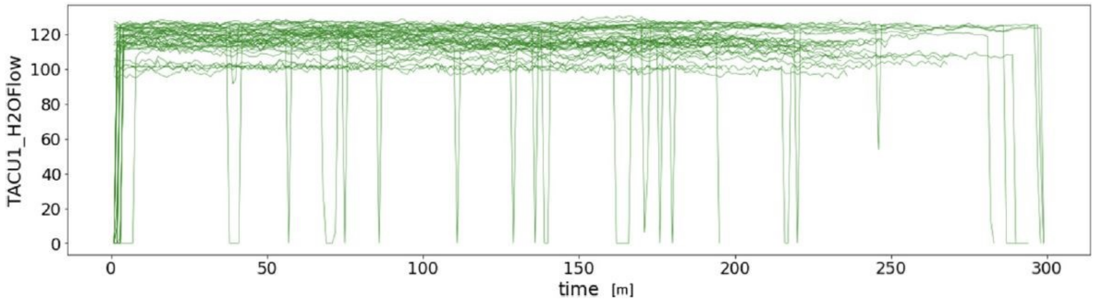

Figure 56. An example of the TACU H2O flow feature signal trend over time

6.2.2 Long Short-Term Memory Networks

Due to the sequential and gradually changing nature of the features within our dataset, it is crucial to capture their dependencies over time in the model. To achieve this, it has been employed a LSTM networks, an extension of *Recurrent Neural Networks* (RNNs) designed to address the issues of gradient vanishing and explosion [160], [161]. LSTM networks are able to retain memory of temporal dependencies among inputs for extended periods.

Figure 57 provides an insight into the internal structure of an LSTM cell, comprising three gates: the input gate, the forget gate, and the exit gate.

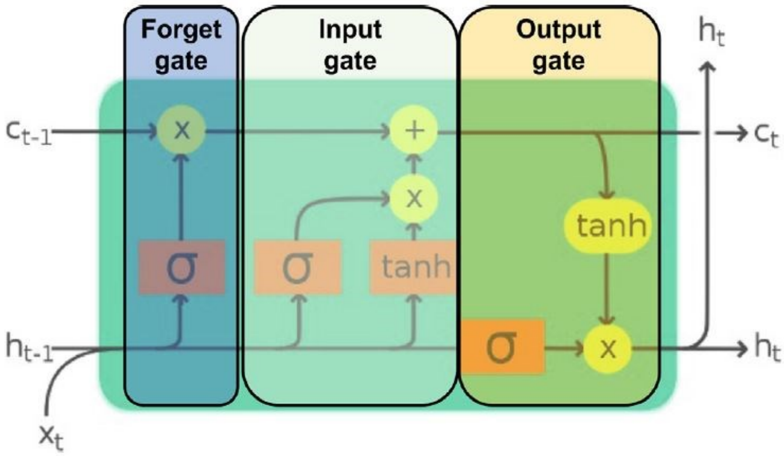

Figure 57. Internal structure of an LSTM cell

These gates are governed by the following equations:

$$f_t = \sigma_g\left(W_f x_t + U_f h_{t-1} + b_f\right) \tag{16}$$

$$i_t = \sigma_g(W_i x_t + U_i h_{t-1} + b_i) \tag{17}$$

$$c_t = \sigma_c(W_c x_t + U_c h_{t-1} + b_c) \tag{18}$$

$$c_t = f_t \odot c_{t-1} \odot i_t \odot \tilde{c_t} \tag{19}$$

$$o_t = \sigma_g(W_o x_t + U_o h_{t-1} + b_o) \tag{20}$$

$$h_t = o_t \odot \sigma_h(c_t) \tag{21}$$

Here:

- f_t, i_t, o_t represent the forget gate, input gate, and output gate, respectively.
- W_f, W_i, W_c, W_o are the weight matrices corresponding to the gates.
- U_f, U_i, U_c, U_o denote the recurrent connections to the gates.
- σ_g, σ_c, and σ_h refer to the sigmoid function, hyperbolic tangent function, and hyperbolic tangent function, respectively.
- $\odot$ denotes the Hadamard product (element-wise product).

The initial step in the LSTM cell processes incoming data by determining what information to retain, as regulated by Eq. (16). The x_t data array, containing feature values at time *t*, is input alongside the previous output h_{t-1}. The result undergoes an activation function (sigmoid σ_g), yielding values between 0 and 1 for each element of the cell state c_{t-1}, indicating whether to disregard or store the element over time. The subsequent step involves the input gate, determining which new information to store, as per Eqs. (17) and (18). The LSTM cell state is then updated through Eq. (19). Lastly, the LSTM output is generated through Eqs. (20) and (21), selecting the portion of the new state to be outputted.

6.3 Methodology

Given the sequential and gradually changing nature of the features in our dataset, it is essential to capture dependencies among these features over time. The methodology, which relies on LSTM networks, is depicted in Fig. 58 and encompasses the following key steps:

1. *Data Exploration*: In this initial phase, data collected from various sensors in the system are meticulously analyzed. The objective is to uncover relationships between the current characteristics and establish trends over time. The insights gained during this exploration are invaluable for detecting faults within the system.
2. *Data Pre-processing*: This step involves preparing the dataset for the subsequent prediction phase. It encompasses various data manipulation tasks, including data cleaning, spike filtering, route extraction, and sequence extraction.

3. *Fault Analysis*: After completing the pre-processing steps, the methodology proceeds to the core of the analysis. Here, we conduct both failure prediction (classification) and forecasting tasks using LSTM networks. These tasks are performed individually for each temporal sequence, taking into account the data transformations and enhancements carried out during the pre-processing step.

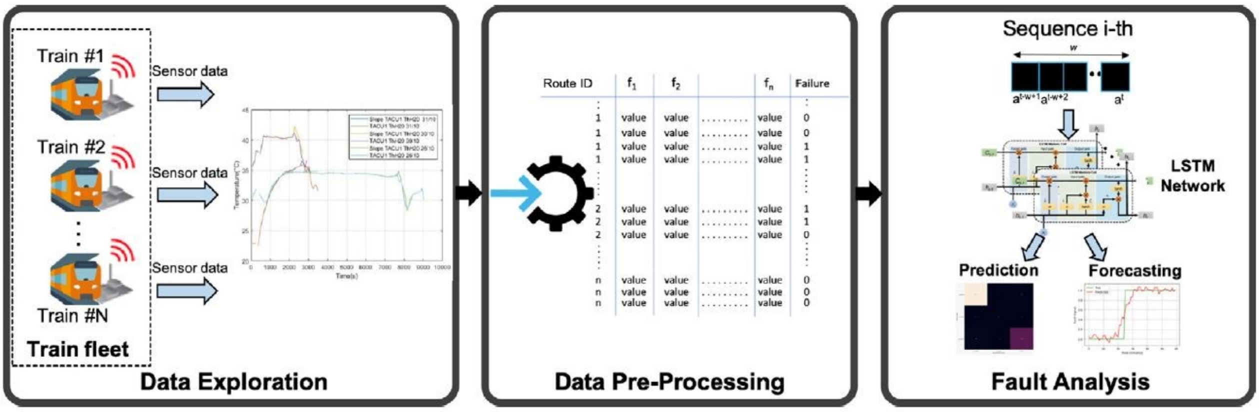

Figure 58. The proposed failure prediction methodology

By following these steps, the methodology leverages LSTM networks to analyze the dataset, identify trends, and make predictions related to failures in the system. This approach allows us to effectively capture the time-dependent dependencies among the features, which is crucial for accurate fault detection and forecasting.

6.3.1 Data Exploration

The available dataset comprises data collected from sensors and control units within the traction converter cooling system. This dataset also encompasses additional information, such as the train identifier, GPS coordinates denoting train location, current train speed, and timestamps for each measurement. In total, the dataset comprises 79.861 samples, encompassing 131 distinct features. These features represent time series data related to a fleet of 10 different trains in operation during a specific time period. This specific time frame was chosen as it was identified by our industry partner as the most critical period for their train fleet.

The available dataset has an incoherent data sampling rate: for the majority of the dataset, the sampling time is 60 s, while for a portion of the dataset, the sampling time has dropped to 1 s.

To ensure consistency, a data pre-processing step was undertaken, specifically in the data cleaning phase, to standardize the sampling interval to 60 s.

Additionally, alongside the traction converter cooling system dataset, our industry partner provided another dataset containing diagnostic information about failures that occurred during train operations within the same time frame. This dataset includes details about diagnostic events, brief descriptions of these events, their durations, and the specific train involved in each event. This dataset plays a crucial role in gaining insights into maintenance and predicting faults within the system.

All raw data in these datasets were collected by our industry partner using their proprietary network of Internet of Things (IoT) sensors installed on-board the trains. These sensors have a direct connection to a centralized database system capable of storing a substantial volume of timestamped data. After a train completes its daily operation, an operator triggers the process of storing the recorded data in this centralized database. This database can be accessed for further analysis. However, specific details regarding the monitoring architecture cannot be disclosed due to a non-disclosure agreement.

To gain deeper insights into the dataset's features, the initial step involves conducting statistical tests to uncover potential trends within the dataset and to identify possible correlations between features. The Mann–Kendall test was employed to detect trends [162], while covariance and correlation analyses were conducted to explore feature relationships [163].

In the case study, this initial step revealed an unexpected correlation between the IGBT sensor (*TACU1_ThIGbt2 feature*) and the temperature of the cooling circuit (*TACU3_ThH20 feature*). Additionally, an interesting finding emerged when both the Mann–Kendall and covariance tests failed to identify an anomaly. This discovery was later corroborated by comparing the results with the available diagnostic data. Specifically, the anomalies identified were related to events involving the flow rate (particularly low or below the minimum) and the level (low or very low) of the cooling liquid. Our industry partner confirmed that diagnostic events associated with low flow

rates (e.g., *TACU_FL1* with low severity) and low cooling liquid levels (e.g., *TACU_TL1* with low severity) are precursors to train traction failures.
Given the dataset's size and complexity, it was decided to partition it into different routes traveled by the trains for more focused analysis and prediction tasks.

6.3.2 Data Pre-Processing

During this step, a series of essential operations are carried out to prepare the dataset for training the LSTM algorithm.

6.3.2.1. Data Cleaning

When dealing with data collected from physical sensors, data cleaning is a crucial initial step in their analysis. This process involves:

- *Removing Missing or Incomplete Data*: Values within the dataset that are blank or represented as special values (e.g., Not a Number or Null) are eliminated.
- *Eliminating Unusual Values*: Any values that deviate significantly from the normal distribution of the dataset are removed.
- *Correcting Data Formatting*: The dataset is reviewed to ensure that all data are correctly formatted, particularly concerning decimal values represented with a point (.) instead of a comma (,).
- *Identifying and Combining Redundant Values*: Duplicate or redundant data entries that convey the same information are identified and combined.

Additionally, the dataset initially had data sampled at varying time intervals. To ensure consistency, a simple algorithm was used to standardize the data sampling to 60 s intervals. This involved analyzing data sampled every second and averaging them over one-minute intervals.

6.3.2.2. Routes Extraction

To facilitate further analysis for the deep learning model, a specialized strategy was employed to extract train routes from the dataset. The algorithm used does not rely solely on GPS coordinates for determining train positions, as this information can be unreliable for inferring train routes. Instead, the algorithm leverages the stop times of trains at stations to identify the start of new train routes. A threshold of approximately 10 minutes was determined to be effective in recognizing route changes, resulting in the identification of 63 unique train routes.

6.3.2.3. Spike Filtering

For fault prediction using LSTM networks, it is essential to assign error labels to each sample in the dataset. To achieve this, diagnostic data related to failures were integrated into the traction converter cooling system dataset. However, a preliminary analysis of the enhanced dataset revealed several spikes that could potentially disrupt LSTM predictions due to significant signal fluctuations.

For example (Figure 59), the aggregate signal for diagnostic events like *TACU_TL1*, *TACU_TL2* (indicating low and very low levels of cooling liquid) and *TACU_FL1*, *TACU_FL2* (indicating low or below the minimum flow rate) displayed numerous spikes of varying durations. In these signals, a 0-signal indicated the absence of failures, while a 1-signal indicated a failure of specific duration over time, according to the analyzed route.

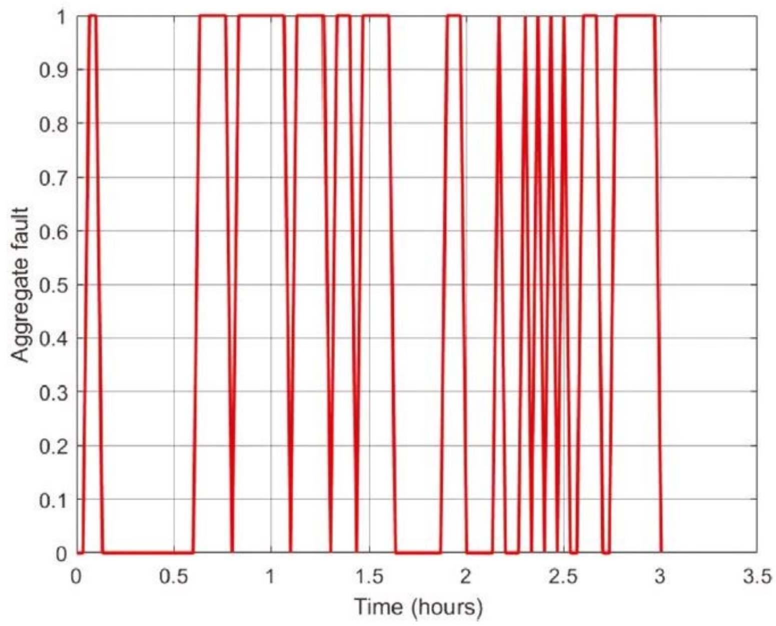

Figure 59. Aggregate signal of diagnostic events TACU_TL1, TACU_TL2, TACU_FL1, TACU_FL2 series over time for a specific train route,

To address this spike issue, an algorithm (Figure 60) was developed to evaluate the duration of each spike for each route and determine whether it should be filtered out as noise or retained as a significant event. The filtering process follows several rules:

- Spikes with durations less than or equal to a defined threshold (*low_thr*, set at 240 s) are filtered out as non-significant diagnostic events.
- Spikes forming a consecutive sequence (spikes' train) with a count of less than a specified limit (*max_spike_count*, set at 3) are filtered out.
- For spikes' trains with a count greater than *max_spike_count*, the algorithm merges the diagnostic event samples into a single high signal.
- In cases where a current diagnostic event sample's duration is greater than or equal to *high_thr* (set at 800 s), the algorithm identifies the next significant diagnostic event sample and computes the spikes' train between these two samples. Only the first spike in that train is retained as high, and the remaining spikes are filtered out.

```
Input: Traction converter cooling system dataset enhanced with
       failure events. low_thr = 240s, high_thr = 800s,
       max_spike_count = 3
Output: Traction converter cooling system dataset with spikes filtered
while Route is available in the route list do
    while Diagnostic event is available in the route do
        Compute the duration of the event;
        if Duration ≤ low_thr then
            Count the number of consecutive spikes (spikes' train);
            if spikes' train size is ≤ max_spike_count then
                Filter the current event and the related spike's train;
            else
                Merge all the spikes within the spikes' train as one
                 high signal;
            end
        else if Duration > low_thr and < high_thr then
            Ignore the event;
        else if Duration ≥ high_thr then
            Find the first next significant failure (duration ≥
             high_thr);
            Count the number of spikes (signal with duration ≤
             low_thr) between the two signals;
            Keep high only the first spike and filter out the
             remaining spikes in the spikes' train;
        end
    end
end
```

Figure 60. Algorithm pseudo-code for spike filtering

After applying this spike filtering algorithm, the aggregate signal for the targeted diagnostic events exhibited smoother behavior (Figure 61).

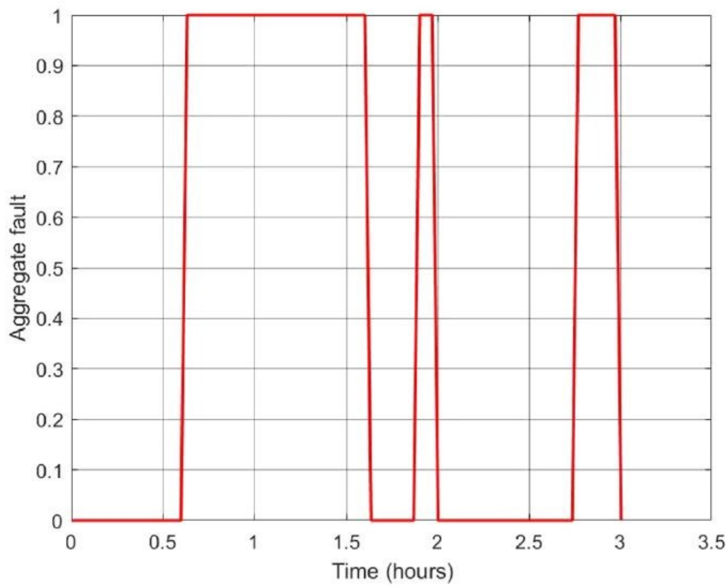

Figure 61. Aggregate signal of diagnostic events after application of spike filtering algorithm.

6.3.2.4. Sequence Extraction

To explore the time dependencies within the periodically collected sensor data, characteristic sequences are extracted using specific time windows (*TW*). For each time window of size *w* and the set of features (f_1, f_2,... f_n) at time t, the goal is to predict the health status at time t + 1 (*Hs(t+1)*). This is done by considering the sequence (a^{t-w+1}, . . . , a^{t-1}, a^t).

Each health status *Hs(t)* is defined for each a^t, and the feature sequence at time *t* is extracted, considering the *w-1* previous samples. This process results in sequences that consist of bi-dimensional arrays of size $w \times n$, where *n* is the number of considered features. The outcome of this step is a dataset organized based on sequences, with each sequence representing the health condition of the traction converter cooling system between two consecutive samples (i.e., a^t and a^{t+1}).

This sequence-based dataset is now suitable for further analysis and the training of the LSTM algorithm, as it preserves the temporal dependencies within the features.

6.3.3 Fault Analysis

This phase involves the execution of both a multiclass classification task and a forecasting task. To provide more detail, it has been defined three severity levels, as suggested by our industry partner, to categorize the components under analysis based on their severity. In the classification task, each feature sequence is assigned to one of the following classes: "*Good*," "*Minor*," or "*Major*." Specifically, these classes represent:

1. *Good*: This class denotes a normal state of the component, indicating that everything is operating within expected parameters.
2. *Minor*: This class serves as a warning, signaling issues related to the flow rate of the cooling liquid, which could be either low or below the minimum acceptable level.
3. *Major*: This class signifies a severe issue, indicating a very low level of the cooling liquid, which poses a significant risk or problem.

In the forecasting task, each feature sequence, which has been extracted with a specific time window (*TW*), is labeled based on the trend of the features in the subsequent sequence, which represents the prediction window.
The input format for each LSTM layer is a three-dimensional data structure with dimensions $z \times w \times n$, where:

- z represents the total number of sequences (or the batch size in each iteration).
- w corresponds to the size of each sequence, essentially representing the length of a time window in terms of time steps.
- n signifies the total number of features describing each time step.

The network architecture consists of two stacked LSTM layers, each containing 256 units, followed by a single dense layer. This neural network configuration is designed to handle the classification and forecasting tasks effectively, leveraging the temporal dependencies within the dataset to make accurate predictions and classifications based on the specified severity levels.

CONCLUSIONS

In this thesis work has been explored the multifaceted applications of the Internet of Things and its transformative impact on various domains. It is possible to conclude that it is evident that IoT is not just a technological advancement; it represents a paradigm shift in how we interact with and leverage technology to enhance our lives.

Section 1 - IoT Device to Remotely Control System:

In Section 1, has been presented a framework to remotely control laboratory instruments. It has been explored case studies and user experiences, revealing the seamless integration of remote instrument control. The application of a Cyber-Physical System, with a focus on Augmented Reality, showcased the potential of connecting the physical world with digital applications. Additionally, it has been examined a solution for remote instrument control in safe experiments, accompanied by a case study on gamma ray energy spectrum measurements. The hardware and software architecture, together with experimental results, demonstrated the efficacy of this approach.

Section 2 - IoT for Localization and Monitoring:

Bluetooth Low-Energy Fingerprinting has offered an innovative approach for implementing a Passive Entry/Passive Start (PEPS) system. Results highlighted the potential of this technology, aided by the ESP32 microcontroller and radio map realization. The statistical inferences and classification learner models highlighted the analytical depth of this system.

Then has been showed a smart system to monitor oscillation for bridges. Proprietary methods, including zero-velocity update filters and Kalman filter techniques, were detailed. The proposed smart monitoring architecture and system design contributed to a holistic understanding of this innovation. Furthermore, the results indicated the potential for smarter, more efficient monitoring solutions.

Finally has been showed a the importance to predict failure for railway rolling stock equipment. The methodology, encompassing data exploration, pre-processing, and fault analysis, emphasized the significance of data-driven insights in ensuring the safety and reliability of railway systems.

In conclusion, IoT has become an integral part of our modern world, transcending boundaries and reshaping industries. It empowers us to remotely control instruments, track and monitor objects with precision, and harness the capabilities of artificial intelligence to predict and improve performance. In the future, IoT will continue to drive innovation, offering new opportunities to enhance our lives and address the challenges of an increasingly interconnected world. The arguments explored are just the beginning, and the future holds even more remarkable possibilities for IoT's role in shaping our world.

BIBLIOGRAPHY

[1] G. Andria *et al.*, "Remote didactic laboratory 'G. Savastano,'The Italian experience for E-Learning at the technical universities in the field of electrical and electronic measurement: Architecture and optimization of the communication performance based on thin client technology," *IEEE Trans Instrum Meas*, vol. 56, no. 4, 2007, doi: 10.1109/TIM.2007.899983.

[2] G. Andria *et al.*, "Remote didactic laboratory 'G. Savastano,'The Italian experience for E-Learning at the technical universities in the field of electrical and electronic measurements: Overview on didactic experiments," *IEEE Trans Instrum Meas*, vol. 56, no. 4, 2007, doi: 10.1109/TIM.2007.899995.

[3] A. Baccigalupi, U. Cesaro, M. D'Arco, and A. Liccardo, "Web-based networking protocol for expanding IEEE-488 ATE capabilities," in *M and N 2011 - IEEE International Workshop on Measurements and Networking, Proceedings*, 2011. doi: 10.1109/IWMN.2011.6088503.

[4] K. P. S. Rana, V. Kumar, and J. Mendiratta, "An educational laboratory virtual instrumentation suite assisted experiment for studying fundamentals of series resistance–inductance–capacitance circuit," *European Journal of Engineering Education*, vol. 42, no. 6, 2017, doi: 10.1080/03043797.2017.1284764.

[5] P. Spanik, L. Hargas, M. Hrianka, and I. Kozehuba, "Application of virtual instrumentation lab VIEW for power electronic system analysis," in *EPE-PEMC 2006: 12th International Power Electronics and Motion Control Conference, Proceedings*, 2007. doi: 10.1109/EPEPEMC.2006.283455.

[6] L. Iannucci, M. Parvis, E. Di Francia, and S. Grassini, "IHomeX: An Internet-Enabled Laboratory for Long-Term Experiment Management," *IEEE Trans Instrum Meas*, vol. 67, no. 5, 2018, doi: 10.1109/TIM.2017.2786740.

[7] C. S. Tzafestas, N. Palaiologou, and M. Alifragis, "Virtual and remote robotic laboratory: Comparative experimental evaluation," *IEEE Transactions on Education*, vol. 49, no. 3, 2006, doi: 10.1109/TE.2006.879255.

[8] X. Chen, G. Song, and Y. Zhang, "Virtual and remote laboratory development: A review," in *Proceedings of the 12th International Conference on Engineering, Science, Construction, and Operations in Challenging Environments - Earth and Space 2010*, 2010. doi: 10.1061/41096(366)368.

[9] A. Ferrero, S. Salicone, C. Bonora, and M. Parmigiani, "ReMLab: A Java-based remote, didactic measurement laboratory," *IEEE Trans Instrum Meas*, vol. 52, no. 3, 2003, doi: 10.1109/TIM.2003.814695.

[10] M. A. Stegawski and R. Schaumann, "A new virtual-instrumentation-based experimenting environment for undergraduate laboratories with application in research and manufacturing," *IEEE Trans Instrum Meas*, vol. 47, no. 6, 1998, doi: 10.1109/19.746720.

[11] M. Stefanovic, V. Cvijetkovic, M. Matijevic, and V. Simic, "A LabVIEW-based remote laboratory experiments for control engineering education," *Computer Applications in Engineering Education*, vol. 19, no. 3, 2011, doi: 10.1002/cae.20334.

[12] C. A. Jara, F. A. Candelas, S. T. Puente, and F. Torres, “Hands-on experiences of undergraduate students in Automatics and Robotics using a virtual and remote laboratory,” *Comput Educ*, vol. 57, no. 4, 2011, doi: 10.1016/j.compedu.2011.07.003.

[13] A. P. J. Chandra and C. R. Venugopal, “Novel design solutions for remote access, acquire and control of laboratory experiments on DC machines,” *IEEE Trans Instrum Meas*, vol. 61, no. 2, 2012, doi: 10.1109/TIM.2011.2164291.

[14] N. Sousa, G. R. Alves, and M. G. Gericota, “An integrated reusable remote laboratory to complement electronics teaching,” *IEEE Transactions on Learning Technologies*, vol. 3, no. 3, 2010, doi: 10.1109/TLT.2009.51.

[15] E. Fabregas, G. Farias, S. Dormido-Canto, S. Dormido, and F. Esquembre, “Developing a remote laboratory for engineering education,” *Comput Educ*, vol. 57, no. 2, 2011, doi: 10.1016/j.compedu.2011.02.015.

[16] V. Paelke, “Augmented reality in the smart factory: Supporting workers in an industry 4.0. environment,” in *19th IEEE International Conference on Emerging Technologies and Factory Automation, ETFA 2014*, 2014. doi: 10.1109/ETFA.2014.7005252.

[17] F. Bademosi, N. Blinn, and R. R. A. Issa, “Use of augmented reality technology to enhance comprehension of construction assemblies,” *Journal of Information Technology in Construction*, vol. 24, 2019.

[18] Y. L. Zhukovskiy and N. I. Koteleva, “Electrical equipment maintenance system with elements of augmented reality technology,” in *IOP Conference Series: Materials Science and Engineering*, 2019. doi: 10.1088/1757-899X/643/1/012024.

[19] L. Angrisani, F. Bonavolontà, A. Liccardo, R. S. Lo Moriello, and F. Serino, “Smart power meters in augmented reality environment for electricity consumption awareness,” *Energies (Basel)*, vol. 11, no. 9, 2018, doi: 10.3390/en11092303.

[20] J. M. Andújar, A. Mejias, and M. A. Marquez, “Augmented reality for the improvement of remote laboratories: An augmented remote laboratory,” *IEEE Transactions on Education*, vol. 54, no. 3, 2011, doi: 10.1109/TE.2010.2085047.

[21] S. J. Lu and Y. C. Liu, “Integrating augmented reality technology to enhance children’s learning in marine education,” *Environ Educ Res*, vol. 21, no. 4, 2015, doi: 10.1080/13504622.2014.911247.

[22] S. Boonbrahm, C. Kaewrat, and P. Boonbrahm, “Using augmented reality technology in assisting english learning for primary school students,” in *Lecture Notes in Computer Science (including subseries Lecture Notes in Artificial Intelligence and Lecture Notes in Bioinformatics)*, 2015. doi: 10.1007/978-3-319-20609-7_3.

[23] T. Kondo, “Augmented Learning Environment using Mixed Reality Technology,” in *Proceedings of World Conference on E-Learning in Corporate, Government, Healthcare, and Higher Education 2006*, 2006.

[24] M. T. Abhishek, P. S. Aswin, N. C. Akhil, A. Souban, S. K. Muhammedali, and A. Vial, “Virtual Lab Using Markerless Augmented Reality,” in *Proceedings of 2018 IEEE International Conference on Teaching, Assessment, and Learning for Engineering, TALE 2018*, 2019. doi: 10.1109/TALE.2018.8615245.

[25] F. Liarokapis *et al.*, “Web3D and Augmented Reality to support Engineering Education,” *UNESCO International Centre for Engineering Education (UICEE) journal of World Transactions on Engineering and Technology Education*, vol. 3(1), 2004.

[26] Z. Nedic, J. Machotka, and A. Nafalski, “Remote laboratories versus virtual and real laboratories,” in *Proceedings - Frontiers in Education Conference, FIE*, 2003. doi: 10.1109/FIE.2003.1263343.

[27] B. Balamuralithara and P. C. Woods, “Virtual laboratories in engineering education: the simulation lab and remote lab,” *Computer Applications in Engineering Education*, vol. 17, no. 1, 2009, doi: 10.1002/cae.20186.

[28] L. Angrisani, F. Bonavolonta, M. Daarco, A. Liccardo, and O. Tamburis, “Internet-oriented measurement and automation project for Industry 4.0 educational program,” in *2019 IEEE International Symposium on Measurements and Networking, M and N 2019 - Proceedings*, 2019. doi: 10.1109/IWMN.2019.8805014.

[29] N. Naik, “Choice of effective messaging protocols for IoT systems: MQTT, CoAP, AMQP and HTTP,” in *2017 IEEE International Symposium on Systems Engineering, ISSE 2017 - Proceedings*, 2017. doi: 10.1109/SysEng.2017.8088251.

[30] G. C. Hillar, *MQTT Essentials - A Lightweight IoT Protocol*, vol. 53, no. 9. 2017.

[31] M. Martorelli, P. Ausiello, and R. Morrone, “A new method to assess the accuracy of a Cone Beam Computed Tomography scanner by using a non-contact reverse engineering technique,” *J Dent*, vol. 42, no. 4, 2014, doi: 10.1016/j.jdent.2013.12.018.

[32] M. Martorelli, S. Maietta, A. Gloria, R. De Santis, E. Pei, and A. Lanzotti, “Design and Analysis of 3D Customized Models of a Human Mandible,” in *Procedia CIRP*, 2016. doi: 10.1016/j.procir.2015.11.016.

[33] M. Martorelli, C. Pensa, and D. Speranza, “Digital Photogrammetry for Documentation of Maritime Heritage,” *Journal of Maritime Archaeology*, vol. 9, no. 1, 2014, doi: 10.1007/s11457-014-9124-x.

[34] B. Macy, “Reverse engineering for additive manufacturing,” in *Handbook of Manufacturing Engineering and Technology*, Springer, 2015, pp. 2485–2504.

[35] U. Technologies, “Build quality learning apps, games and simulations,” *Unity*. [Online]. Available: https://unity.com/solutions/edtech

[36] S. L. Kim, H. J. Suk, J. H. Kang, J. M. Jung, T. H. Laine, and J. Westlin, “Using Unity 3D to facilitate mobile augmented reality game development,” in *2014 IEEE World Forum on Internet of Things, WF-IoT 2014*, 2014. doi: 10.1109/WF-IoT.2014.6803110.

[37] “Vuforia Developer Portal,” *Vuforia Developer Portal*. [Online]. Available: https://developer.vuforia.com/

[38] A. Simonetti Ibañez and J. Paredes Figueras, “Vuforia v1. 5 SDK: Analysis and evaluation of capabilities,” Universitat Politècnica de Catalunya, 2013.

[39] J. Linowes and K. Babinlinski, *Augmented reality for Developer: Build practical augmented reality applications with Unity, ARCore, ARKit, and Vuforia*, vol. 433–435. 2017.

[40] X. Liu1, Y.-H. Sohn, and D.-W. Park, “Application Development with Augmented Reality Technique using Unity 3D and Vuforia,” 2018.

[41] J. Glover, *Unity 2018 augmented reality projects: build four immersive and fun AR applications using ARKit, ARCore, and Vuforia*. Packt Publishing Ltd, 2018.

[42] M. Sarosa, A. Chalim, S. Suhari, Z. Sari, and H. B. Hakim, “Developing augmented reality based application for character education using unity with Vuforia SDK,” in *Journal of Physics: Conference Series*, 2019. doi: 10.1088/1742-6596/1375/1/012035.

[43] S. Jackson, *Unity 3D UI essentials*. Packt Publishing Ltd, 2015.

[44] "IEC/IEEE International Standard - Higher Performance Protocol for the Standard Digital Interface for Programmable Instrumentation - Part 1: General," *IEEE 488.1 IEC 60488-1 First edition 2004-07*, pp. 1–158, 2004.
[45] "IEC/IEEE International - Standard Digital Interface for Programmable Instrumentation - Part 2: Codes, formats, protocols and common commands," *IEEE 488.2 IEC 60488-2 First edition 2004-05*, pp. 1–264, 2004.
[46] S. Lee, H. Kim, D. K. Hong, and H. Ju, "Correlation analysis of MQTT loss and delay according to QoS level," in *International Conference on Information Networking*, 2013. doi: 10.1109/ICOIN.2013.6496715.
[47] "Agilent 33220A 20 MHz Waveform Generator User Guide," no. 33220–90002. 2007.
[48] R. Bahati and H. Gill, "Cyber-physical Systems. The Impact of Control Technology," *Open J. Soc. Sci. Sci. Res. Publ*, vol. 5, pp. 161–166, 2011.
[49] M. Bashendy, A. Tantawy, and A. Erradi, "Intrusion response systems for cyber-physical systems: A comprehensive survey," *Computers and Security*, vol. 124. 2023. doi: 10.1016/j.cose.2022.102984.
[50] S. Zanero, "Cyber-Physical Systems," *Computer (Long Beach Calif)*, vol. 50, no. 4, 2017, doi: 10.1109/MC.2017.105.
[51] W. Wolf, "Cyber-physical systems," *Computer (Long Beach Calif)*, vol. 42, no. 03, pp. 88–89, 2009.
[52] F. Cicirelli *et al.*, "Edge computing and social internet of things for large-scale smart environments development," *IEEE Internet Things J*, vol. 5, no. 4, 2017, doi: 10.1109/JIOT.2017.2775739.
[53] M. Prist *et al.*, "Cyber-physical manufacturing systems: An architecture for sensor integration, production line simulation and cloud services," *Acta IMEKO*, vol. 9, no. 4, 2020, doi: 10.21014/acta_imeko.v9i4.731.
[54] F. Hu, *Cyber-physical systems*. Taylor & Francis Group LLC, 2014.
[55] J. Shi, J. Wan, H. Yan, and H. Suo, "A survey of cyber-physical systems," in *2011 international conference on wireless communications and signal processing (WCSP)*, 2011, pp. 1–6.
[56] B. Scherer, "Hardware-in-the-loop test based non-intrusive diagnostics of cyber-physical systems using microcontroller debug ports," *Acta IMEKO*, vol. 7, no. 1, 2018, doi: 10.21014/acta_imeko.v7i1.513.
[57] P. S. Matharu, A. A. Ghadge, Y. Almubarak, and Y. Tadesse, "Jelly-Z: Twisted and coiled polymer muscle actuated jellyfish robot for environmental monitoring," *Acta IMEKO*, vol. 11, no. 3, 2022, doi: 10.21014/acta_imeko.v11i3.1255.
[58] F. Gabellone, "Digital Twin: a new perspective for cultural heritage management and fruition," *Acta IMEKO*, vol. 11, no. 1, 2022, doi: 10.21014/acta_imeko.v11i1.1085.
[59] J. A. Ejiwale, "Facilitating Teaching and Learning Across STEM Fields," *J STEM Educ*, vol. 13, no. 3, 2012.
[60] J. Bolla, R. Meier, and E. Meyr, "The Safety of Physics Science Activities in a High School Physics Classroom," *Open J Soc Sci*, vol. 04, no. 08, 2016, doi: 10.4236/jss.2016.48017.
[61] K. Ashton, "That Internet of Things Thing," *RFID Journal*, vol. 4986, 2009.
[62] O. Vermesan and P. Friess, *Internet of things: converging technologies for smart environments and integrated ecosystems*. River publishers, 2013.

[63] O. Vermesan and P. Friess, *Internet of things applications-from research and innovation to market deployment*. Taylor & Francis, 2014.
[64] M. B. Ibáñez and C. Delgado-Kloos, "Augmented reality for STEM learning: A systematic review," *Comput Educ*, vol. 123, 2018, doi: 10.1016/j.compedu.2018.05.002.
[65] S. Y. Chen and S. Y. Liu, "Using augmented reality to experiment with elements in a chemistry course," *Comput Human Behav*, vol. 111, 2020, doi: 10.1016/j.chb.2020.106418.
[66] J. C. Byrn *et al.*, "Three-dimensional imaging improves surgical performance for both novice and experienced operators using the da Vinci Robot System," *Am J Surg*, vol. 193, no. 4, 2007, doi: 10.1016/j.amjsurg.2006.06.042.
[67] M. E. Moran, "The da Vinci robot," *J Endourol*, vol. 20, no. 12, pp. 986–990, 2006.
[68] A. J. Bianco, "Why Taking Risks in the Classroom Pays off for Students—and Teachers." 2018.
[69] S. of Education, "The Benefits of Risk-Taking in the Classroom." 2020.
[70] A. Mohammad Bagher, "Introduction to Radioactive Materials," *International Journal of Renewable and Sustainable Energy*, vol. 3, no. 3, 2014, doi: 10.11648/j.ijrse.20140303.13.
[71] G. Nelson, D. Rewy, and D. Reilly, "Gamma-ray interactions with matter," *Passive Nondestructive Analysis of Nuclear Materials*, no. I, 1991.
[72] B. S. Pasternack, "Linear Estimation and the Analysis of Gamma Ray Pulse-Height Spectra," *Technometrics*, vol. 4, no. 4, 1962, doi: 10.1080/00401706.1962.10490040.
[73] M. K. Kumaran and M. Bomberg, *A gamma-spectrometer for determination of density distribution and moisture distribution in building materials*. National Research Council Canada. Division of Building Research, 1985.
[74] K. Fleck, N. Cavanagh, and G. Sarri, "Conceptual Design of a High-flux Multi-GeV Gamma-ray Spectrometer," *Sci Rep*, vol. 10, no. 1, 2020, doi: 10.1038/s41598-020-66832-x.
[75] R. R. Greenberg, P. Bode, and E. A. De Nadai Fernandes, "Neutron activation analysis: A primary method of measurement," *Spectrochimica Acta - Part B Atomic Spectroscopy*, vol. 66, no. 3–4. 2011. doi: 10.1016/j.sab.2010.12.011.
[76] L. H. T. Rietjens, G. J. Arkenbout, G. F. Wolters, and J. C. Kluyver, "Influence of the distance between source and crystal on the detection-efficiency of a gamma-scintillation spectrometer," *Physica*, vol. 21, no. 1–5, pp. 110–116, 1954.
[77] R. A. Rydin, "Resolution, Efficiency and Background Effects in Semiconductor Sandwich Fast Neutron Spectrometers. EUR 2994.," 1966.
[78] STMicroelectronics, Ed., "X-NUCLEO-53L0A1 ranging and gesture detection sensor expansion board based on VL53L0X for STM32 Nucleo." 2016.
[79] STMicroelectronics, Ed., "Getting started with the X-NUCLEO-IKS01A2 motion MEMS and environmental sensor expansion board for STM32 Nucleo." 2017.
[80] STMicroelectronics, Ed., "World's smallest Time-of-Flight ranging and gesture detection sensor." 2018.
[81] STMicroelectronics, Ed., "iNEMO inertial module: always-on 3D accelerometer and 3D gyroscope." 2017.
[82] "STM32 Nucleo-64 boards (MB1136)." 2020.
[83] E. System, Ed., "ESP32-WROOM-32D & ESP32-WROOM-32U." 2021.

[84] Caen, "I-Spector Digital."

[85] "Motion King 17HS Stepper Motor 42mm 1.8 degree." 2020.

[86] STMicroelectronics, Ed., "Stepper motor driver expansion board based on L6474 for STM32 Nucleo." 2015.

[87] J. R. Jiang, H. Subakti, and H. S. Liang, "Fingerprint feature extraction for indoor localization†," *Sensors*, vol. 21, no. 16, 2021, doi: 10.3390/s21165434.

[88] A. Koutris *et al.*, "Deep Learning-Based Indoor Localization Using Multi-View BLE Signal," *Sensors*, vol. 22, no. 7, 2022, doi: 10.3390/s22072759.

[89] J. D. Ceron, F. Kluge, A. Küderle, B. M. Eskofier, and D. M. López, "Simultaneous indoor pedestrian localization and house mapping based on inertial measurement unit and bluetooth low-energy beacon data," *Sensors (Switzerland)*, vol. 20, no. 17, 2020, doi: 10.3390/s20174742.

[90] J. C. Ferreira, R. Resende, and S. Martinho, "Beacons and BIM models for indoor guidance and location," *Sensors (Switzerland)*, vol. 18, no. 12, 2018, doi: 10.3390/s18124374.

[91] J. H. Huh and K. Seo, "An indoor location-based control system using bluetooth beacons for IoT systems," *Sensors (Switzerland)*, vol. 17, no. 12, 2017, doi: 10.3390/s17122917.

[92] K. Kyung-Hyun and L. Choi, "BLE-based localization of smartphone for the passive entry and passive start system," in *Proceedings of the 3rd International Conference on Next Generation Computing (ICNGC 2017b), Kaohsiung, Taiwan*, 2017, pp. 21–24.

[93] H. Liu, J. Yang, S. Sidhom, Y. Wang, Y. Chen, and F. Ye, "Accurate WiFi based localization for smartphones using peer assistance," *IEEE Trans Mob Comput*, vol. 13, no. 10, 2014, doi: 10.1109/TMC.2013.140.

[94] M. Ji, J. Kim, J. Jeon, and Y. Cho, "Analysis of positioning accuracy corresponding to the number of BLE beacons in indoor positioning system," in *International Conference on Advanced Communication Technology, ICACT*, 2015. doi: 10.1109/ICACT.2015.7224764.

[95] P. Bahl and V. N. Padmanabhan, "RADAR: An in-building RF-based user location and tracking system," in *Proceedings - IEEE INFOCOM*, 2000. doi: 10.1109/infcom.2000.832252.

[96] R. Karani *et al.*, "Implementation and design issues for using Bluetooth low energy in passive keyless entry systems," in *2016 IEEE Annual India Conference, INDICON 2016*, 2017. doi: 10.1109/INDICON.2016.7838978.

[97] H. Jun Bae and L. Choi, "Environment Aware Localization with BLE Fingerprinting for the Next Generation PEPS system," in *IEEE Wireless Communications and Networking Conference, WCNC*, 2019. doi: 10.1109/WCNC.2019.8886078.

[98] S. Djosic, I. Stojanovic, M. Jovanovic, T. Nikolic, and G. L. Djordjevic, "Fingerprinting-assisted UWB-based localization technique for complex indoor environments," *Expert Syst Appl*, vol. 167, 2021, doi: 10.1016/j.eswa.2020.114188.

[99] W. Sakpere, M. Adeyeye-Oshin, and N. B. W. Mlitwa, "A state-of-the-art survey of indoor positioning and navigation systems and technologies," *South African Computer Journal*, vol. 29, no. 3, 2017, doi: 10.18489/sacj.v29i3.452.

[100] L. Yi, L. Tao, and S. Jun, "RSSI localization method for mine underground based on RSSI hybrid filtering algorithm," in *2017 9th IEEE International Conference on*

Communication Software and Networks, ICCSN 2017, 2017. doi: 10.1109/ICCSN.2017.8230129.

[101] J. Wisanmongkol, L. Klinkusoom, T. Sanpechuda, L. Kovavisaruch, and K. Kaemarungsi, "Multipath mitigation for RSSI-based Bluetooth low energy localization," in *2019 19th International Symposium on Communications and Information Technologies (ISCIT)*, 2019, pp. 47–51.

[102] S. Sadowski and P. Spachos, "Optimization of BLE beacon density for RSSI-Based indoor localization," in *2019 IEEE International Conference on Communications Workshops, ICC Workshops 2019 - Proceedings*, 2019. doi: 10.1109/ICCW.2019.8756989.

[103] F. J. Böning, A. S. J. Helberg, and M. J. Grobler, "A comparison of wireless node topologies for network coding using practical path-loss models," in *9th International Conference on Networks, ICN 2010*, 2010. doi: 10.1109/ICN.2010.33.

[104] M. Ivanic and I. Mezei, "Distance Estimation Based on RSSI Improvements of Orientation Aware Nodes," in *2018 Zooming Innovation in Consumer Technologies Conference, ZINC 2018*, 2018. doi: 10.1109/ZINC.2018.8448660.

[105] Y. Cao, X. Lu, Z. Zhao, X. Ji, J. Yang, and X. Pang, "A comparative study of BLE-based fingerprint localization for vehicular application," in *Proceedings of 5th IEEE Conference on Ubiquitous Positioning, Indoor Navigation and Location-Based Services, UPINLBS 2018*, 2018. doi: 10.1109/UPINLBS.2018.8559781.

[106] L. Sun, Z. Shang, Y. Xia, S. Bhowmick, and S. Nagarajaiah, "Review of Bridge Structural Health Monitoring Aided by Big Data and Artificial Intelligence: From Condition Assessment to Damage Detection," *Journal of Structural Engineering*, vol. 146, no. 5, 2020, doi: 10.1061/(asce)st.1943-541x.0002535.

[107] J. Seo, J. W. Hu, and J. Lee, "Summary Review of Structural Health Monitoring Applications for Highway Bridges," *Journal of Performance of Constructed Facilities*, vol. 30, no. 4, 2016, doi: 10.1061/(asce)cf.1943-5509.0000824.

[108] F. Lamonaca, C. Scuro, P. F. Sciammarella, R. S. Olivito, D. Grimaldi, and D. L. Carnì, "A layered IoT-based architecture for a distributed structural health monitoring system," *Acta IMEKO*, vol. 8, no. 2, 2019, doi: 10.21014/acta_imeko.v8i2.640.

[109] N. Giulietti *et al.*, "Continuous monitoring of the health status of cement-based structures: electrical impedance measurements and remote monitoring solutions," *Acta IMEKO*, vol. 10, no. 4, 2021, doi: 10.21014/acta_imeko.v10i4.1140.

[110] A. Cigada, L. Corradi Dell'Acqua, B. Mörlin Visconti Castiglione, M. Scaccabarozzi, M. Vanali, and E. Zappa, "Structural Health Monitoring of an Historical Building: The Main Spire of the Duomo Di Milano," *International Journal of Architectural Heritage*, vol. 11, no. 4, 2017, doi: 10.1080/15583058.2016.1263691.

[111] M. Carratu, V. Gallo, V. Paciello, and A. Pietrosanto, "A deep learning approach for the development of an Early Earthquake Warning system," in *Conference Record - IEEE Instrumentation and Measurement Technology Conference*, 2022. doi: 10.1109/I2MTC48687.2022.9806627.

[112] L. Angrisani, F. Bonavolontà, G. D'Alessandro, and M. D'Arco, "Inductive power transmission for wireless sensor networks supply," in *EESMS 2014 - 2014 IEEE Workshop on Environmental, Energy and Structural Monitoring Systems, Proceedings*, 2014. doi: 10.1109/EESMS.2014.6923289.

[113] C. Scuro, P. F. Sciammarella, F. Lamonaca, R. S. Olivito, and D. L. Carni, "IoT for structural health monitoring," *IEEE Instrum Meas Mag*, vol. 21, no. 6, pp. 4–14, 2018.

[114] A. Astarita, F. Tucci, A. T. Silvestri, M. Perrella, L. Boccarusso, and P. Carlone, "Dissimilar friction stir lap welding of AA2198 and AA7075 sheets: forces, microstructure and mechanical properties," *International Journal of Advanced Manufacturing Technology*, vol. 117, no. 3–4, 2021, doi: 10.1007/s00170-021-07816-7.

[115] F. Tucci, P. Carlone, A. T. Silvestri, H. Parmar, and A. Astarita, "Dissimilar friction stir lap welding of AA2198-AA6082: Process analysis and joint characterization," *CIRP J Manuf Sci Technol*, vol. 35, 2021, doi: 10.1016/j.cirpj.2021.09.007.

[116] P. Jiao, K. J. I. Egbe, Y. Xie, A. M. Nazar, and A. H. Alavi, "Piezoelectric sensing techniques in structural health monitoring: A state-of-the-art review," *Sensors (Switzerland)*, vol. 20, no. 13, 2020, doi: 10.3390/s20133730.

[117] I. Roselli *et al.*, "Integrated approach to structural diagnosis by nondestructive techniques: The case of the Temple of Minerva Medica," *Acta IMEKO*, vol. 7, no. 3, 2018, doi: 10.21014/acta_imeko.v7i3.558.

[118] F. Zonzini *et al.*, "Structural Health Monitoring and Prognostic of Industrial Plants and Civil Structures: A Sensor to Cloud Architecture," *IEEE Instrum Meas Mag*, vol. 23, no. 9, 2020, doi: 10.1109/MIM.2020.9289069.

[119] D. Seneviratne, L. Ciani, M. Catelani, and D. Galar, "Smart maintenance and inspection of linear assets: An Industry 4.0 approach," *Acta IMEKO*, vol. 7, no. 1, 2018, doi: 10.21014/acta_imeko.v7i1.519.

[120] C. R. Farrar and K. Worden, "An introduction to structural health monitoring," *Philosophical Transactions of the Royal Society A: Mathematical, Physical and Engineering Sciences*, vol. 365, no. 1851, 2007, doi: 10.1098/rsta.2006.1928.

[121] P. Rizzo and A. Enshaeian, "Challenges in bridge health monitoring: A review," *Sensors*, vol. 21, no. 13. 2021. doi: 10.3390/s21134336.

[122] P. J. Vardanega, G. T. Webb, P. R. A. Fidler, F. Huseynov, K. Kariyawasam, and C. R. Middleton, "Bridge monitoring," in *Innovative bridge design handbook*, Elsevier, 2022, pp. 893–932.

[123] L. Ciani, A. Bartolini, G. Guidi, and G. Patrizi, "A hybrid tree sensor network for a condition monitoring system to optimise maintenance policy," *Acta IMEKO*, vol. 9, no. 1, 2020, doi: 10.21014/acta_imeko.v9i1.732.

[124] M. Brambilla *et al.*, "Metrological Evaluation of New Industrial SHM Systems Based on MEMS and Microcontrollers," in *Lecture Notes in Civil Engineering*, 2023. doi: 10.1007/978-3-031-07254-3_78.

[125] A. Liccardo, F. Bonavolontà, M. Balato, and C. Petrarca, "Lora-Based Smart Sensor for PD Detection in Underground Electrical Substations," *IEEE Trans Instrum Meas*, vol. 71, 2022, doi: 10.1109/TIM.2022.3200427.

[126] E. Reynders, "System Identification Methods for (Operational) Modal Analysis: Review and Comparison," *Archives of Computational Methods in Engineering*, vol. 19, no. 1, 2012, doi: 10.1007/s11831-012-9069-x.

[127] A. Lavatelli and E. Zappa, "Uncertainty in vision based modal analysis: Probabilistic studies and experimental validation," *Acta IMEKO*, vol. 5, no. 4, 2016, doi: 10.21014/acta_imeko.v5i4.426.

[128] G. Cerro *et al.*, "An accurate localization system for Nondestructive testing based on magnetic measurements in quasi-planar domain," *Measurement (Lond)*, vol. 139, 2019, doi: 10.1016/j.measurement.2019.03.022.

[129] R. R. Ribeiro and R. de M. Lameiras, "Evaluation of low-cost MEMS accelerometers for SHM: Frequency and damping identification of civil structures," *Latin American Journal of Solids and Structures*, vol. 16, no. 7 CILAMCE 2018, 2019, doi: 10.1590/1679-78255308.

[130] F. Bonavolonta, L. P. Di Noia, A. Liccardo, S. Tessitore, and D. Lauria, "A PSO-MMA Method for the Parameters Estimation of Interarea Oscillations in Electrical Grids," *IEEE Trans Instrum Meas*, vol. 69, no. 11, 2020, doi: 10.1109/TIM.2020.2998909.

[131] R. Iervolino, F. Bonavolontà, and A. Cavallari, "A wearable device for sport performance analysis and monitoring," in *2017 IEEE International Workshop on Measurement and Networking, M and N 2017 - Proceedings*, 2017. doi: 10.1109/IWMN.2017.8078375.

[132] M. Varanis, A. Silva, A. Mereles, and R. Pederiva, "MEMS accelerometers for mechanical vibrations analysis: a comprehensive review with applications," *Journal of the Brazilian Society of Mechanical Sciences and Engineering*, vol. 40, no. 11, 2018, doi: 10.1007/s40430-018-1445-5.

[133] C. Bedon, E. Bergamo, M. Izzi, and S. Noè, "Prototyping and validation of MEMS accelerometers for structural health monitoring—the case study of the Pietratagliata cable-stayed bridge," *Journal of Sensor and Actuator Networks*, vol. 7, no. 3, 2018, doi: 10.3390/jsan7030030.

[134] S. Han, Z. Meng, O. Omisore, T. Akinyemi, and Y. Yan, "Random error reduction algorithms for MEMS inertial sensor accuracy improvement—a review," *Micromachines*, vol. 11, no. 11. 2020. doi: 10.3390/mi11111021.

[135] H. Huang, H. Zhang, and L. Jiang, "An Optimal Fusion Method of Multiple Inertial Measurement Units Based on Measurement Noise Variance Estimation," *IEEE Sens J*, vol. 23, no. 3, 2023, doi: 10.1109/JSEN.2022.3229475.

[136] S. Ahvenjärvi, "The Human Element and Autonomous Ships," *TransNav, the International Journal on Marine Navigation and Safety of Sea Transportation*, vol. 10, no. 3, 2017, doi: 10.12716/1001.10.03.18.

[137] P. D. Groves, "Principles of GNSS, inertial, and multisensor integrated navigation systems, 2nd edition [Book review]," *IEEE Aerospace and Electronic Systems Magazine*, vol. 30, no. 2, 2015, doi: 10.1109/maes.2014.14110.

[138] G. T. Schmidt, "INS / GPS Technology Trends," *Technology (Singap World Sci)*, vol. 116, no. 2010, 2011.

[139] G. De Alteriis, V. Bottino, C. Conte, G. Rufino, and R. S. Lo Moriello, "Accurate attitude inizialization procedure based on MEMS IMU and magnetometer integration," in *2021 IEEE International Workshop on Metrology for AeroSpace, MetroAeroSpace 2021 - Proceedings*, 2021. doi: 10.1109/MetroAeroSpace51421.2021.9511679.

[140] A. Liccardo *et al.*, "Detection and Analysis of Inter-Area Oscillations Through a Dynamic-Order DMD Approach," *IEEE Trans Instrum Meas*, vol. 71, 2022, doi: 10.1109/TIM.2022.3186371.

[141] R. I. Alfian, A. Ma'Arif, and S. Sunardi, "Noise reduction in the accelerometer and gyroscope sensor with the Kalman filter algorithm," *Journal of Robotics and Control (JRC)*, vol. 2, no. 3, 2021, doi: 10.18196/jrc.2375.

[142] D. Capriglione *et al.*, “Experimental Analysis of Filtering Algorithms for IMU-Based Applications under Vibrations,” *IEEE Trans Instrum Meas*, vol. 70, 2021, doi: 10.1109/TIM.2020.3044339.

[143] F. Bonavolonta, M. D’Arco, A. Liccardo, and O. Tamburis, “Remote laboratory design and implementation as a measurement and automation experiential learning opportunity,” *IEEE Instrum Meas Mag*, vol. 22, no. 6, 2019, doi: 10.1109/MIM.2019.8917906.

[144] D. Capriglione, G. Cerro, L. Ferrigno, and G. Miele, “Analysis and implementation of a wavelet based spectrum sensing method for low SNR scenarios,” in *WoWMoM 2016 - 17th International Symposium on a World of Wireless, Mobile and Multimedia Networks*, 2016. doi: 10.1109/WoWMoM.2016.7523585.

[145] G. De Alteriis *et al.*, “Innovative Fusion Strategy for MEMS Redundant-IMU Exploiting Custom 3D Components,” in *2022 IEEE 9th International Workshop on Metrology for AeroSpace, MetroAeroSpace 2022 - Proceedings*, 2022. doi: 10.1109/MetroAeroSpace54187.2022.9856222.

[146] A. T. Silvestri, I. Papa, F. Rubino, and A. Squillace, “On the critical technological issues of CFF: enhancing the bearing strength,” *Materials and Manufacturing Processes*, vol. 37, no. 2, 2022, doi: 10.1080/10426914.2021.1954195.

[147] A. T. Silvestri, I. Papa, and A. Squillace, “Influence of Fibre Fill Pattern and Stacking Sequence on Open-Hole Tensile Behaviour in Additive Manufactured Fibre-Reinforced Composites,” *Materials*, vol. 16, no. 6, 2023, doi: 10.3390/ma16062411.

[148] R. S. Peres, A. Dionisio Rocha, P. Leitao, and J. Barata, “IDARTS – Towards intelligent data analysis and real-time supervision for industry 4.0,” *Comput Ind*, vol. 101, 2018, doi: 10.1016/j.compind.2018.07.004.

[149] E. Sezer, D. Romero, F. Guedea, M. MacChi, and C. Emmanouilidis, “An Industry 4.0-Enabled Low Cost Predictive Maintenance Approach for SMEs,” in *2018 IEEE International Conference on Engineering, Technology and Innovation, ICE/ITMC 2018 - Proceedings*, 2018. doi: 10.1109/ICE.2018.8436307.

[150] J. S. Rahhal and Di. Abualnadi, “IOT Based Predictive Maintenance Using LSTM RNN Estimator,” in *2nd International Conference on Electrical, Communication and Computer Engineering, ICECCE 2020*, 2020. doi: 10.1109/ICECCE49384.2020.9179459.

[151] A. Cachada *et al.*, “Maintenance 4.0: Intelligent and Predictive Maintenance System Architecture,” in *IEEE International Conference on Emerging Technologies and Factory Automation, ETFA*, 2018. doi: 10.1109/ETFA.2018.8502489.

[152] A. K. Mahamad, S. Saon, and T. Hiyama, “Predicting remaining useful life of rotating machinery based artificial neural network,” in *Computers and Mathematics with Applications*, 2010. doi: 10.1016/j.camwa.2010.03.065.

[153] S. Basak, S. Sengupta, and A. Dubey, “Mechanisms for integrated feature normalization and remaining useful life estimation using LSTMs applied to hard-disks,” in *Proceedings - 2019 IEEE International Conference on Smart Computing, SMARTCOMP 2019*, 2019. doi: 10.1109/SMARTCOMP.2019.00055.

[154] A. De Santo, A. Galli, M. Gravina, V. Moscato, and G. Sperli, “Deep Learning for HDD Health Assessment: An Application Based on LSTM,” *IEEE Transactions on Computers*, vol. 71, no. 1, 2022, doi: 10.1109/TC.2020.3042053.

[155] A. N. Nichenametla, S. Nandipati, and A. L. Waghmare, “Optimizing life cycle cost of wind turbine blades using predictive analytics in effective maintenance planning,” in *Proceedings - Annual Reliability and Maintainability Symposium*, 2017. doi: 10.1109/RAM.2017.7889682.

[156] O. Aydin and S. Guldamlasioglu, “Using LSTM networks to predict engine condition on large scale data processing framework,” in *2017 4th International Conference on Electrical and Electronics Engineering, ICEEE 2017*, 2017. doi: 10.1109/ICEEE2.2017.7935834.

[157] Z. Chen, M. Wu, R. Zhao, F. Guretno, R. Yan, and X. Li, “Machine Remaining Useful Life Prediction via an Attention-Based Deep Learning Approach,” *IEEE Transactions on Industrial Electronics*, vol. 68, no. 3, 2021, doi: 10.1109/TIE.2020.2972443.

[158] N. Williams, S. Zander, and G. Armitage, “A preliminary performance comparison of five machine learning algorithms for practical IP traffic flow classification,” *Computer Communication Review*, vol. 36, no. 5, 2006, doi: 10.1145/1163593.1163596.

[159] L. Bai, R. Liu, F. Wang, Q. Sun, and F. Wang, “Estimating railway rail service life: A rail-grid-based approach,” *Transp Res Part A Policy Pract*, vol. 105, 2017, doi: 10.1016/j.tra.2017.08.007.

[160] S. Hochreiter and J. Schmidhuber, “Long short-term memory,” *Neural Comput*, vol. 9, no. 8, pp. 1735–1780, 1997.

[161] F. A. Gers, J. Schmidhuber, and F. Cummins, “Learning to forget: Continual prediction with LSTM,” *Neural Comput*, vol. 12, no. 10, 2000, doi: 10.1162/089976600300015015.

[162] G. Kendall Maurice, “Rank correlation methods,” *Charles Griffin, London*, 1975.

[163] D. Quade, “Rank Analysis of Covariance,” *J Am Stat Assoc*, vol. 62, no. 320, 1967, doi: 10.1080/01621459.1967.10500925.